

Dissertation
submitted to the
Combined Faculty of Natural Sciences and Mathematics
of Heidelberg University, Germany
for the degree of
Doctor of Natural Sciences

Put forward by
Riccardo, Dal Bello
born in: Spilimbergo, Italy
Oral examination: December 17th, 2019

Nuclear prompt gamma spectroscopy for range verification in ion-beam therapy

Referees:

Prof. Dr. Joao Seco
Prof. Dr. Oliver Jäkel

Declaration

I, Riccardo, Dal Bello, declare here that this Ph.D. thesis is the result of my own research, and that all sources used in this work have been duly referenced. This thesis has not been submitted to any other university or institute for a degree award.

Heidelberg, Germany

October 2nd, 2019

Signed:

Abstract

Proton and heavier ions have a characteristic energy deposition profile presenting the maximum at the end of range of the primary particles. This feature potentially allows delivering highly conformal radiation therapy, depositing most of the dose in the target volume and sparing the healthy tissue surrounding it. Despite its expanding clinical application, several limitations still affect this technique and there are great opportunities for further improvement. This thesis addresses the issue of range uncertainties. Many factors influence the range of the primary particles. Due to the sharp spatial gradients of the dose distribution, even a small shift can lead to severe changes in the treatment quality. Countermeasures are usually adopted in clinical practice to make the dose delivery robust to such shifts at the price of obtaining sub-optimal treatment plans. This thesis aims to develop a pre-clinical prototype to measure on-line and in-vivo the position of the dose deposition. The technique is based on nuclear prompt gamma spectroscopy. In this work, we first proposed the use of a novel detector type. Then, we optimized through simulations and experimentally characterized the detector system. Finally, we experimentally demonstrated the measurement of the particles range with millimetric precision in clinically relevant conditions.

Zusammenfassung

Protonen und schwerere Ionen haben ein charakteristisches Energiedepositionsprofil, welches eine maximale Energieabgabe am Ende der Reichweite der Primärpartikel aufweist. Durch diese Eigenschaft kann eine hochgradig konformale Strahlentherapie durchgeführt werden, wobei der Hauptteil der Dosis im Tumervolumen wirkt und das umgebende, gesunde Gewebe geschoont wird. Trotz der expandierenden klinischen Anwendung unterliegt diese Technik einiger Einschränkungen und es gibt einige Möglichkeiten zur weiteren Verbesserung. Diese Arbeit behandelt das Problem der Reichweitenunschärfe. Viele Faktoren beeinflussen die Reichweite der Primärpartikel. Aufgrund der scharfen räumlichen Gradienten der Dosisdistribution kann schon ein kleiner Shift zu starken Änderungen in der Qualität der Behandlung führen. Gegenmaßnahmen werden meistens im Klinikalltag angewandt, um die Dosisabgabe robust gegenüber solchen Shifts zu gestalten, was jedoch zu suboptimalen Bestrahlungsplänen führt. Das Ziel dieser Arbeit war, einen präklinischen Prototypen zu entwickeln, um die Position der Dosisabgabe online und in-vivo zu messen. Die Technik basiert auf Kernprompt-gamma-Spektroskopie. In dieser Arbeit wurde zunächst die Verwendung eines neuen Detektortyps motiviert. Anschließend wurde das Detektorsystem durch Simulationen optimiert und experimentell charakterisiert. Letztendlich konnten wir experimentell die Partikelreichweite mit Präzision im Millimeterbereich in klinisch relevanten Bedingungen bestimmen.

Contents

Abstract	v
1 Introduction	1
1.1 Motivation	1
1.2 Aim of this thesis	3
2 Background	5
2.1 Physics of ion beam therapy	5
2.1.1 Energy loss of ion beams in matter	5
2.1.2 Nuclear reactions	7
2.1.3 Ion beams production	11
2.1.4 Physical range uncertainties	12
2.2 Range verification in ion beam therapy	13
2.2.1 Ion imaging	13
2.2.2 Positron emission tomography	14
2.2.3 Prompt gamma	15
2.2.4 Other techniques	17
2.3 State-of-the-art prompt gamma technology	18
3 Overview of the results	21
4 Publications	23
4.1 Proposal of a novel scintillator for prompt gamma spectroscopy	24
4.2 Monte Carlo optimization of the spectroscopic unit	34
4.3 Experimental verification of the spectroscopic unit performances	51
4.4 Development and characterization of the beam trigger	71
4.5 Absolute range verification for ion beams	88
5 Discussion	121
5.1 New findings in prompt gamma spectroscopy	121
5.2 Features specific to synchrotrons and ion beams	126
5.3 Towards clinical applicability	128
5.4 Limitations and conceivable solutions	129
6 Summary	131
List of publications	133
Bibliography	139

Chapter 1

Introduction

An in-vivo and on-line imaging and range measurement would be the holy grail of radio-therapy

L. Bottura - CERN

1.1 Motivation

Most of the oncology patients receive radiation therapy either as a primary form of treatment or within a combined strategy. The technology employed in this field drastically evolved during the last decades. The conformal radiation therapy has been replaced by the intensity modulated radiation therapy, which is nowadays a standard of clinical care. The image guidance and online imaging have also been developed to provide a more focused dose delivery with high energy photon beams. This type of ionizing radiation is the most commonly adopted in the clinical practice. A small but increasing fraction of patients is treated with beams of protons or heavier ions. Several properties support the use of charged particle therapy. As a matter of fact, the patients who received charged particle therapy overcame the 200'000 units at the end of 2018. The physical rationale is based on the characteristic dose profile, which presents the maximum of the energy deposition at a depth defined by the initial beam energy. Its comparison with the depth dose profile of high energy photon beams clearly shows the potential advantage in treating deeply located tumors (Figure 1.1). The biological effect is enhanced compared to photon beams due to the higher local ionization density, which can be beneficial especially for radio resistant tumors in presence of beams heavier than protons. The technological challenges in producing and delivering high energy ion beams have been overcome and several commercial solutions are nowadays available to integrate charged particle therapy in clinical environments. The advantage for the patients is being investigated by several randomised clinical trials. Nonetheless, several challenges are still present and charged particle therapy has great potential for further improvement. This thesis addresses the issue of range uncertainty investigating a technique to measure the absolute position of the dose deposition during the treatments.

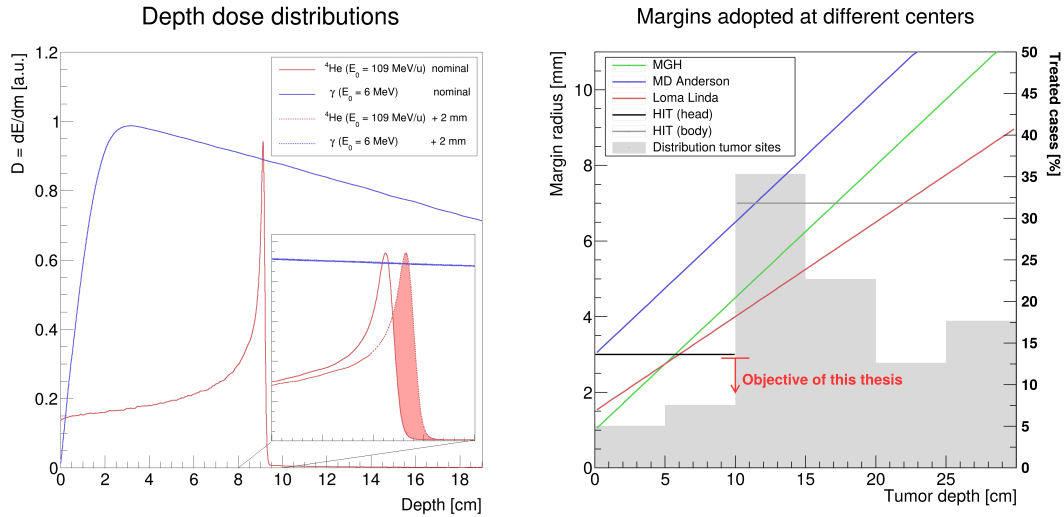


FIGURE 1.1: *Left*: Depth dose comparison for a photon and a ${}^4\text{He}$ beam in water at clinically relevant initial energies. The insert shows the detail of a scenario in which a longitudinal displacement of 2 mm is added for both beams. The additional dose delivered by the displaced ${}^4\text{He}$ beam is shown in red. Data generated with FLUKA. *Right*: Comparison of the margins used at different proton and ion therapy centers. Data reproduced from Greilich, 2017. The distribution of the tumor depth for patients referred to CPT is also shown with an histogram. The red arrow compares the aim of this thesis to the data.

The localised energy deposition of ion beams is advantageous for delivering more conformal therapy but has remarkable drawbacks in presence of errors. This effect can be attributed to the high spatial gradients of the dose distribution, especially in the beam direction, which are not present for high energy photons. The erroneous modelling of the interaction of the ion beams with the patient tissue along the beam path can lead to small deviations between the predicted and the actual position of the dose deposition. An example where a deviation of $\Delta z = 2$ mm was artificially introduced is shown in Figure 1.1. The dose deposition for the photon beam is substantially unaltered. On the other hand, for the ion beam, this shift removes the dose from the planned location and moves it to a more distal position. This simple physical effect could be translated to a clinical scenario of a prostate treatment where part of the dose planned for the target volume is instead delivered to the nearby organ at risk, the rectum, leading to severe side effects. To avoid such situation, frontal beams are generally avoided and the treatments are performed with a sub-optimal solution consisting of two lateral beams. This provides an example of how range uncertainties limit the exploitation of the full potential of charged particle therapy. Moreover, the concept of safety margins is adopted to ensure that the whole tumor volume receives the planned dose. This approach consists in expanding the volume to which the maximum dose is delivered to account for possible uncertainties. An example of typical sizes of the margins is showed in Figure 1.1.

Their dimension is in general depth dependent, as increasing the penetration depth the uncertainties accumulate. For deep located tumors, the additional volume irradiated could be as large as the tumor volume itself. The sources of the uncertainties are diverse and will be later presented. The direct measurement of the dose deposition location during the beam delivery can on one hand lead to a reduction of the margin sizes and on the other hand to an increase in the confidence when choosing beam angles facing an organ at risk. These two outcomes can greatly improve the quality of charged particle therapy treatments.

1.2 Aim of this thesis

This thesis aims to develop a technique to measure in-vivo and on-line the location of the dose deposition during ion beam treatments. The proposed method is prompt gamma spectroscopy. This technique measures the secondary radiation produced by specific de-excitation channels following nuclear inelastic reactions between the beam particles and the target nuclei. In particular, the high energy gamma radiation emitted within nanoseconds from the beam delivery is detected. The measurement of multiple spectral lines, each with a characteristic energy-dependent cross-section for its production, has the potential advantage of measuring the absolute position of the beam particles range. Additional advantages compared to other range monitor techniques span from the negligible contribution of the biological washout due to the nearly-instantaneous emission of the secondary radiation, to the high spatial resolution achievable selecting only the events that do not undergo any interaction before reaching the detector system. Prompt gamma spectroscopy has been demonstrated for protons accelerated by cyclotrons. Here, we investigate the technique for heavier ions accelerated by a synchrotron. Several challenges have to be addressed. The different time structure of a synchrotron with respect to cyclotrons requires the introduction of a beam trigger. The larger mass of the projectiles leads to an increase in the Doppler broadening and the production of prompt gamma signal from secondary fragments not directly correlated to the dose deposition position. These and other phenomena have to be investigated and it has to be demonstrated whether prompt gamma spectroscopy is applicable to ions accelerated by a synchrotrons in clinically relevant scenarios. The objective of this thesis is schematically presented in Figure 1.1. We aim to measure the range of the primary ions with a confidence interval that is smaller compared to the margins size nowadays adopted in clinical practice. To do so, we develop a pre-clinical prototype for prompt gamma spectroscopy at a synchrotron based facility.

The thesis includes a comprehensive background chapter describing the relevant physical processes and their usage by different range verification techniques (Chapter 2). This is followed by a concise overview of the results (Chapter 3) and the manuscripts presenting the original research (Chapter 4). Finally, a comprehensive discussion of the findings is developed (Chapter 5) and the thesis is concluded with a summary (Chapter 6).

Chapter 2

Background

2.1 Physics of ion beam therapy

2.1.1 Energy loss of ion beams in matter

Charged particle therapy makes use of protons and heavier ions accelerated to kinetic energies up to $E_{\text{kin}} = 430 \text{ MeV/u}$ (Haberer et al., 2004). At such energy, ^{12}C ions have a velocity of approximately $\beta = 0.74$; while to obtain the same penetration potential (approximately $d = 30 \text{ cm}$ in water) is sufficient to accelerate ^1p beams to $E_{\text{kin}} = 220 \text{ MeV}$ corresponding to $\beta = 0.59$. Therefore, a key aspect of CPT is the description of the physics regulating the interactions of slightly relativistic protons and heavier ions from the energies previously reported down to rest. At the HIT facility ¹ beams of ^1p , ^4He , ^{12}C and ^{16}O are available. In the following, these are referred to as light ions or, simply, ions (Wambersie et al., 2004).

While traveling in matter, ions can undergo the following interactions: Coulomb interactions with electrons, Coulomb interactions with nuclei, nuclear reactions and Bremsstrahlung. In a first-order approximation, ions travel on a straight line and continuously lose their energy until rest. The major mechanism for such energy loss is the interaction with the electrons in the target. As shown in Figure 2.1, nuclear interactions have only a minor contribution to the energy loss but they are relevant for several range verification methods, as discussed later. Bremsstrahlung can be neglected due to the high mass of the projectiles. The energy loss due to a single electronic collision and the time between two collisions are stochastic processes. However, for a description of the phenomena at the fraction of millimeter or larger scales one is rather interested in the mean energy loss per unit path length. i.e. the stopping power. This is well described by the Bethe-Bloch formula (Bethe, 1930; Bloch, 1933) with the relativistic correction modelled by Fano, 1963:

$$S = - \left\langle \frac{dE}{dz} \right\rangle = 4\pi N_A r_e^2 m_e c^2 \rho \frac{Z \cdot z^2}{A \cdot \beta^2} \cdot \left(\ln \frac{2m_e c^2 \gamma^2 \beta^2}{\langle I \rangle} - \beta^2 - \frac{\delta}{2} - \frac{C}{Z} \right) \quad (2.1)$$

where the constants are: N_A Avogadro's number, $r_e = \frac{1}{4\pi\epsilon_0} \frac{e^2}{m_e c^2}$ classical electron radius, m_e electron mass and c speed of light. The projectile properties

¹Heidelberg Ion-Beam Therapy Center, Im Neuenheimer Feld 450, 69120 Heidelberg, Germany

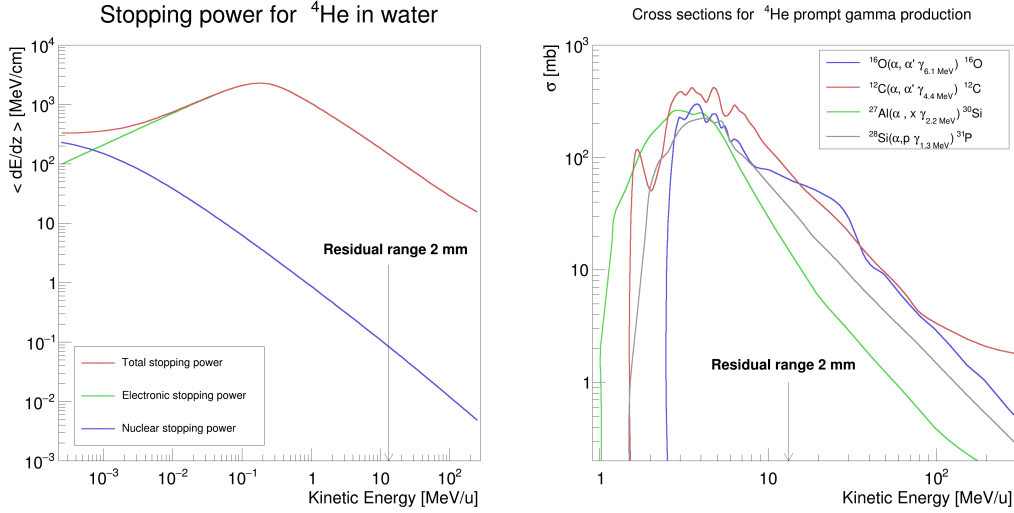


FIGURE 2.1: *Left:* Stopping power for ^4He beams in water over a wide energy spectrum. The total (red) stopping power is the sum of the electronic (green) and nuclear (blue) contribution. As a reference, the kinetic energy corresponding to a residual range of 2 mm is indicated. Data reproduced from the ASTAR database [ASTAR](#). *Right:* Evolution of the angular integrated cross sections for the production of prompt gamma radiation in the collision of ^4He with different light (abundant in human tissue) and heavier (found in prosthesis or implants) nuclei. As a reference, the kinetic energy corresponding to a residual range of 2 mm is indicated. Data reproduced from Kozlovsky et al., [2002](#).

are its charge z , its velocity β and the corresponding Lorentz factor γ . The target is described by the atomic number Z , the atomic mass A , the mass density ρ and the mean ionization energy $\langle I \rangle$. Finally, δ is the density correction and C is the shell correction term. Assuming that the kinetic energy lost by the primary beam is deposited locally, the equation 2.1 shows directly the fundamental dosimetric property of ion beams. In first approximation the energy loss is dominated by the term β^{-2} , which leads to a minimum energy loss when the ions are travelling at high velocities in the first part of the target and maximum energy loss at deeper positions, right before stopping. Such dependency produces the so-called Bragg peak with maximum dose deposition at the end of the range (Figure 1.1). More precisely, the range can be experimentally measured at the location where the dose deposition drops to 80% of its maximum, which corresponds to the position where 50% of the ions stop. (Schuemann et al., [2014](#)). On the other hand, it can be theoretically calculated from equation 2.1 with the continuous slowing down approach:

$$R = \int_{E_0}^0 \left\langle \frac{dE}{dz} \right\rangle^{-1} \cdot dE. \quad (2.2)$$

The analytic solution of the equation 2.2 is not available; however, several

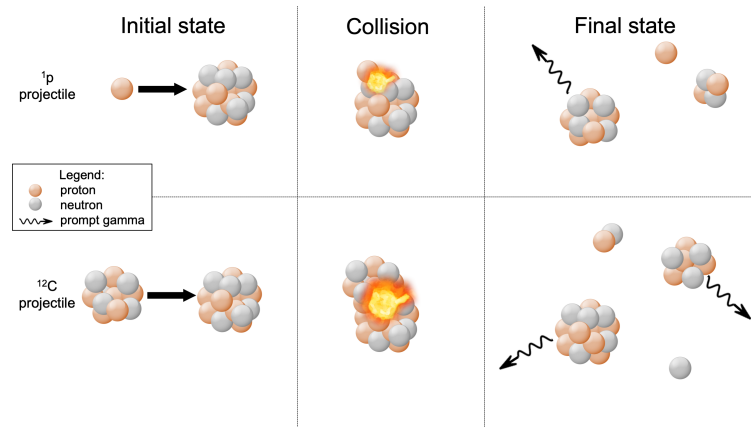


FIGURE 2.2: Schematic representation of nuclear interactions of the beam particles with the target nuclei. Top: proton-nucleus inelastic collision, specifically $^{16}\text{O}(p, p' n)^{12}\text{C}^*$. Bottom: nucleus-nucleus inelastic collision, specifically $^{16}\text{O}(^{12}\text{C}, ^{10}\text{B}^* d n)^{15}\text{O}^*$. Reproduced from Magalhaes Martins et al., 2019a.

approximations have been proposed (Bortfeld, 1997). Among the approximations, it is remarkable the precision achievable with the simple model proposed in early times by Bragg et al., 1905. In this case, the energy loss is described by a power law $\langle dE/dz \rangle \propto E^{1-\alpha}$ and therefore the equation 2.2 can be promptly integrated obtaining $R = a \cdot E_0^\alpha$. Such relation is known as Geiger rule ($\alpha = 1.5$) for energies up to 10 MeV and as Bragg–Kleemann rule ($\alpha \simeq 1.8$) for higher energies.

2.1.2 Nuclear reactions

Note: Parts of this sub-section were also published in the B.I book chapter.

The direct interaction of the ions with the target nuclei has only a minor contribution to the total stopping power. Still, the nuclear interactions are highly relevant in charged particle therapy. First, the correct modeling of such events is required to complete the dosimetric description of ions beams, which so far was limited to the electronic interactions. Then, the production of secondary radiation that leaves the patient can be exploited to develop methods to measure the range of the projectiles in-vivo and on-line. Such methods are referred to as range verification techniques.

For what concerns the complete the dosimetric description of ion beams, a fundamental difference has to be highlighted between protons and heavier ions. The former are made of just one nucleon and when they undergo a nuclear inelastic interaction the projectile is removed from the primary beam fluence. There is no dose deposition beyond the range of the primary protons. On the other hand, heavier ions include multiple nucleons. Among the nuclear interaction channels, there is the possibility for the primary ion to undergo fragmentation and produce lighter charged fragments. Such light fragments are highly energetic, as they are generated in the moving frame of

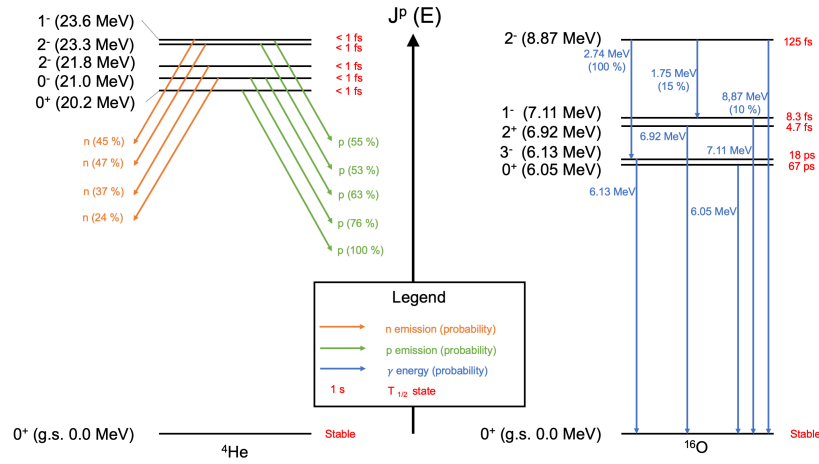


FIGURE 2.3: Nuclear energy levels for ${}^4\text{He}$ (left) and ${}^{16}\text{O}$ (right). The ground state and the first five states above it are shown. The principal de-excitation channels and their characteristic decay times are also reported. Reproduced from Magalhaes Martins et al., 2019a.

the projectile and on the top of this they can carry an additional momentum up to the Fermi momentum:

$$Z = \frac{V(p_F^p)^3}{3\pi^2\hbar^3} = \frac{\frac{4}{3}\pi R(p_F^p)^3}{3\pi^2\hbar^3} \rightarrow p_F = \frac{\hbar}{R} \left(\frac{9\pi Z}{4} \right)^{1/3} = 248 \text{ MeV}/c \quad (2.3)$$

which is here (equation 2.3, Povh et al., 2008) calculated for the protons in a ${}^{12}\text{C}$ nucleon, approximating $R = 1.21 \cdot A^{1/3} = 2.77 \text{ fm}$. Such protons have a velocity of $\beta'_p = pc/\gamma m_p c^2 = 0.26$ in the projectile moving frame, which can be converted in up to $\beta_p = (\beta'_p + \beta_{12\text{C}})/(1 + \beta'_p \cdot \beta_{12\text{C}}) = 0.84$ in the patient frame. This upper limit shows that the light fragments can travel greater distances than the primary heavier projectiles and leads to energy deposition beyond the prescribed range, which is normally referred to as dose deposition tail. The heavier the primary projectile, the greater the number of light fragment production. It is therefore fundamental a proper modelling of the energy dependent charge- and mass-changing cross sections to correctly describe the depth dose curve. Recent studies aimed to precisely characterize these for ${}^4\text{He}$ beams (Horst et al., 2019), while the next generation experiments are expected to further increase the precision of the experimental data available for ${}^{12}\text{C}$ beams (Alexandrov et al., 2019).

Most of the range verification methods are based on nuclear inelastic collisions. These are violent events where the projectile may change the target nucleus to a different isotope by knocking out light fragments or modifying its energy state. Because the produced nuclei are not at the ground level, they undergo a chain of de-excitation reactions. Secondary radiation is produced during these processes, it can leave the patient and be measured with an external detector to retrieve the Bragg peak position.

Few general aspects of range verification based on inelastic nuclear interactions have to be highlighted. First, the secondary radiation is produced by interaction mechanisms that differ radically from the ones leading to the primary energy loss and the production of the Bragg peak. Therefore, the correlation of the deposited dose with the by-products of nuclear interactions exists but it is not direct. The existence of the correlation is proven by Figure 2.1. Here, it is shown how in a neighborhood of the projectile energy corresponding to the last millimeters of its range, the prompt gamma yield is monotonic with respect to the residual kinetic energy, therefore invertible. Second, the energies of the particles outgoing nuclear interactions can reach several MeV. This implies that the secondary radiation (e.g. neutrons, protons or gamma-rays) has a high potential to leave the patient and be measured. Third, the time scale of nuclear interactions is the one of the strong force. The de-excitation processes that follow have characteristic times connected to each specific channel. These can range from several minutes (e.g. $T_{1/2} = 20.4$ min for the β^+ decay of $^{11}\text{C}_{\text{g.s.}}$) down to sub-nanoseconds (e.g. $T_{1/2} = 18.4$ ps for the γ decay of $^{16}\text{O}^*_{6.13\text{ MeV}}$). In this thesis, we will focus on the fast processes that produce high energetic gamma radiation, i.e. the prompt gamma.

Prompt gamma are one of the possible by-products of the inelastic nuclear reactions of the beam particles with the target nuclei. Figure 2.2 represents in a schematic way two possible inelastic collisions producing final states differing from the initial ones. Generally, after such a collision the beam particle is lost and does not contribute to the primary dose deposition in the Bragg peak, as discussed before. Typically, for a 16 cm deep Bragg peak, about 20% of the primary protons and about 50% of the primary ^{12}C ions undergo inelastic nuclear interactions before the end of the range (Kraan, 2015). The cross sections of such processes are energy dependent and they generally increase at lower collision energies before dropping rapidly when the projectile has not anymore enough energy to overcome the Coulomb barrier. The effect of the Coulomb repulsion may be factorized from the total cross section

$$\sigma(E) = \frac{1}{E} \cdot \exp\left(-2\pi\frac{z \cdot Z}{\hbar v}e^2\right) \cdot S(E) \quad (2.4)$$

obtaining a direct relation with the astrophysical S-factor $S(E)$, which varies less strongly with increasing energy (Thompson et al., 2009). The investigation of such processes is indeed of great relevance for astrophysics, e.g. in the analysis of solar flare data. Therefore, several compilations of the reaction channels leading to gamma de-excitation are available (Kozlovsky et al., 2002). Interestingly, high resolution spectroscopic measurements were performed for the light nuclei found in the Earth atmosphere, which are also the most abundant species making up the human body. This created a solid database for the investigation of prompt gamma in ion beam therapy. However, astrophysical studies focus mainly on high energy gamma lines, provide the total cross sections integrated over the solid angle and limited information on the time structure is discussed. Therefore, a refinement of the

experimental data to perform range verification through prompt gamma is required.

Inelastic nuclear interactions produce excited nuclear states. Figure 2.3 shows the first five energy levels above the ground state for two light nuclei relevant for charged particle therapy. Similar properties are observed also for other nuclei such as ^1p or ^{12}C . The principal de-excitation mechanisms are depicted as well. The first property to be noticed is that the energy separation for the nuclear levels is in the MeV range, which correlates directly with the energy of the secondary radiation produced in the de-excitation processes. A major difference is observed between the lightest nuclei and the heavier ones. Namely, the excited levels of ^1p or ^4He nuclei do not relax by the emission of gamma radiation. The energy separation between the ground state and the first excited level is sufficient to open the channels for the emission of nucleons. A different situation is observed for ^{12}C or ^{16}O nuclei. Here, the energy separation between the ground state and the excited levels is smaller and the preferred de-excitation channel is the gamma isomeric transition. We observe that every nuclear level has a preferred de-excitation channel. The ground state is reached either with a single transition or with a photon emission chain. The net result is that a series of gamma quanta are emitted, having well defined discrete energies. It is important to notice that every single nucleus has its unique energy levels. Therefore, the discrete energy spectrum of the de-excitation photons is a characteristic feature unique for every given isotope.

It is now possible to interpret the prompt gamma emission in the case of heavier projectiles, such as ^{12}C or ^{16}O . Here, both the target nucleus and the projectile can be excited and produce gamma radiation. As presented schematically in Figure 2.2, the gamma emission for the excited projectile happens while this nucleus is travelling away from the interaction zone in a relativistic moving frame. Therefore, the energy of the gamma quanta emitted by the projectile has to be corrected by the relativistic Doppler factor. This does not apply for the prompt gamma emission from the target nucleus. Figure 2.3 also presents the characteristic times ($T_{1/2}$) that describe the time intervals in which the excited nuclear states exist after their production and before undergoing relaxation. These values are specific for every level and we can generally observe that $T_{1/2} \ll 1$ ns.

Finally, we should also point out that there is a second mechanism for nuclear de-excitation replacing the single discrete emission with multiple photon emission. This presents a continuum spectrum. However, for the energies and the nuclei found in proton and ion therapy, the probability for the discrete emission is approximately an order of magnitude higher than the continuous one (Dedes et al., 2014).

To summarize, the nuclear interactions of the beam particle with the target nuclei play a minor role in dose deposition but are important for range verification. In particular, the inelastic nuclear collisions that produce excited nuclear states. These can de-excite with the emission of gamma radiation that leaves the patient and can be measured with an external detector. The gamma radiation is emitted by light nuclei, such as ^{12}C or ^{16}O ,

	Cyclotron ^1p	Synchrotron ^1p	Synchrotron ^{12}C	Synchrocyclotron ^{12}C
Macro-period (T_1)	-	10 s	10 s	1 ms
Micro-period (T_2)	10 ns	$100 \div 350$ ns	$100 \div 200$ ns	16 ns
Bunch width (T_{bw})	< 2 ns	75 ns	30 ns	8 ns
Ions per bunch (n_i)	≤ 200	≤ 300	≤ 10	≤ 4000
Intensity (I_{max})	10^{10} p/s	$2 \cdot 10^9$ p/s	$5 \cdot 10^7$ ions/s	10^{10} ions/s

TABLE 2.1: Typical time structures of clinical accelerators. The data for cyclotron and synchrocyclotrons is reproduced from Krimmer et al., 2018. The synchrotron data refers to the HIT facility (Haberer et al., 2004).

but not by the lightest ones, such as ^1p or ^4He . The prompt gamma energy spectrum presents discrete lines that are characteristic of the nuclei involved. These lines span up to approximately $E_\gamma = 10$ MeV with production times $T \ll 1$ ns.

2.1.3 Ion beams production

The production of slightly relativistic ion beams requires the employment of advanced particle accelerator technology. All the clinical facilities are nowadays based either on cyclotrons (58 in operation, 31 in construction and 16 in planning stage) or synchrotrons (38 in operation, 13 in construction and 7 in planning stage), the latter being the only solution in clinical use to accelerate any ion heavier than protons (*PTCOG*). Future solutions may include superconducting synchrocyclotrons (1 in construction) or laser acceleration (Owen et al., 2016). The time structure and the beam intensity plays a fundamental role in the detection of the secondary radiation, as most of the background signal is delayed by few nanoseconds ($\Delta t_{\text{bg}} \simeq 5$ ns) with respect to the prompt gamma radiation (Testa et al., 2010). The table 2.1 summarizes the key features of such particle accelerators. To perform time resolved prompt gamma detection one requires either (i) a short bunch containing many ions or (ii) a wide bunch containing few ions. The superconducting synchrocyclotrons do not respect either of the conditions and may be more suited for other techniques that perform data acquisition during the T_1 interval, such as the imaging of short-lived positron emitters (Buitenhuis et al., 2017).

The first condition is respected by the proton cyclotrons. In this case, the arrival time of the single bunches can be directly correlated to the radio-frequency (RF) of the accelerator. There is no need for an additional detector to measure the arrival time of the beam particles. However, proton bunch drifts against the RF of the cyclotron have been observed and re-synchronization is required each time the energy is varied. The very short T_2 makes difficult to clearly separate the background from the prompt gamma,

especially at high proton energies. Nevertheless, such technique is successfully applied by several prompt gamma prototypes. This is possible since $T_{\text{bw}} < \Delta t_{\text{bg}}$ and therefore the prompt gamma radiation is fully acquired before the background radiation starts reaching the detector. The number of particles delivered per single bunch can be particularly high, since the limiting factor is the throughput of the prompt gamma detector. This can be as high as $1 \cdot 10^6$ events per second with modern crystals and electronics (Pausch et al., 2018b).

The second condition is respected by the carbon synchrotrons. Here we observe that $T_{\text{bw}} > \Delta t_{\text{bg}}$. Therefore, the use of the RF signal² to reject the background is unsuccessful. The use of an additional detector to track the arrival time of the single ions is required. In this case, the limiting factor is the throughput of such beam time tracker. The limited number of particles per bunch eases such task. Some solutions have been proposed to cope with the highest beam intensities reached by proton and carbon beams (Magalhaes Martins et al., 2019b; Vignati et al., 2017). Moreover, the long T_1 could be exploited for the data transfer and the long T_2 allows a clear separation of the background from the prompt gamma data.

2.1.4 Physical range uncertainties

To exploit the dosimetric properties of ion beams, the range of the primary particles beams in the patients should be predicted as accurately as possible in the treatment planning and delivery process. Small under- or over-estimations of the stopping power along the path may lead to severe consequences in the dose deposition. While the equation 2.1 provides an accurate model, its parameters are subject to uncertainties. Moreover, the dose calculation algorithms, the stability of the accelerator and of the mechanical components introduce further sources of systematic and random errors. Paganetti, 2012 provided a compilation of the effects. As previously displayed in Figure 1.1, such effect is observed for ion beams and has only a minor impact for photon irradiation. This is due to the steep dose gradient $g = dD/dz$, which at the falloff produces a dose drop from 80% to 20% of its maximum value in a fraction of millimetre (Dal Bello, 2016). The systematic and random errors in the prediction of the Bragg peak position are referred to as range uncertainties.

The consequences of their existence can be summarized either in (i) an under-dosage of the clinical target volume (CTV) or in (ii) an over-dosage of organs at risk (OAR). Different countermeasures are adopted to mitigate these effects. In the first case, safety margins are added and the treatment plan is calculated on a larger target volume, namely the planning target volume (PTV). This approach, based on statistical considerations, ensures that the CTV receives the required dose even in presence of systematic and random errors. The cost to be payed is the delivery of the dose amount intended for the tumor also to the healthy tissue surrounding it. Typical dimensions

²Moreover, the correlation of the bunch arrival time with the RF is partially spoiled by the knock-out extraction process.

of the safety margins have been shown in Figure 1.1. In the second case, the treatment plan is optimized avoiding beam delivery angles pointing directly to OARs. The multi-field or patched-field plans are preferred to a possible optimal single field plan (Knopf et al., 2013). In this way, the steepest gradients g_{\max} are moved from the interface between tumor and healthy tissue to a location inside the PTV. Therefore, a misplacement of the Bragg peak produces an over-dosage in the tumor and not in the OARs. The cost to be payed is the delivery of a less conformal therapy with respect to the achievable dose distributions. Finally, biological effects and complex geometrical inhomogeneities also play a role in range uncertainties. The direct or indirect measurement of the Bragg peak position in the patient aims to solve the limitations and the compromises introduced by the presence of range uncertainties. The following section describes the latest developments in this field.

2.2 Range verification in ion beam therapy

2.2.1 Ion imaging

The stopping power described by equation 2.1 is nowadays calculated having as input data the planning CT, i.e. a tomographic image of the patient obtained through the interaction of photons with energy in the range of $E_{\gamma} = 100$ keV with the tissue. Given the different physics regulating the interaction of keV photons and MeV ions with matter, such conversion is one of the largest source of uncertainties. A better approach predicts the stopping power on the base of a CT image acquired with two different sources, i.e. dual energy CT (Wohlfahrt et al., 2017). The ideal approach would be the direct measurement of the stopping power performing a tomographic image of the patient with the same radiation quality. The use of high energetic ions to perform transmission imaging was proposed in the 1960s (Koehler, 1968) and gained new interest at the end of the 1990s (Pemler et al., 1999) due to the availability of the technology required to satisfy the technical requirements (Schulte et al., 2004). Recent studies demonstrated better predictions when moving from ^1p projectiles to ^4He projectiles (Piersimoni et al., 2018). Nevertheless, ion radiography and tomography has not yet reached the stage of clinical application. Their rapid development promises however a possible application of such technique in the near future to perform pre-treatment imaging. At the cost of little extra dose to the patient, this could improve the stopping power map definition and reduce the range uncertainties connected to CT conversion. The use of ion imaging to perform on-couch verification of the patient anatomy has also been proposed (Martišíková et al., 2018). Other errors such as intra-fractional variations would not be tackled. Graeff et al., 2018 proposed a monitoring technique to be used on-line during ^{12}C treatments. Ion imaging is promising as a solution for reducing the range uncertainties and to perform indirect range verification.

2.2.2 Positron emission tomography

Positron emission tomography (PET) can be used to measure the β^+ activity induced by the ion beam in the patient. The lightest projectiles (^1p and ^4He) can convert the target nuclei into unstable isotopes. This processes happen from the entrance until the cross sections for the nuclear channels drop to zero at the Coulomb barrier. The generated activity is in first approximation constant from the skin until the final range of the primary particles and zero elsewhere. The heavier projectiles (^{12}C and ^{16}O), in addition to the previous mechanism, undergo fragmentation producing lighter unstable isotopes, e.g. ^{11}C or ^{15}O , which production yield is maximum at the lowest kinetic energies. Therefore, the generated activity presents a plateau followed by a peak reaching its maximum shortly before the primary particles range. Such interaction mechanisms offer the potential to retrieve the Bragg peak position with a passive measurement of the activity induced by the primary ion beam. The delivery of additional dose to the patient is not required. Two distinct modalities could be used for range verification via PET: (i) post-treatment imaging or (ii) in-beam imaging.

In the first case, commercially available scanners can be adopted and the development of new detector technology is not strictly required. The patient, after the delivery of the fraction is completed, is moved from the treatment room to the PET scanner. Typical acquisition times can reach up to 30 minutes. The challenges to be faced span from the limited counting statistic orders of magnitude below conventional tracer imaging to physiological washout and the co-registration. Moreover, the imaging of fast decaying isotope is made impossible due to the time required to transfer the patient. Overall, the detection of range shifts is limited to a precision of few millimeters (Handrack et al., 2017).

In the second case, new dedicated technology needs to be developed in order to acquire the coincidence events during beam-on. A first prototype was available during the ^{12}C pilot project at the GSI Helmholtz Centre for Heavy Ion Research in Darmstadt, Germany (Enghardt et al., 2004). A series of complex background rejection techniques need to be employed in this case, as most of the events that reach the detector do not originate from β^+ decays. The long bunch separation (T_2) and intra-spill times (T_1) offered by synchrotron-based facilities are especially beneficial to reject the prompt-gamma and neutron background. The data acquisition during beam-on for the standard cyclotron time structure is impracticable. Recent developments showed promising results for the data acquisition during beam-on conditions at synchrotron based facilities (Bisogni et al., 2017). Nevertheless, in order to acquire sufficient statistics, the data acquisition should be extended several minutes after the fraction delivery is completed (Ferrero et al., 2018). The physiological washout is reduced compared to post-treatment imaging but is still present.

Both solutions (i) and (ii) provide the detection of an error in the dose delivery only few minutes after the treatment fraction is completed. Moreover, the PET data includes the signal from the integral dose deposition and is

hardly suitable for one or few spot-by-spot based range verification. An innovative solution has been proposed and investigated by Buitenhuis et al., 2017. In this case, the effect of physiological washout is negligible since only the short living ^{12}N isotope ($t_{1/2} = 11$ ms) is imaged. However, the synchrotron time structure is not suited for the detection scheme and the cyclotron one needs to be artificially changed to obtain millisecond long beam-off times to perform the data acquisition. On the other hand, superconducting synchrocyclotrons present an optimal irradiation scheme for the ^{12}N imaging. The first few spots of the plan can be imaged without any intense background, as there is no induced activation yet. The remaining spots may be challenging to detect due to the long living β^+ activity induced by the previous irradiation.

2.2.3 Prompt gamma

Note: Parts of this sub-section were also published in the B.I book chapter.

The abundant events that are discarded during beam-on by the PET systems can instead be used to obtain a direct measurement of the Bragg peak location. The processes leading to the generation of the prompt gamma radiation were extensively described in the section 2.1.2. The detection of such radiation is referred to as prompt gamma imaging (PGI). Due to the nearly instantaneous emission only during beam-on condition and to the characteristic energy of the gamma quanta, PGI is suitable for one or few spot-by-spot based range verification and is not affected by physiological washout. Moreover, being the secondary radiation more energetic than the one produced in the β^+ decays, the attenuation inside the human body is smaller. On the other hand, the efficient detection of high energy gamma radiation is challenging and several different techniques have been suggested for this purpose.

The PGI as a technique for on-line verification of the ion range in particle therapy was first proposed by Jongen et al., 2003. Few years later, Min et al., 2006 presented the first experimental results from a 38 MeV proton beam. Afterwards, many groups emerged around the world trying to verify in-vivo and on-line the range of the particle beams inside the patient. The leading groups were the ones in Boston (Verburg et al., 2014), Belgium (Smeets et al., 2012), Delft (Biegun et al., 2012), Dresden (Golnik et al., 2014), Korea (Min et al., 2006), Lyon (Testa et al., 2008), Maryland (Polf et al., 2009), Milan (Mattei et al., 2017), and Munich (Aldawood et al., 2017). Each of these groups specialized in different approaches to develop a device capable to perform direct measurements of the Bragg peak position with millimetric accuracy.

The knife-edge slit camera was first applied in the clinical setting by Richter et al., 2016. The prompt gamma spectroscopy (PGS) is, on the other hand, planned for clinical use later this year (Hueso-González et al., 2018). In a first phase, the passive detection of the radiation is planned and the course of the treatment is not influenced. Other devices are also heading towards clinical application by taking advantage of different features of the detection method, such as prompt-gamma timing or Compton camera.

Min et al., 2006 proposed a multilayered collimator system to locate the distal falloff in proton therapy. Such a system would capture neutrons and prevent unwanted gammas while measuring at right angles the prompt-gamma component resulting from the interaction of the proton beam with the patient tissue. One year later, a prototype composed by a collimator and a CsI(Tl) scintillator detector showed for the first time a clear correlation between the distribution of the prompt gammas and the location of the distal dose edge for a $E_{\text{kin}} = 38$ MeV proton beam, thus confirming the previous simulations with Monte Carlo (Min et al., 2007). A spatial resolution of ≤ 2 mm was already envisioned at that time. Further developments lead to the Monte Carlo investigation of a full-scale multislit collimation system for all therapeutic proton energies (Min et al., 2012). This system requires however a two-dimensional distribution of the proton dose with 2D position sensitive gamma detectors and lacks so far enough statistics when compared to the other available systems.

Smeets et al., 2012 presented a pioneering prototype and methods for verification of the proton range through a slit camera. The experimental work followed thorough Monte Carlo simulations that defined the main geometrical parameters for a system to be operated in presence of a proton beam at $E_{\text{kin}} = 160$ MeV. A range estimation of 1-2 mm standard deviation was achieved in an homogeneous PMMA phantom. This prototype has been acquired by IBA³ and evolved to a clinical prototype that was tested in humans for the first time by Richter et al., 2016. Such investigations demonstrated great accuracy in the measurement of relative shifts between fractions.

A more elaborated technique, based on specific nuclear channels and isomeric transitions was proposed by Verburg et al., 2012. Such approach used the spectrum of the prompt-gamma emission to retrieve an absolute range verification of the proton beam. Further experimental work demonstrated the feasibility of measuring the discrete prompt-gamma rays for in-vivo range verification of clinical proton beams. The differential cross-sections were measured for 15 prompt gamma-ray lines from proton-nuclear interactions with ^{12}C and ^{16}O up to 150 MeV and an absolute range was determined with a standard deviation of 1.0–1.4 mm (Verburg et al., 2014). The full scale prototype, dedicated to protons accelerated by cyclotrons is close to its first clinical application (Hueso-González et al., 2018).

A novel concept of prompt gamma-ray timing (PGT) has been proposed by Golnik et al., 2016. This is an uncollimated method that uses a gamma-ray detector of reasonable time resolution for measuring the finite transit time from entering the patient's body until stopping in the target volume. The underlying principle is the increasing transit time with the particle range that causes measurable effects in the PGT spectra that can be used for range verification. This method has been demonstrated at a clinical proton facility and range differences of 5 mm in defined heterogeneous targets were identified with a single detector and 10^8 incident protons (Hueso-González et al., 2015). However, PGT spectra were observed to be smeared out by the bunch time

³Ion Beam Applications SA, Louvain-la-Neuve, Belgium

spread and accelerator related proton bunch drifts against the RF of the accelerator have been detected. A proton bunch monitor has been therefore developed to correct for potential bunch drifts and increase the robustness of the PGT method. Nevertheless, this technique is highly dependent on the number of gamma rays detected per incident proton. Large detector loads and a high acquisition throughput are therefore mandatory to draw statistically significant conclusions on range errors.

The Compton camera (CC) belongs to the electronically collimated systems and it requires position-sensitive gamma ray detectors with high resolution and efficiency, which are arranged in one scatterer, one absorber, or in several scatter planes. In contrast to the other PGI systems, it allows for two-dimensional or even three-dimensional images to be reconstructed as more gamma-rays and directions can be detected. However, the event coincidence needed between the different stages limits the overall efficiency. The major pitfalls are its highly demanding instrumentation in term of spatial, time and energy resolution and the computationally intensive reconstruction algorithms. The challenges include also technical complexity, electronics expense, low coincident efficiency, high detector load, radiation background, and the elevated percentage of random coincidences. Draeger et al., 2018 are close to reach a clinical prototype . Recent results reported prompt-gamma measurements with a small CC prototype placed at three different locations along the proton beam path. The data were combined to simulate measurements with a larger scale, clinical CC capable of imaging Bragg peak shifts for both hypo-fractionated and standard treatments. 3D images of the prompt gamma emission were produced and range shifts of 2 mm were detected for the delivery of a 2 Gy spot.

2.2.4 Other techniques

Further techniques have been applied or are under investigation for measuring in-vivo the Bragg peak position. Some of these are based on well established technology, such as MR or ultrasound imaging. Other are site specific or focus on the tracking of different secondary products of the nuclear inelastic reactions. A brief overview of such techniques is here provided.

The nuclear inelastic collisions produce several secondary particles that have enough energy to leave the patient and reach an external detector. Ytre-Hauge et al., 2019 investigated with Monte Carlo methods the correlation of secondary neutrons with the beam particle range. While the neutron production site was proven to be well correlated with the Bragg peak position, the efficient detection of high energetic neutrons to reconstruct the vertex of origin remains challenging. The opposite applies to charged secondaries, such as protons, which could be detected with a nearly $\epsilon = 1$ efficiency. Félix-Bautista et al., 2019 experimentally demonstrated the correlation between secondary protons and the transverse position of the beam during a pencil beam scan plan delivery. The correlation with the longitudinal Bragg peak position is still under investigation. The major challenges to be faced are the wide energy spectrum of the secondary proton, the angular spectrum

peaked in the forward direction and the loss of information on the vertex of origin due to multiple Coulomb scattering within the patient.

The pulsed and localized delivery of energy to a medium generates localized heating and therefore a thermoacoustic signal. This could be detected with ultrasound imaging devices along with the anatomic structures (Kellnberger et al., 2016). Millimetre range resolution is achievable in homogeneous media, given that the beam structure is artificially modified to obtain high intensity pulses ($I \geq 1$ pC) in short times ($\Delta t \leq 1 \mu\text{s}$) to maximize the acoustic emission. Moreover, significant changes in the MRI signal have been observed for the irradiated parts of the spine (Gensheimer et al., 2010) and the liver (Yuan et al., 2013). Such results show the feasibility of using MR-imaging to retrospectively determine the location of the dose deposition in follow-up studies. The common feature of the techniques presented in this paragraph is that the patient anatomy is imaged along with the energy deposition location.

Finally, site specific dose and range monitors have been developed. These techniques usually require the invasive introduction of a sensor in the patient either through surgery or in a body cavity. Several solutions have been proposed based on fiducial markers containing a MOSFET sensor and a wireless transmitter (Lu et al., 2010) or fiducial markers with selected materials having high yield of β^+ emitters upon proton irradiation to facilitate post-treatment imaging (Cho et al., 2013). Also, the use of diodes within a rectal balloon has been investigated and commissioned for clinical application (Hoesl et al., 2016). The common challenge of such techniques is that the energy deposition is not measured along a profile but at one unique point. This creates ambiguity on the actual Bragg peak position that has to be solved with the additional detection of an independent signal or comparing multiple independent measurements.

2.3 State-of-the-art prompt gamma technology

A compilation of the state of the art for the most advanced prompt gamma prototypes is provided in Table 2.2. The physical principles are also listed. It should be noticed that, except for prompt gamma spectroscopy, all technologies have been designed focusing on the physical interaction of the photons with devices external to the human body. On the other hand, prompt gamma spectroscopy is based on specific nuclear interactions happening at the location of interaction of the beam particles with the tissue. Only the gamma rays that travel directly to the detector without undergoing further interactions are collected among the data events, while the others are treated as noise. Therefore, the direct characterization of the nuclear process generating the secondary gamma rays is accessible through PGS. As previously shown in Figure 2.1, the cross section is a monotonic function of the residual kinetic energy in the last few millimeters. Given the energy-range relation for ion beams (equation 2.2) and by measuring the intensity of the gamma

	Physical principle	Detected quantity	Prototype stage
knife-edge slit camera	straight line gamma ray tracing	intensity profile integrated over the energy	patient test performed (relative 1D deviations)
prompt gamma spectroscopy	specific nuclear channels and de-excitation lines	intensity spectral lines at one or few locations	patient test planned (absolute 1D deviations)
Compton camera	Compton scattering	energy and location of the scattered gamma and electron	approaching clinical prototype (relative 3D deviations)
prompt gamma timing	time-of-flight	time differences between the gamma from shallow and deep locations	approaching clinical prototype (relative 1D deviations)
multi-slit collimated system	position-dependent attenuation of the gamma radiation	intensity profile integrated over the energy	used in the past to demonstrate PGI (relative 1D deviations)

TABLE 2.2: Overview of the most advanced prompt gamma imaging prototypes and their stage of development towards clinical application.

de-excitation lines, prompt gamma spectroscopy is the only technique having the potential to measure the absolute instead of the relative position of the Bragg peak.

The devices previously listed have been developed towards the application of PGI to protons beams accelerated by cyclotrons. The studies involving synchrotron facilities or heavier ions at were so far scarce. The investigation was limited to the total production yield in either collimated (Pinto et al., 2014) or un-collimated (Mattei et al., 2017) setups. The development of systems dedicated to synchrotron facilities aiming to perform range verification of proton and heavier ions is so far missing.

The sound physics base of the technique and the lack of studies at synchrotron facilities call for the development of prompt gamma spectroscopy for ^1p , ^4He , ^{12}C and ^{16}O beams.

Chapter 3

Overview of the results

The results presented in this thesis have been obtained during multiple investigations having a common final goal, namely the development of a prompt gamma spectroscopy pre-clinical prototype to be operated in presence of ^1p , ^4He , ^{12}C and ^{16}O beams at a synchrotron facility. Several challenges needed to be faced and the techniques applied to proton beams accelerated by cyclotrons could not always be directly translated into this work. The most significant differences can be summarized in the following four points:

1. There is a lack of experimental data for double differential cross sections for prompt gamma production of ^1p , ^4He , ^{12}C and ^{16}O projectiles on the light nuclei composing the human body. Therefore, the theoretical models implemented in the Monte Carlo codes are generally not benchmarked.
2. The presence of light fragments along with the primary beam particles generates additional prompt gamma signal, which is not directly correlated to the Bragg peak position.
3. The Doppler broadening of the gamma radiation originated in the isomeric transitions following the nuclear excitation induced by projectiles heavier than protons may limit the applicability of the spectroscopy technique.
4. The time structure of a synchrotron requires the employment of an external trigger to perform time resolved prompt gamma measurements.

Such points were used to structure the work towards the final results presented in this thesis. Motivated by the first point, this project was based primarily on experimental work. The additional uncertainty introduced by the increased Doppler broadening led to avoid adopting scintillating crystals with intrinsic activity, which are limited to the detection of gamma radiation only above few MeV (e.g. LaBr_3). In absence of intrinsic activity it is theoretically possible to detect the prompt gamma rays over their full energy spectrum and therefore aim to compensate for the lower signal to background ratio induced by the Doppler broadening. The choice fell on the novel CeBr_3 scintillating crystal, which has only recently reached the commercial distribution.

The publication A.V proposed and experimentally investigated for the first time the use of CeBr_3 scintillating crystals for prompt gamma spectroscopy. The results were promising but it was observed that the single and double escape peaks were often more intense than the photopeaks. Also, the Doppler continuum component was significant and substantially decreased the spectroscopy performances in the low energy component of the spectrum.

The publication A.IV was a Monte Carlo study that focused on the optimization of the geometry of the CeBr_3 scintillating crystals and the introduction of secondary crystals for background rejection. The aim was the maximization of the signal to background during the detection of the gamma spectral lines induced by ^4He beams in different materials. The nuclear interaction models implemented in the Monte Carlo simulations were chosen to obtain a realistic prompt gamma spectrum but were not optimized to precisely reproduce the experimental data, as the focus of this study was the optimization of the sole spectroscopic unit.

The optimized spectroscopic unit was then tested during several experiments in presence of ^4He beams at the HIT facility. Its performances were compared with the Monte Carlo predictions and presented in the publication A.III. The experimental setup included a non-optimized plastic scintillator to provide the time of flight information for the incoming primary ions. This was limited to low beam intensities but served to the purpose of the characterization of the spectroscopic unit.

A more advanced beam trigger was developed and experimentally characterized in the publication A.II. Its efficiency and time resolution were analyzed for all the ion species available at the HIT facility and demonstrated for the application to time resolved prompt gamma spectroscopy. The detector was designed to be scalable to larger areas and higher intensities, providing a novel solution to the problem of single particle tracking for clinical particle accelerators. For this reason, the patent application P.I was filed to the United States Patent and Trademark Office.

Finally, the spectroscopy unit characterized in the publication A.III and the beam trigger presented in publication A.II were included in the full experimental setup investigated in the publication A.I. The setup was used to perform experiments with all the ion beams available at the HIT facility and the information extracted from the energy spectra was correlated to the Bragg peak position. This article also provided a definitive answer to the second and third issues raised in the previous list. As a matter of fact, the amplitude of the Doppler broadening was parametrized against the projectile mass and a technique was developed to partially suppress the prompt gamma signal generated by the light fragments. The final results demonstrate the possibility to measure the absolute Bragg peak position with prompt gamma spectroscopy at a synchrotron facility. Following these results, a novel geometry for prompt gamma detection was filed in the patent application P.II filed to the European Patent Office.

The studies presented in the journal articles A.I-A.V provide a systematic investigation of the four points raised at the beginning of this chapter.

Chapter 4

Publications

This thesis is presented in cumulative format in accordance with the regulations of the Department of Physics and Astronomy of Heidelberg University. It comprises five articles published in or submitted to internationally acclaimed peer-reviewed journals. The individual articles are referred to within this thesis by the letter "A" followed by roman numerals. The author of this thesis is first author of the publications A.I, A.III and A.IV and second author of publications A.II and A.V. Three manuscripts have been published (A.III, A.IV and A.V) and another two are currently under review (A.I and A.II). A detailed list of authors' contributions precedes each of the publications. Moreover, the development of the doctoral project led to the filing of two patent applications (P.I and P.II) and the production of a book chapter (B.I). The author of this thesis is among the inventors for the patent applications and is a co-author of the book chapter. Their complete references are presented at the end of the thesis. As required by the regulations of the Faculty, the publications with first authorship have not been used and will not be used for any other dissertation. The current chapter presents the five manuscript with unaltered content and edited formatting to be conform with the rest of the thesis.

4.1 Proposal of a novel scintillator for prompt gamma spectroscopy

Title : Prompt gamma spectroscopy for range control with CeBr₃

Authors : Paulo Magalhaes Martins, Riccardo Dal Bello, Andreas Rinscheid, Katja Roemer, Theresa Werner, Wolfgang Enghardt, Guntram Pauch and Joao Seco

Status : Published

Journal : Current Directions in Biomedical Engineering, 3(2), pp. 113-117, 2017

DOI : 10.1515/cdbme-2017-0023

Copyright : © 2017 De Gruyter, Berlin/Boston. Reproduced with permission. Permission request number: 11850787. All rights reserved.

Contributions : R.D.B. contributed to design the experiments with the support of Monte Carlo simulations. This was critical especially for the experiments involving a collimator, where the optimal tradeoff between statistics and neutron-induced noise had to be chosen. The first author, P.M.M., designed and conducted the experiments and the post-processing of the data. The last three authors, W.E., G.P. and J.S., coordinated the project between the different institutions. The remaining co-authors provided support with the experimental setup, mainly with the readout electronics. After the experimental campaigns, R.D.B. contributed to the data interpretation. He contributed especially to the interpretation of the experiments including the collimators, where it was observed a steeper fall-off of the high energy gamma lines in presence of the semi-collimated setup compared to the slit collimation. At the end of the article P.M.M., R.D.B. and the other co-authors concluded that the implementation of an active anti-coincidence shielding would be beneficial for improving the background rejection. This topic is investigated in the following publication.

Prompt gamma spectroscopy for range control with CeBr_3

Abstract

The ultimate goal of radiotherapy using external beams is to maximize the dose delivered to the tumor while minimizing the radiation given to surrounding healthy critical organs. Prompt Gamma Spectroscopy (PGS) has been proposed for range control of particle beams along with the determination of the elemental composition of irradiated tissues. We aim at developing a PGS system for the German Cancer Research Center – DKFZ that takes advantage of the superior selectivity of Helium and Carbon beams accelerated at the Heidelberg Ion-Beam Therapy Center. Preliminary tests with protons accelerated with an IBA C230 cyclotron located at the Universitäts Protonen Therapie Dresden were performed at OncoRay - National Center for Radiation Research in Oncology. We present results obtained with a PGS system composed of CeBr_3 detectors ($\varnothing 2'' \times 2''$) and ($\varnothing 1.5'' \times 3''$) coupled to a Hamamatsu R13089 photomultiplier tube and plugged to a Target U100 Spectrometer. Such system provides accurate time-of-flight measurements to increase the signal-to-noise ratio relative to neutron-induced background. First measurements resulted from the irradiation of PMMA and water phantoms, and graphite and aluminum bricks. Several PG energy lines ranging from 0.511 MeV up to 8 MeV were identified and compared with reference results. Two further experiments consisted in irradiating PMMA phantoms in a slit- and semi-collimated configuration with mono-energetic proton beams of 165 MeV and 224 MeV, respectively. Results acquired by means of transversal PGS at different phantom depths, ranging from 6 cm before the Bragg peak (BP) to 3.5 cm beyond the BP in 5 mm steps with a 1 cm slit collimation (tungsten) showed a slight decrease of PG yields after the BP. Similar measurements with a semi-opened collimation configuration demonstrated a steeper decrease of PG yields after the BP.

Introduction

Over the last 25 years, millions of euros/dollars were spent without any successful solution to proton range errors (Knopf et al., 2013). The major consequence of these range errors is that significantly larger high dose regions are created around the tumor with severe consequences to the patient. Prompt gamma imaging (PGI) has been proposed as a superior method to

Positron Emission Tomography (PET) for range verification, with the potential to achieve 1 mm uncertainty in the positioning of the Bragg peak within the patient (Moteabbed et al., 2011). PGI allows real-time range verification and does not suffer from biological washout or motion effects. In addition, a significantly higher PG production and closer correlation with dose profiles due to higher cross-sections makes it more attractive than PET. A novel approach for measuring prompt gammas, combining energy- and time-resolved detection has been proposed by Verburg et al., 2014. Besides using the prompt gamma signal for range verification, the emitted gamma spectrum allows determining the elemental composition of irradiated tissue. The characterization of CeBr₃ detectors for usage as PG monitors in particle therapy has been firstly accomplished by Roemer et al., 2015. Such detectors were systematically investigated by Pausch et al., 2016 and firstly applied to prompt gamma timing (PGT). In this work, we propose to use CeBr₃ scintillators for prompt gamma spectroscopy (PGS).

Materials and methods

Experimental setups

The measurements were divided in three campaigns. In the first campaign, Water and PMMA phantoms and a Graphite Brick were irradiated with a mono-energetic proton beam of 130 MeV. For the Aluminum brick we adjusted the energy to 90 MeV. The schematics of the experimental setup is depicted in Figure 4.1). The detection system was composed of a CeBr₃ detector ($\varnothing 2'' \times 2''$) coupled to a Hamamatsu R13089 photomultiplier tube and plugged to a Target U100 Spectrometer (*Target Systemelektronik*). The system was located at 90° with respect to the beam, at a distance of 50 cm and aligned with the Bragg peak position. The energy spectrum was calibrated with a ²²Na source and the photomultiplier voltage was adjusted accordingly. In the second campaign, a tungsten collimator with a thickness of 5 cm was placed between the PMMA phantom and the detecting system. The scheme is shown in Figure 4.1). The phantoms were placed on a moving platform and displaced in 5 mm steps covering a region from 6 cm before the BP up to 3.5 cm after the BP. In the last campaign, we used different CeBr₃ detectors ($\varnothing 1.5'' \times 3''$) and doubled the collimator thickness in a semi-collimation configuration, see Figure 4.1). We also acquired for several detector positions along the beam range covering a region from 9 cm before the BP until 9 cm after the BP. We irradiated a PMMA phantom with the maximum energy available - 224 MeV. Figure 4.2 shows a photograph of the setup in campaign 2 and 3. We set a beam current of 0.4 nA measured at the ionization chamber and an acquisition time of 50 s for both campaigns. The observed throughput rates for the 3 campaigns varied between 300 and 500 kcps with a busy time of 30 – 50% as indicated by the U100. The spectrometer streamed acquired data in list-mode format to a server which then saved them in binary files containing the time stamp (64-bit integers) and the energy information

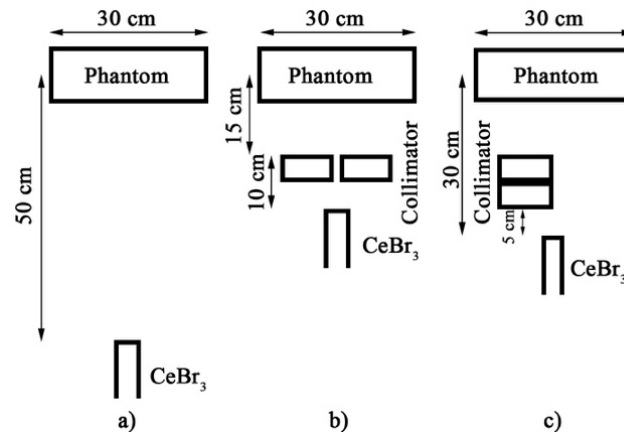


FIGURE 4.1: Schematic drawing of the three campaigns for the prompt gamma acquisition from proton-irradiated phantoms using: a) no collimation; b) slit collimation; c) semi-collimation.

(32-bit floats). This data was further analysed with MATLAB and ROOT (version 5.34.00, CERN, Geneva, Switzerland). The accelerator radio-frequency (RF) has been used for timing information as external reference clock. The detailed specifications of the detection system are reported in a more comprehensive work (Pausch et al., 2016).

Results

No collimation

Figure 4.3 shows a 2D histogram with the energy- and timeresolved prompt gammas emitted from water, PMMA and graphite targets irradiated in campaign 1, see Figure 4.1). The prompt gamma lines and corresponding single- (SE) and double-escape (DE) peaks are visible as horizontal stripes. Several time-uncorrelated lines are also visible (e.g., the 511 keV line from positron annihilation and the 2.2 MeV line resulting from hydrogen neutron capture).

Energy spectra

Figure 4.4 shows the energy spectra within 5 ns and 6 ns for the water (I) and PMMA (II) phantoms and the graphite (III) brick irradiated in campaign 1, see Figure 4.1). The energy peaks are related to reactions with material nuclei or characteristic transitions from excited states as a result of the interaction with the proton beams. In table 1, we identified 17 transitions or reactions for the three irradiated materials (targets) and compared with the reference values (Kozlovsky et al., 2002).

Metal spectroscopy

Several metals are used as implants in orthopaedics and dentistry. They are mainly made of titanium and gold and affect the proton range due to their

Transition / Reaction	Target	Reference Line [MeV]	Measured [MeV]
β -decay	I, II, III	0.511	0.509
$^{10}\text{B}_{0.718}^* \rightarrow ^{10}\text{B}_{g.s.}$ / $^{12}\text{C}(p,x)^{10}\text{B}^*$	I, II, III	0.718	0.718
$^{10}\text{B}_{1.740}^* \rightarrow ^{10}\text{B}_{0.718}^*$ / $^{12}\text{C}(p,x)^{10}\text{B}^*$	I, II, III	1.022	1.028
$^{14}\text{N}_{3.948}^* \rightarrow ^{14}\text{N}_{2.313}^*$ / $^{16}\text{O}(p,x)^{14}\text{N}^*$	I, II	1.635	1.636
$^{11}\text{C}_{2.000}^* \rightarrow ^{11}\text{C}_{g.s.}$ / $^{12}\text{C}(p,x)^{11}\text{C}^*$	I, II, III	2.000	2.012
$^{11}\text{B}_{2.125}^* \rightarrow ^{11}\text{B}_{g.s.}$ / $^{12}\text{C}(p,x)^{11}\text{B}^*$	I, III	2.124	2.124
$^{14}\text{N}_{2.313}^* \rightarrow ^{14}\text{N}_{g.s.}$ / $^{16}\text{O}(p,x)^{14}\text{N}^*$	I, II	2.313	2.324
$^{16}\text{O}_{8.872}^* \rightarrow ^{16}\text{O}_{6.130}^*$ / $^{16}\text{O}(p,p')^{16}\text{O}^*$	I, II	2.742	2.788
$^{12}\text{C}_{4.439}^* \rightarrow ^{12}\text{C}_{g.s.}$ / $^{12}\text{C}(p,p')^{12}\text{C}^*$	I, II, III	3.416	3.436
$^{13}\text{C}_{3.685}^* \rightarrow ^{13}\text{C}_{g.s.}$ / $^{16}\text{O}(p,x)^{13}\text{C}^*$	II	3.684	3.684
$^{12}\text{C}_{4.439}^* \rightarrow ^{12}\text{C}_{g.s.}$ / $^{12}\text{C}(p,p')^{12}\text{C}^*$	I, II, III	3.927	3.924
$^{15}\text{O}_{5.181}^* \rightarrow ^{15}\text{O}_{g.s.}$ / $^{16}\text{O}(p,x)^{15}\text{O}^*$	II	4.158	4.167
$^{12}\text{C}_{4.439}^* \rightarrow ^{12}\text{C}_{g.s.}$ / $^{12}\text{C}(p,p')^{12}\text{C}^*$	I, II, III	4.438	4.427
$^{15}\text{N}_{5.270}^* \rightarrow ^{15}\text{N}_{g.s.}$ / $^{16}\text{O}(p,x)^{15}\text{N}^*$	I, II	4.758	4.756
$^{15}\text{O}_{5.181}^* \rightarrow ^{15}\text{O}_{g.s.}$ / $^{16}\text{O}(p,p')^{15}\text{O}^*$	I, II	5.180	5.204
$^{16}\text{O}_{6.130}^* \rightarrow ^{16}\text{O}_{g.s.}$ / $^{16}\text{O}(p,p')^{16}\text{O}^*$	I, II	5.618	5.612
$^{16}\text{O}_{6.130}^* \rightarrow ^{16}\text{O}_{g.s.}$ / $^{16}\text{O}(p,p')^{16}\text{O}^*$	I, II	6.129	6.076

TABLE 4.1: Comparison of measured energy peaks for characteristic transitions/reactions with reference values.

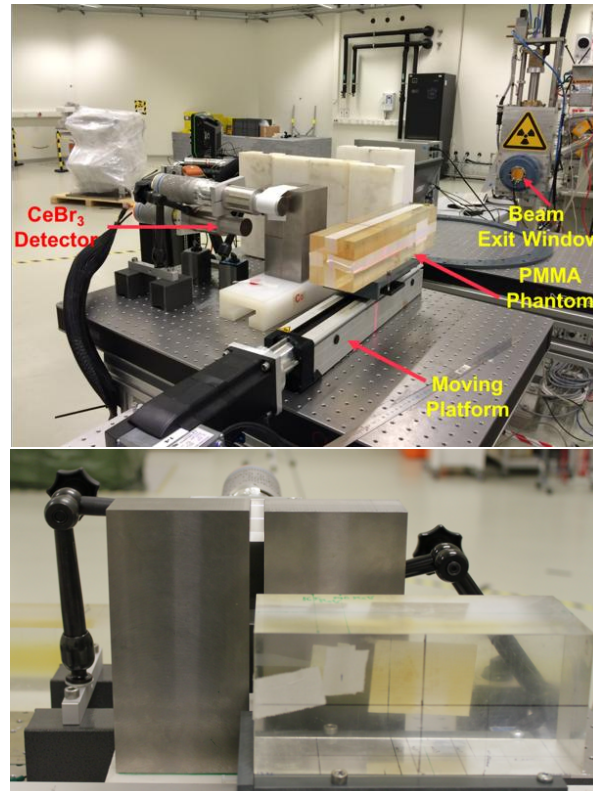


FIGURE 4.2: Photos of campaign 2 (bottom) – slit collimation, and 3 (top) – semi-collimation

high stopping power. Prompt gamma spectroscopy may have a role in the range control in the presence of materials with higher atomic number. Figure 4.5 shows the prompt gamma lines resulting from the irradiation of an Aluminum brick with a proton beam with an energy of 90 MeV. The energy spectrum for the interval 5 – 6 ns is shown in Figure 4.6. The energy peaks agree with the values reported by Foley et al., 1962.

Slit collimation and semi-collimation

Figure 4.7 shows the prompt-gamma lines from a slit collimated configuration for an interval of 1.5 ns and at different positions before and after the BP (5 mm steps). The event counts are represented in logarithmic scale (top). An energy cut in lines below 2 MeV was applied in the linear-scaled histogram (bottom) for better visualization. It clearly shows the 4.4 MeV line from carbon de-excitation and corresponding SE and DE peaks. As expected, those are the most intense lines and a reduction in the prompt gamma yields after the BP is observed. Figure 4.8 shows the prompt-gamma lines from a semi-collimated configuration for the same time interval at 25 positions before and after the BP. The linear histogram (bottom) shows a steeper decrease of the prompt gamma yields after the BP than with the slit collimation. This may be due to the thickness of the collimator, which lets a fraction of gamma-rays through it.

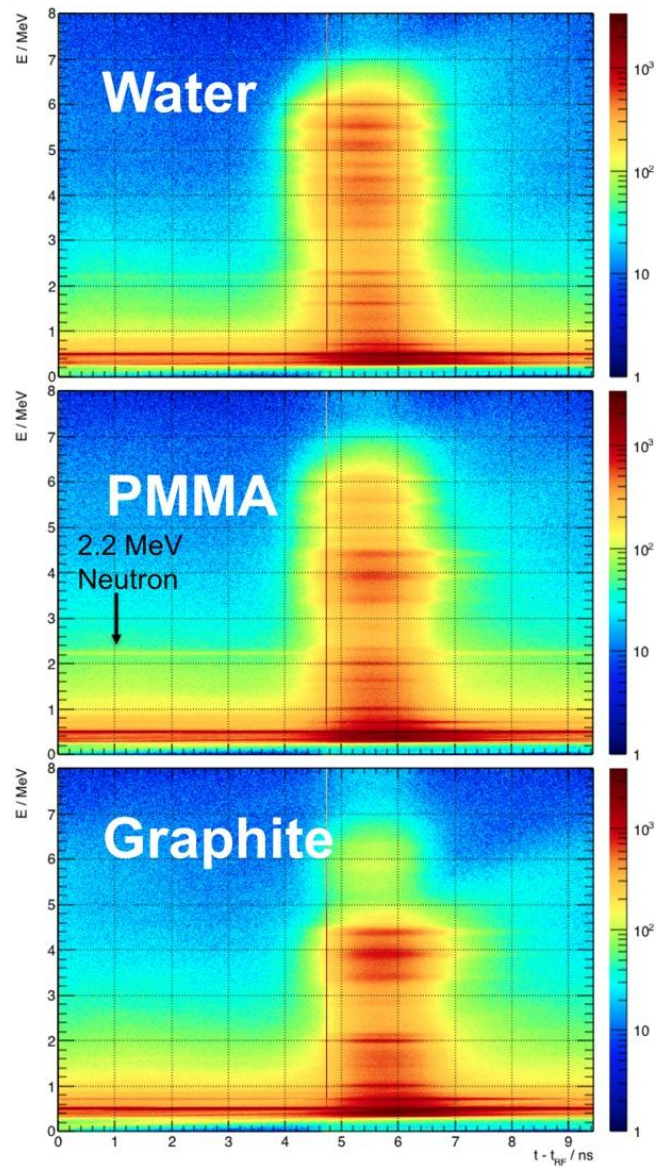


FIGURE 4.3: Prompt gamma lines and corresponding single- and double-escape peaks visible as time correlated horizontal stripes. The targets were irradiated with a mono-energetic proton beam of 130 MeV in a setup without collimation.

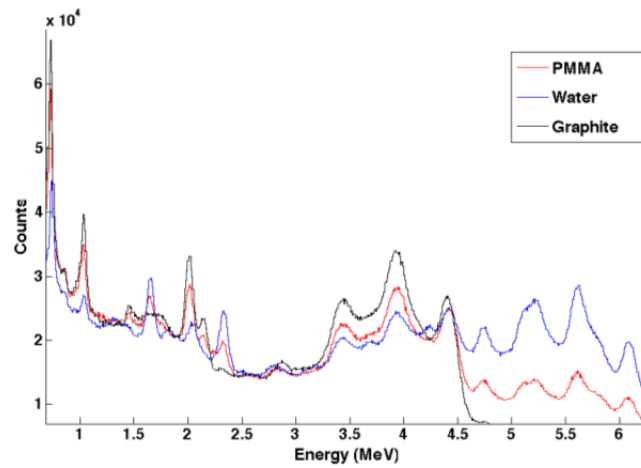


FIGURE 4.4: Energy spectra corresponding to prompt-gamma rays resulting from the irradiation of PMMA, water and graphite for the interval 5 – 6 ns.

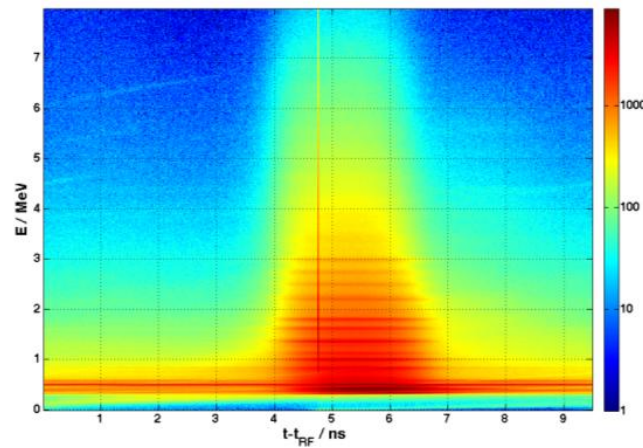


FIGURE 4.5: Prompt gamma lines resulting from the irradiation of Aluminum with protons ($E = 90$ MeV).

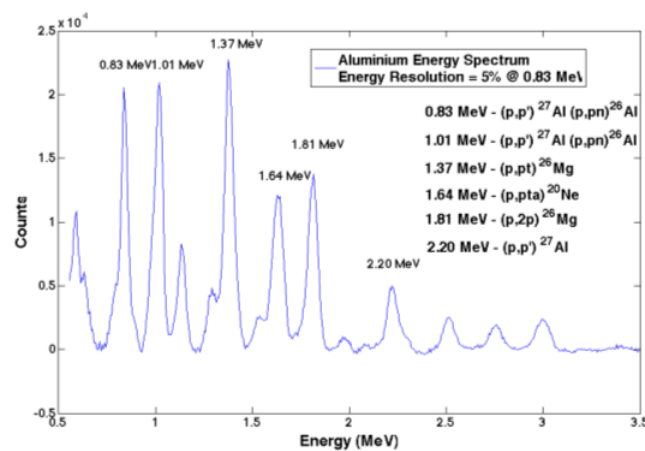


FIGURE 4.6: Energy spectrum corresponding to prompt gamma-rays from proton irradiation of aluminium. The six reactions that are believed to be responsible for their production are also shown.

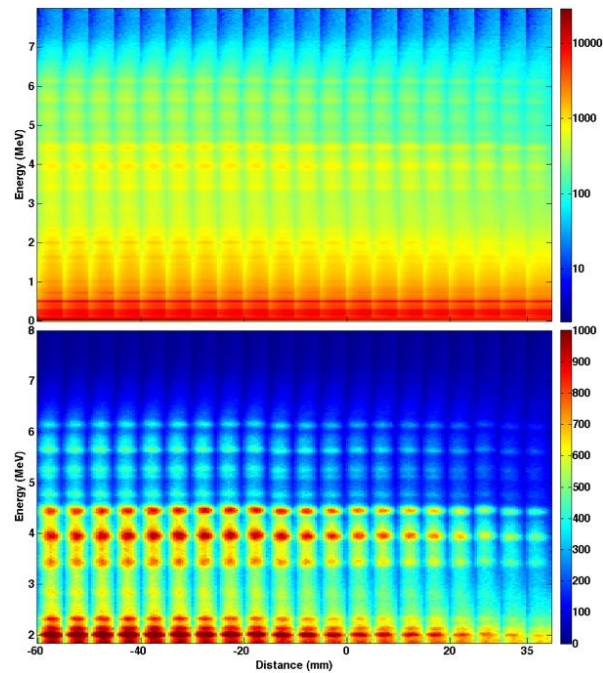


FIGURE 4.7: Energy lines of slit-collimated prompt-gammas resulting from the irradiation of PMMA with protons ($E = 165$ MeV) along 20 positions before and after the BP (zero). Top: Logarithmic scale, full energy range. Bottom: Linear scale, energy cut at 2 MeV.

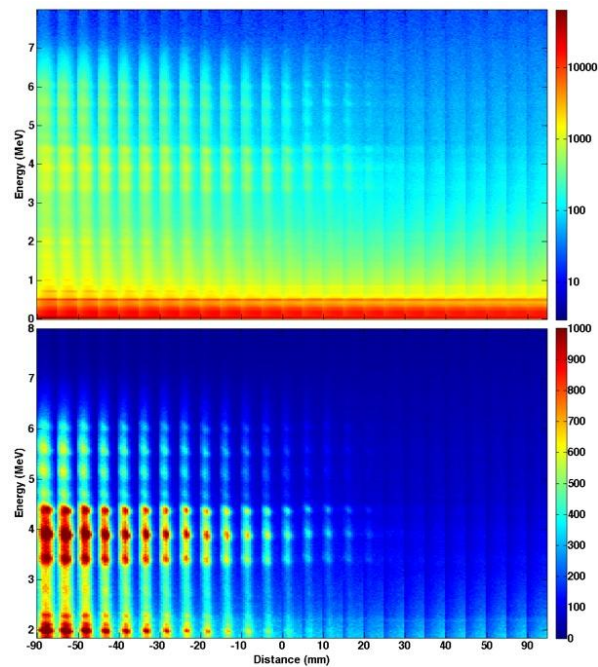


FIGURE 4.8: Energy lines of semi-collimated prompt-gammas resulting from the irradiation of PMMA with protons ($E = 224$ MeV) along 25 positions before and after the BP (zero). Top: Logarithmic scale, full energy range. Bottom: Linear scale, energy cut at 2 MeV.

Discussion

We accomplished three campaigns, where several materials have been irradiated with proton beams in the energy range from 90 to 224 MeV. In the first campaign, we had no collimator between the target and the detection system. Due to the good ToF capabilities of this system, we observed an energy-time correlation of prompt-gammas. This allowed the subsequent time window selection with a significant reduction of background events and the identification of prompt gamma lines. Time-uncorrelated energy lines were also observed. We also observed that the energy spectra corresponding to prompt gamma-rays from the irradiation of Water and PMMA phantoms and a graphite brick shows a significant agreement within the energy peaks positions. A total of 17 reactions or transitions that are believed to be responsible for the production of such prompt-gamma rays were identified and compared with reference values. Moreover, six additional reactions were identified from the irradiation of an Aluminum brick. This may open doors for the application of this system in clinical scenarios where metal implants of high-Z materials, such as titanium and gold, are present. We performed 2 further campaigns with slit- and semi-collimation configurations. The third campaign had doubled tungsten collimator thickness in comparison with the second campaign, which contributed to the better efficacy in the collimation and therefore a steeper gradient in the number of detected prompt-gammas after the BP. Some residual prompt-gamma detection was observed with a higher prominence for the 4.4 MeV and SE and DE peaks. Such geometry coupled with such detection system seems to be promising in the range control of particle beams through PGS. Future work includes the implementation of an active anti-coincidence shielding for background reduction and the systematic comparison of different detector sizes for an optimized prompt-gamma data collection.

Acknowledgment

The authors would like to thank the support from Ion Beam Applications S.A. (IBA).

Author's Statement

Research funding: The authors state no funding involved. Conflict of interest: Authors state no conflict of interest. Informed consent: Informed consent is not applicable. Ethical approval: The conducted research is not related to either human or animals use.

4.2 Monte Carlo optimization of the spectroscopic unit

Title : CeBr₃ scintillators for ⁴He prompt gamma spectroscopy: Results from a Monte Carlo optimization study

Authors : Riccardo Dal Bello, Paulo Magalhaes Martins and Joao Seco

Status : Published

Journal : Medical Physics, 45(4), pp. 1622-1630, 2018

DOI : 10.1002/mp.12795

Copyright : © 2018 American Association of Physicists in Medicine. Reproduced with permission. Permission request number: 4667071481088. All rights reserved.

Contributions : R.D.B. designed and wrote the code to perform the Monte Carlo simulations. The last author, J.S., coordinated the project and provided guidance in order to focus the study on the development of a detection system with clinical relevance. R.D.B. conducted the post-processing of the data generated by means of the Monte Carlo simulations and he wrote the software to extract the optimization parameters. The second author, P.M.M., contributed to the interpretation of the results and developed together with the other authors the discussion on their consequences. R.D.B. finalized the data analysis, wrote the software to export the plots included in the article and wrote the article. R.D.B. and the co-authors concluded that the use of the optimized anti-coincidence detector is beneficial. Its experimental realization is the topic of the following publication.

Abstract

Purpose: Range uncertainties limit the potential of charged particle therapy. *In vivo* and online range verification techniques could increase the confidence in the dose delivery distribution and lead to more conformal treatments. Prompt gamma imaging and prompt gamma spectroscopy (PGS) have been demonstrated for such purpose. The successful application of these techniques requires the development of a dedicated detector system optimized to the radiation energy ranges and the intensity. In this work we investigated a detector system based on CeBr₃ crystals capable of performing spectroscopy of the prompt gamma radiation induced by ⁴He beams.

Methods: We performed Monte Carlo simulations to optimize the detector system. The study was carried out both with the Geant4 toolkit and the FLUKA package. The simulated system consisted of a primary crystal for spectroscopy and secondary crystals for noise reduction in anti-coincidence (AC). For comparison purposes, we considered a configuration without AC crystals. We first defined the dimensions of the primary cerium bromide (CeBr₃) crystal and the secondary bismuth germanate (BGO) or CeBr₃ crystals. We then evaluated their detection performance for mono-energetic gamma radiation up to 7 MeV in such way that the probability of the photo peak detection was maximized in comparison to the number of escape peak and Compton events. We simulated realistic prompt gamma radiation spectra induced by ⁴He beams on homogeneous targets (water, graphite and aluminum) and on implants (water with an aluminum insert). Finally, we tested the performances of the optimized systems in the detection of the realistic gamma spectra. The quantitative analysis was accomplished by comparing the signal to noise ratio between the different configurations and the ability to resolve the discrete reactions.

Results: We present the optimized dimensions for the primary CeBr₃ crystals with and without AC shielding. The specific values are given over a wide range of crystal volumes. The results show an optimal primary CeBr₃ crystal with an approximately diameter to length ratio of 1 without AC shielding and 0.5 with AC shielding. The secondary BGO and CeBr₃ should have a transverse dimension of 3 cm and 4.56 cm, respectively. The analysis of the prompt gamma spectra from ⁴He beams highlighted the presence of specific discrete reactions not observed in ¹H studies, e.g. ¹²C transition 0⁺ (7.65 MeV) → 2⁺ (4.44 MeV). This reaction is responsible for the generation of the 3.21 MeV prompt gamma peak. The optimized primary crystal provides a significant increase of the signal to noise ratio together with an improved resolution of the discrete gamma lines, especially in the high energy region. The detection configuration with an optimized anti-coincidence crystal improved the signal to noise ratio up to a factor of 3.5.

Conclusions: This work provides the optimal geometry for primary and secondary crystals to be used in range verification through PGS. The simulations show that such PGS system may allow for the simultaneous detection of the discrete lines from a thin metal implant within a water phantom.

Introduction

Charged particle therapy (CPT) takes advantage of the favorable depth-dose distribution of light ions in comparison to conventional radiotherapy. Among other ion species, ^4He beams present several preferred features: increased biological effectiveness and reduced scattering when compared to ^1H beams; and reduced fragmentation if compared to ^{12}C beams (Tommasino et al., 2015). The finite range of the primary particles potentially allows the sparing of healthy tissue distal to the target. However, the presence of range uncertainties requires the employment of margins during the treatment planning in order to guarantee the coverage of the whole tumor (Paganetti, 2012). On-line range verification techniques offer an opportunity to increase the confidence during the dose delivery by achieving more conformal CPT, thus exploiting its full potential.

In the recent years, several techniques have been proposed for *in vivo* range verification (Knopf et al., 2013). Prompt gamma imaging (PGI) is promising in offering range monitoring during treatment due to the instantaneous ($\sim fs \div ps$) emission of the secondary radiation. Therefore, it has a higher potential if applied to pencil beams scanning (PBS) than other monitoring techniques that suffer from biological washout and motion effects, such as Positron Emission Tomography (PET) (Moteabbed et al., 2011). On the other hand, the employment of PGI for range control relies on the development of dedicated detector systems due to the high energy and count rate of the emitted radiation.

Prompt gamma are one of the products of the nuclear interactions of the ion beam with the tissue. In such collisions, the projectile undergoes an inelastic interaction involving energy transfer with a target nucleus. Excited states of the projectile and the target nuclei are produced. The latter is mostly relevant in case of helium beams: the ^4He first excited nuclear level is 0^+ (20.21 MeV)¹ and leads to the emission of a proton without gamma quanta in coincidence. Analogous considerations apply to higher nuclear levels with the emission of other light fragments (Tilley et al., 1992). The excited target nucleus de-excites in a $fs \div ps$ time scale with the emission of fragments and an eventual final relaxation to the ground nuclear state through the emission of gamma rays. These are referred to as prompt gamma and are emitted with a complex energy spectrum essentially up to $E_\gamma = 10$ MeV. Such spectrum presents a continuous and a discrete component with a strong dependence on the target elemental composition and on the collision energy. Therefore, a PGI system should be optimized to detect high energy and high intensity gamma rays exclusively during the beam delivery.

Several detector concepts have been proposed for PGI, which have been recently reviewed by Krimmer et al., 2018. These can be classified in collimated and non-collimated systems. The former ones have been proven to be suitable for retrieving the range information from the beams of protons (Min et al., 2006) and carbon ions (Testa et al., 2008). Such systems aim to detect the gamma radiation emitted orthogonally to the beam direction with a certain

¹Notation for nuclear levels: $J^P(E_i)$, with E_i energy above the ground state.

angular acceptance. This geometry presents a direct correlation of the signal with the longitudinal position of the gamma production, since no strong dependencies on the detection angle are expected (Testa et al., 2009).

The background contribution from neutrons and secondary gamma can be reduced with the application of time-of-flight (TOF) windows based on the arrival time of the primary particles (Biegun et al., 2012). A more effective approach to exploit the discrete nature of the gamma spectrum consists of resolving the detection both in energy and time (Verburg et al., 2014). The single reaction channels may be resolved, which allows not only to reduce the background contribution, but also to analyze the relative intensity of the reactions and infer the beam energy independently at each collimation point (Verburg et al., 2012). This technique, also known as range control through prompt gamma spectroscopy (PGS), relies on the extraction of additional information from the spectrum through few detection points associated with large crystals. The latter, despite the collimated design, may improve the statistical limitations observed in the multi-slit cameras, which require the use of multiple thin crystals with a reduced single crystal detection efficiency (Min et al., 2012).

The key feature of PGS is the detection of the discrete prompt gamma peaks over a wide energy spectrum. The cerium bromide (CeBr_3) crystals feature the good energy and time resolution required for PGS (Quarati et al., 2013). Moreover, due to their low intrinsic activity, one can detect low energy prompt gamma lines, which may be relevant in the presence of metal implants (Magalhaes Martins et al., 2017).

With this work, we aim at optimizing the photo-peak efficiency and the suppression of non-photo-peak events with an appropriate design of primary and secondary crystals. We present a Monte Carlo (MC) optimization study for a detection system for range control through PGS. This system consists of a primary CeBr_3 crystal associated with secondary crystals for noise reduction. We tested the performances of the optimized design for the detection of the prompt gamma spectrum from ^4He nuclear interactions. Finally, we evaluated the signal-to-noise improvement in the detection of the discrete peaks in the presence of both homogeneous targets and metal inserts.

Materials and Methods

The optimization of the detector system was performed in sequential steps based on independent MC calculations. The focus of the study was the optimization of the detector geometry, based on electromagnetic radiation transport simulations. We chose an inelastic nuclear interaction model for ^4He that generated a realistic gamma spectrum. Two separate MC codes were adopted for the electromagnetic and nuclear simulations: FLUKA and Geant4. The study was based on three steps: optimization of the detector geometry for mono-energetic gamma radiation; generation of prompt gamma radiation

phase space (PS) ² from ^4He nuclear interactions; and evaluation of their detection performances.

Monte Carlo software and models

The geometry optimization of the detector system and its performance evaluation was entirely based on electromagnetic radiation transport simulations. As described in detail in 4.2, a mono-energetic gamma radiation was considered followed by nuclear MC simulations. Those generated the more complex and realistic gamma spectrum, but did not affect directly the optimization of the system. Consequently, those two steps can be treated as independent and do not require a unique MC code. Despite the high level of accuracy that can be achieved with both MC codes in the electromagnetic and nuclear simulations, we adopted separate codes in different steps of the study to achieve a good trade-off for our needs. FLUKA was adopted when a systematic variation of geometrical parameters was required. This choice was relied on its capability of varying geometrical parameters within multiple simulations. Geant4 was adopted for nuclear simulations in a fixed geometry. This choice was driven by its flexibility in selecting the nuclear interaction model and its parameters. The details of the single codes are presented below.

FLUKA

FLUKA is a general purpose MC simulation package with multiple applications in several fields (Böhlen et al., 2014, Ferrari et al., 2005). We adopted the FLUKA simulation package (version 2011-2c.5) to perform electromagnetic radiation transport simulations (the hadronic interactions were not considered). Extensive benchmarks have been performed on the electromagnetic component of this simulation package resulting in a higher accuracy over a wide energy spectrum from 1 PeV down to 1 keV (Battistoni et al., 2015). The simulations were performed with the precision defaults (PRECISION). This ensured the treatment of the Compton scattering with the introduction of the inelastic form factor corrections and a detailed photoelectric edge treatment. The particle transport threshold was set at 100 keV. The scoring of the quantities was performed with an user customization of the `mgdraw.f` routine, which tracks the event by event energy deposition in the relevant regions. We included as well the point-like energy deposition events (variable `RULL`) along with the continuous energy deposition (variable array `DTRACK`). We benchmarked the personalized `mgdraw.f` routine against the FLUKA built-in scoring card `DETECT` in a simulation with one CeBr_3 scoring region. For the following simulations we required full flexibility in presence of multiple scoring regions and energy binning. Therefore we choose the personalized `mgdraw.f` routine. When required, the external PS of the prompt gamma

²The phase space consists of a ROOT file with the information on the position, momentum, energy and time of the particles leaving the target.

events was imported with an additional user customization of the `source.f` routine.

Geant4 10.03

We adopted the Geant4 toolkit (version 10.03) to simulate the production of prompt gamma radiation through inelastic nuclear interactions (Agostinelli et al., 2003). The electromagnetic component was treated with the package `G4EmStandardPhysics_option3` and the particle transport threshold was set at 1 mm. The relevant hadronic inelastic models for ^4He in the therapeutic energy range are the binary light ion cascade (BICLI), the Liege intranuclear cascade (INCL) and the quantum molecular dynamics (QMD). The nuclear de-excitation model `G4PhotonEvaporation` handles the production of the continuum and discrete prompt gamma spectrum through the E1, M1 and E2 transitions. This determines the quality of the discrete spectrum, which database is based on the Evaluated Nuclear Structure Data File (ENSDF) (Allison et al., 2016). The aim of this work was not the benchmark or optimization of the models, but rather the generation of a realistic phase space to test the detector performances. Despite its highest computing burden, we adopted the comprehensive QMD model, which allows tuning just few free parameters that best reproduce the experimental data as already discussed by Pinto et al., 2016 (for proton beams) and by Dedes et al., 2014 (for carbon beams). Those studies also showed how the optimization affects mainly the total yield and not the spatial and energy distribution. The generated PS files from the simulations were converted into a compatible input format through dedicated ROOT routines (Brun et al., 1997).

Monte Carlo calculations

Detector geometry optimization.

We optimized the geometry of a detector system based on a primary CeBr_3 crystal surrounded by secondary crystals for noise rejection in anti coincidence (AC). We simulated bismuth germanate (BGO) and CeBr_3 as secondary crystals and compared to the configuration without an AC shielding. Despite the sub-optimal choice of CeBr_3 as secondary crystal, we tested this setup to investigate the volume requirements of secondary crystals with high energy resolution. This could allow for a more sophisticated system where the CeBr_3 crystals could be used both as primary crystals and for AC rejection. In the current work we limited our investigations to the geometry of the crystals and left aside the simulation of a complex collimation system. The schematic geometry of the three configurations is depicted in Fig. 4.9.

We simulated mono-energetic gamma beams with an $E_\gamma^i \in (0.5, 7.0)$ MeV in steps of $\Delta E_\gamma^{ij} = 0.5$ MeV impinging parallel to the main axis of the primary crystal. An ideal rectangular collimation with a slit $\Delta x = 1.0$ cm was considered and kept constant throughout the simulations. For every geometry and every E_γ^i , we set the number of simulated primary gamma events (N_0) at 10^6 . The following parameters were calculated:

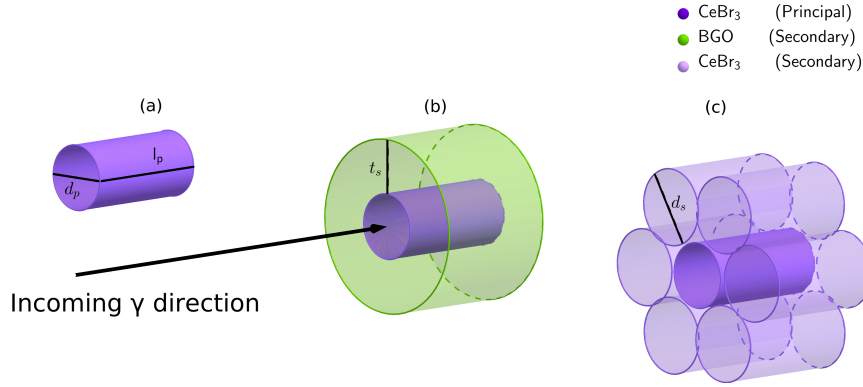


FIGURE 4.9: Schematic geometries of the detector system: primary CeBr_3 without an AC shielding (left); primary CeBr_3 with a BGO AC shielding (middle); primary CeBr_3 with a CeBr_3 AC shielding (right).

- number of photo peak events (N_{PP});
- number of single escape peak events (N_{SE});
- number of double escape peak events (N_{DE});
- number of Compton continuum events (N_{CC}).

The full description of the encapsulation geometry for the CeBr_3 detectors was taken into account, since such CeBr_3 crystals are highly hygroscopic (Quarati et al., 2013). Such description provides an accurate simulation of the radiation leaving from the primary to the secondary crystal. The front and lateral faces were surrounded by Teflon, air and aluminum. Independently of the crystal volume, the layer thicknesses for the front and lateral face were respectively: 0.5 mm (Teflon), 2.45 and 2.25 mm (air), and 0.8 mm and 1.25 mm (aluminum). The crystal back face was in contact with a 1.25 mm quartz window.

The secondary crystals were simulated as bare crystals. This simplified description provides a good approximation regarding the volume of the secondary crystal required to detect the radiation leaving the primary one. A BGO hollow cylinder was in contact with the external aluminum layer of the primary crystal and covered its whole length after encapsulation. Concerning the secondary CeBr_3 crystals, we considered that same length and placed them with a uniform azimuthal angular distribution. Such geometry required the introduction of a small gap between the aluminum and the secondary CeBr_3 . The more favorable geometry of secondary BGO in comparison to CeBr_3 results from the customizing constraints of such crystals and their availability.

Firstly, we varied the thickness of the secondary BGO (t_s) for a certain primary CeBr_3 diameter and length ($d_p = 1.5''$ and $l_p = 3''$). We then evaluated the rejection efficiency of N_{SE} , N_{DE} and N_{CC} . The optimized value t_s^{opt} was evaluated at a saturation of 95% and the optimized diameter of the

secondary CeBr₃ crystal (d_s^{opt}) was derived from the former (same attenuation power as for the optimized BGO). We set a threshold of 100 keV on the energy deposited by the gamma rays on the crystals.

Finally, we optimized the diameter to length ratio ($R_p = d_p/l_p$) of the primary CeBr₃ at varying volumes (V_p) of this crystal in the configuration with the secondary BGO. Different approaches were adopted for the setups with and without AC shielding (see Fig. 4.9). In the presence of AC shielding, N_{CC} is already minimized due to the presence of the secondary crystal, and therefore we varied R_p in order to maximize the ratio $\epsilon = N_{PP}/N_0$. If no AC shielding was employed, we simply chose the value that maximizes the ratio $\eta = N_{PP}/N_{CC}$.

⁴He prompt gamma phase space generation

The prompt gamma PS was generated by simulating the interaction of ⁴He mono-energetic pencil beams ($E_0^{kin} = 158.75$ MeV/n) with different targets. We simulated homogeneous cylindrical targets composed of water, aluminum and graphite. They were 40 cm long and had a diameter of 15 cm. Additionally, we simulated a water target with a thin aluminum insert ($\Delta z = 2$ mm) positioned at a depth $z = 10$ cm. We aimed at evaluating the simultaneous detection efficiency of both high energy gamma lines from ¹⁶O and low energy gamma lines from a thin metal implant. Despite its less frequent use compared to other implant metals such as titanium or gold, we simulated an aluminum target since the CeBr₃ capability to distinguish its spectral lines has been experimentally demonstrated (Magalhaes Martins et al., 2017).

The PS files were generated with 10^8 primary particles for each setup, then exported into a ROOT binary format and converted into a source input file for the FLUKA simulations. In the conversion, we followed the angular and longitudinal cuts similar to previous studies (Janssen et al., 2014). In the current study we applied: $\theta = 90^\circ \pm 1.5^\circ$ and $z = z_0 \pm 0.5$ cm. We considered z_0 values of 2 cm upstreaming the range of the primary ⁴He. For the simulation with the aluminum insert, z_0 was positioned at its center. We followed the approach of the shifting TOF window (Biegun et al., 2012) and applied a time cut $\Delta t = 1$ ns.

⁴He prompt gamma phase space detection

The performances of the optimized detector geometry were tested by detecting the prompt gamma PS. We assumed the optimized R_p values (R_p^{opt}) for the setups with and without AC shielding and set the volume for the primary crystal $V_p = 86.87$ cm³ ($d_p = 1.5''$ and $l_p = 3''$). The geometry of the secondary crystals was set according with the previously calculated t_s^{opt} and d_s^{opt} . The number of simulated primaries was 10^8 for each setup.

Extraction of parameters

The simulated energy deposition in the primary CeBr_3 was converted into the detected spectrum by introducing the crystal energy resolution experimentally determined by Roemer et al., 2015. This ensured a more realistic energy resolution if compared to the Poisson distribution description, i.e. $R(E) \propto E^{-0.5}$.

The signal-to-noise ratio (SNR) values for the discrete peaks were evaluated through a background subtraction and peak fit routine. The continuous background distribution $BG(E)$ was computed with the dedicated ROOT function (Morháč et al., 2000) from the TSpectrum class. This included the continuous component of the PS and the Compton continuum associated with the detection. We then obtained the background-subtracted signal for each peak $S_i(E)$ and, through a Gaussian fit, we calculated the peak energy, E_i , and standard deviation, σ_i . The SNR is then given by

$$SNR_i = \frac{\int_E S_i(\tilde{E}) d\tilde{E}}{\int_{E_i-3\sigma_i}^{E_i+3\sigma_i} BG(\tilde{E}) d\tilde{E}}. \quad (4.1)$$

We also calculated the relative SNR between the setups shown in Fig. 4.9. Moreover, we compared the SNR gain obtained with the optimized values R_p^{opt} to the ones commercially available (0.5 and 1).

Results and Discussion

Detector geometry optimization

Secondary crystal: BGO

The evolution of the Compton suppression and the single escape peak suppression for an increasing thickness of the secondary BGO crystal is depicted in Fig. 4.10. It shows a fast decrease of N_{CC} , N_{SE} and N_{DE} relative to N_{PP} before reaching saturation. The trend of the double escape suppression is similar to the SE one (not shown). While, the suppression of the escape peaks follows the detection of isotropic 511 keV photons, the Compton suppression involves a more complex distribution both in angle and in energy. Nevertheless, we reach the 95% saturation at similar t_s^{opt} values for both types of suppression and no significant dependence on the energy of the incoming gamma was observed (see Fig. 4.11). Also in presence of a complex spectrum, this allows extracting an energy independent t_s^{opt} for each type of suppression, which results in

$$t_s^{opt}(CC) = (2.94 \pm 0.02) \text{ cm} \quad (4.2)$$

$$t_s^{opt}(SE) = (3.16 \pm 0.03) \text{ cm} \quad (4.3)$$

$$t_s^{opt}(DE) = (2.13 \pm 0.03) \text{ cm} \quad (4.4)$$

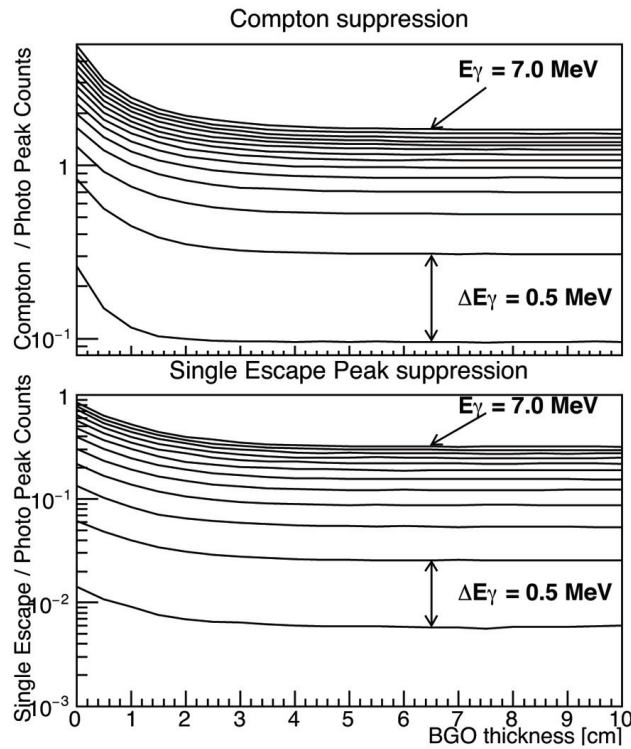


FIGURE 4.10: Evolution of the Compton suppression N_{CC}/N_{PP} (top) and the single escape peak suppression N_{SE}/N_{PP} (bottom) for an increasing thickness t_s of the secondary BGO. Each solid line represents the result for mono-energetic gamma beams separated by steps of $\Delta E_\gamma = 0.5$ MeV. The energy ranges are respectively $E_\gamma^i \in (0.5, 7.0)$ MeV (top) and $E_\gamma^i \in (1.5, 7.0)$ MeV (bottom).

Therefore, we decided to set the thickness of the secondary BGO (t_s) at 3.0 cm. This choice led to a reduction of the Compton continuum component and single escape peaks, respectively, by a factor 2.63 and 2.44 for 6.0 MeV incoming gamma rays.

Secondary crystal: CeBr₃

The optimization of the CeBr₃ was based on the results obtained with BGO. The diameter d_s^{opt} of the CeBr₃ crystal needed to achieve a detection probability equivalent to the one obtained with the BGO crystal with $t_s^{opt} = 3.0$ cm was (4.56 ± 0.02) cm. This value was not optimized separately between Compton continuum and escape peaks, since we only considered the attenuation for both crystals.

Primary crystal: CeBr₃ diameter to length ratio

Fig. 4.12 shows the optimization curve for the primary CeBr₃ crystal with and without the AC shielding, with distinct trends regarding the R_p . For an increasing volume up to a maximum crystal size of 3'' × 3'', R_p increases in the

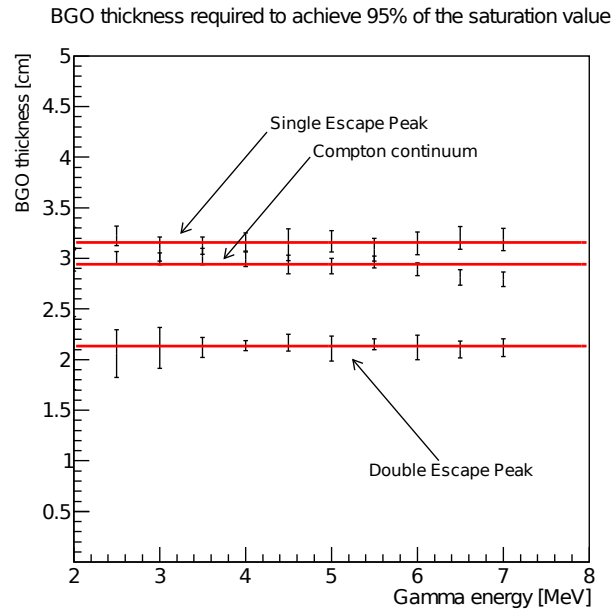


FIGURE 4.11: Extrapolated t_s^{opt} values at different mono-energetic gamma radiation energies for the Compton continuum, and single and double escape peaks.

presence of AC shielding and decreases if no AC shielding is employed. The optimization without AC shielding suggests the use of crystals with R_p close to 1. Taking into account the crystal volume chosen for the SNR evaluation, we obtained an optimal value $R_p^{noAC}(V_p = 86.87 \text{ cm}^3) = 0.897 \pm 0.002 \text{ cm}$. The optimization with the AC shielding suggests the use of crystals with R_p close to 0.5. We achieved an optimal value $R_p^{AC}(V_p = 86.87 \text{ cm}^3) = 0.396 \pm 0.003$. A steep increase of R_p was observed at small volumes.

^4He prompt gamma phase space generation

Fig. 4.13 shows the prompt gamma yield resulting from the irradiation of a water target with an aluminum insert. The presence of the aluminum insert leads to an increased gamma production and energy deposition at its location. However, the dose deposition is smaller than the one in water due to the higher density of the metal.

Fig. 4.14 shows the energy spectrum of the emitted prompt gamma radiation. An energy cut on such spectrum at 10 MeV was applied, thus ensuring that more than 99% of the total gamma radiation was processed.

^4He prompt gamma phase space detection

The rate of events with activation of the secondary crystal depends on the analyzed spectrum. We observed variations up to $\pm 3\%$. For the most complex case of the water target with the aluminum insert, 26.75% and 21.79% of

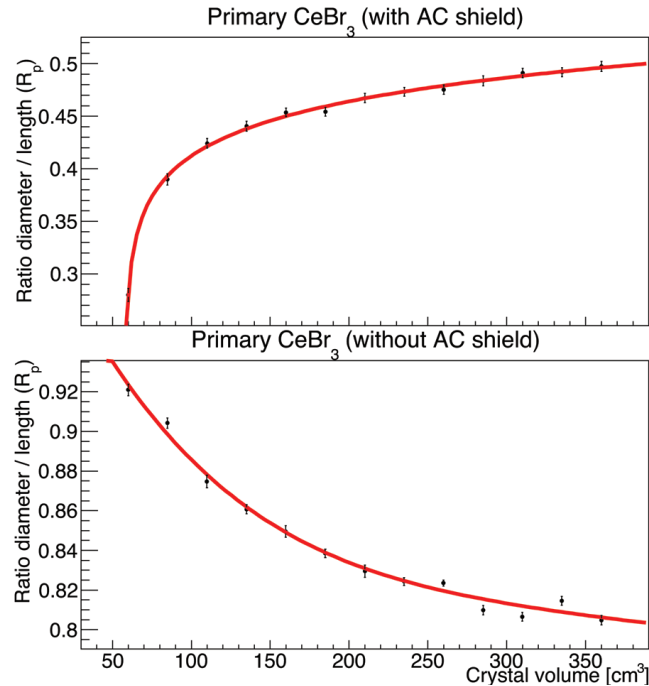


FIGURE 4.12: Curves of the diameter to length ratio of the primary CeBr_3 for an increasing crystal volume. The system without AC shielding was optimized based on the maximization of $\eta = N_{\text{PP}}/N_{\text{CC}}$ (top). The system with an active AC shielding was optimized based on the maximization of $\epsilon = N_{\text{PP}}/N_0$ (bottom).

the primary crystal events activated the BGO and CeBr_3 AC shieldings, respectively. The activation of the BGO shielding following the detection by a non-optimized primary CeBr_3 crystal with $R_p = 1$ and $R_p = 0.5$ was 12.53% and 22.94%, respectively.

The complete set of PS spectra detected by the optimized systems for a constant $V_p = 86.87 \text{ cm}^3$ are depicted in Fig. 4.15. The spectra are shown in logarithmic scale with an energy window from 0.511 MeV up to 7 MeV. No algorithmic background reduction was applied. The presence of the AC shielding resulted in a significant reduction of the Compton continuum background, especially in the high energy region. A higher suppression was obtained with the BGO shielding.

The detection in AC improves the SNR and clearly resolves the peaks, especially the ones closer to the most intense energy lines, e.g., the energy peaks of 5.2 MeV and 3.21 MeV for the water and graphite targets, respectively. The latter results from the ^{12}C transition $0^+ (7.65 \text{ MeV}) \rightarrow 2^+ (4.44 \text{ MeV})$ followed by the relaxation to the ground state.

The quantitative evaluation of the detection performances was performed with a SNR evaluation. Table 4.4 reports the list of the relative SNR for the most important discrete peaks.

The relative values refer to the ratio between the SNR for the optimized systems with AC shielding to the SNR for the optimized system without AC shielding. As observed in the spectra, the highest improvement is obtained

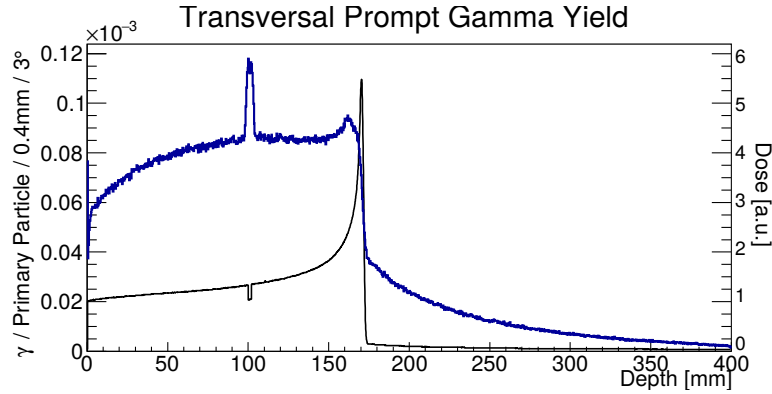


FIGURE 4.13: Phase space production for the water target with a 2 mm aluminum insert. The prompt gamma yield at $\theta = 90^\circ \pm 1.5^\circ$ is shown (blue). A wide TOF window of 10 ns was implemented to acquire the gamma rays through all the phantom length. The dose deposition is also shown normalized to the entrance value (black).

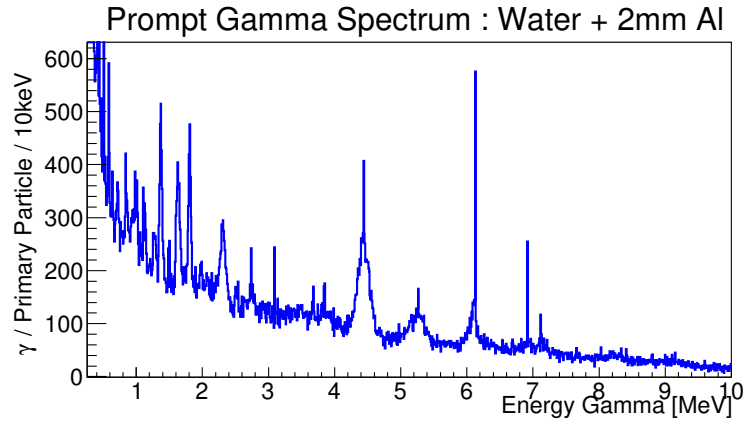


FIGURE 4.14: Energy spectrum of the phase space for the water target with a 2 mm aluminum insert. The following cuts were introduced: $\theta = (90 \pm 1.5)^\circ$, $z = (10.1 \pm 0.5)$ cm and $\Delta t = 1$ ns.

in the high energy region. For the most complex scenario of the water target with the aluminum insert, the detection with the BGO AC shield grants in average an improvement of the SNR by a factor ~ 2 . Slightly smaller values are obtained with secondary CeBr_3 scintillators. Highly relevant is also the detection performances for the low energy peaks. The lowest energy peak considered was the result of the ^{10}B transition 1^+ (0.718 MeV) \rightarrow 3^+ (0.0 MeV). The ^{10}B is produced by spallation reactions of ^4He both on ^{12}C and ^{16}O (Vidal-Quadras et al., 1979). Moreover, we observed an increase in the production of the ^{10}B state 1^+ (0.718 MeV) (water target) and the 1^+ (2.15 MeV) state (graphite target), resulting in two different lines in the energy spectra.

Finally, the SNR comparison between the system with optimized R_p and the commercially available systems ($R_p = 1$ and $R_p = 0.5$) showed the advantage of the dedicated geometry. For comparison, we considered the

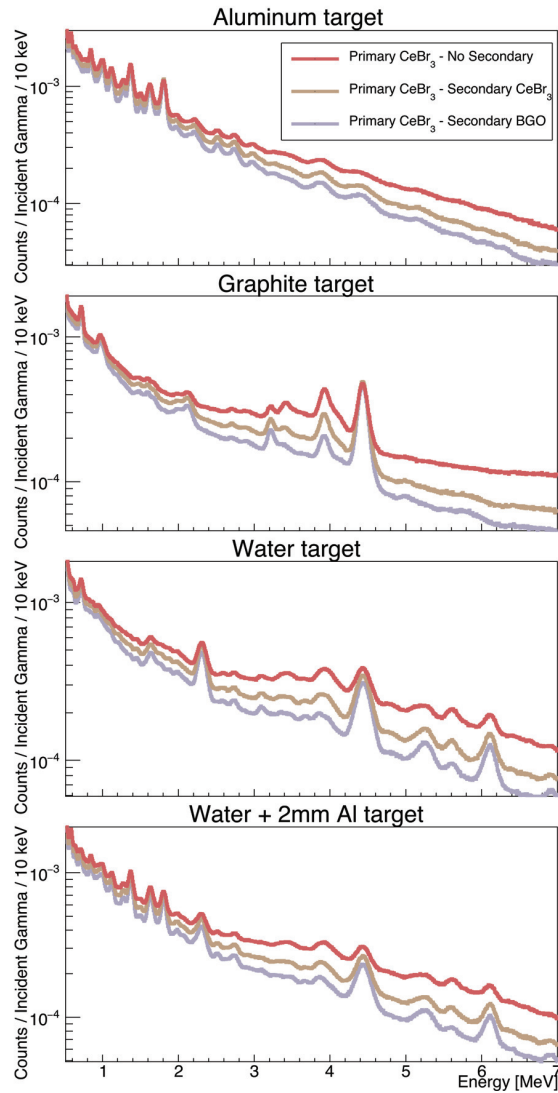


FIGURE 4.15: Energy spectra of the detected prompt gamma radiation for the 3 optimized setups. From top to bottom: aluminum target, graphite target, water target and water target with aluminum insert.

$E = 4.4$ MeV peak for the water target with the aluminum insert. For the configuration without AC shielding, the use of a crystal with $R_p = 1$ and $R_p = 0.5$ decreased the SNR by 0.98 and 0.88, respectively, which compares to the optimized $R_p = 0.897$. For a configuration with a BGO AC shielding, the use of a crystal with $R_p = 0.5$ and $R_p = 1$ decreased the SNR by 0.94 and 0.70, respectively, which compares to the optimized $R_p = 0.396$.

Source	E_γ [MeV]	Graphite	Aluminum	Water	Water + Al
		$\hat{\text{SNR}}_{BGO}$ $\hat{\text{SNR}}_{CeBr_3}$	$\hat{\text{SNR}}_{BGO}$ $\hat{\text{SNR}}_{CeBr_3}$	$\hat{\text{SNR}}_{BGO}$ $\hat{\text{SNR}}_{CeBr_3}$	$\hat{\text{SNR}}_{BGO}$ $\hat{\text{SNR}}_{CeBr_3}$
^{16}O	6.13	-	-	2.70 2.04	3.26 2.08
$^{14}\text{N}, ^{15}\text{N}, ^{15}\text{O}$	5.2	-	-	2.47 1.84	2.36 1.72
$^{11}\text{B}, ^{12}\text{C}$	4.4	2.09 1.73	-	2.48 1.94	2.38 1.87
^{27}Al	3.88	-	1.61 1.33	-	1.32 1.15
^{13}C	3.68	-	-	1.22 1.34	-
^{12}C	3.21	3.52 2.77	-	-	-
^{16}O	2.74	-	-	1.76 1.22	1.93 1.55
$^{14}\text{N}, ^{27}\text{Al}, ^{30}\text{Si}$	2.3	-	1.58 1.43	1.71 1.46	1.74 1.48
^{10}B	2.15	1.50 1.53	-	-	-
^{26}Mg	1.81	-	1.52 1.37	-	1.60 1.41
$^{14}\text{N}, ^{20}\text{Ne}$	1.6	-	1.56 1.36	2.40 2.01	1.58 1.43
^{24}Mg	1.37	-	1.52 1.35	-	1.53 1.26
^{18}F	0.937	1.32 1.21	-	1.86 1.85	1.30 1.19
^{27}Al	0.843	-	1.39 1.27	-	2.27 2.18
^{10}B	0.718	1.31 1.28	-	2.24 1.23	1.48 1.33

TABLE 4.2: Relative signal-to-noise values. The $\hat{\text{SNR}}_i$ are given for the optimized systems with BGO and CeBr_3 AC shield with respect to the optimized configuration without AC shield. The first entry indicates the nuclear species originating the discrete peak. Discrete peaks with $\Delta E < 0.1$ MeV and $E > 1$ MeV are aggregated. The values in brackets represent the uncertainty on the last $\hat{\text{SNR}}_i$ digit.

Discussion

The optimization without the AC shielding suggested the use of crystals with R_p close to 1. This is explained by the fact that the lack of a secondary crystal for Compton rejection requires a large diameter in order to stop the Compton scattered events within the primary CeBr_3 and obtain a photo-peak event, thus increasing $\eta = N_{PP}/N_{CC}$. On the other hand, the results show that higher values of R_p led to sub-optimal crystals. The resulting smaller values of η at larger R_p cannot be interpreted with a larger N_{CC} , but rather due to a smaller N_{PP} and therefore a lower photo-peak efficiency given by the reduced l_p .

The optimization with the AC shielding suggested the use of crystals with R_p close to 0.5. In this case, the Compton scattered events were rejected by the secondary crystal and the priority in the optimization was given to the photo-peak events. This led to higher l_p values to increase the interaction probability of the gamma rays. However, we observed that too small values of R_p resulted into a reduction of $\epsilon = N_{PP}/N_0$, which could be interpreted with a lateral loss of scattered radiation due to the reduced d_p .

A steep increase of R_p was observed at small volumes. This is correlated to the quadratic dependence $V_p \propto d_p^2$ and to the fact that at small volumes the dominant parameter is l_p .

The cuts applied to the gamma radiation, i.e. $\theta = 90^\circ \pm 1.5^\circ$ and $z = z_0 \pm 0.5$ cm, were compatible with a potential experiment having a 7.5 cm thick slit collimation placed at 10 cm from the target with an additional 5 cm gap before the detector. The application of PS cuts instead of simulating a slit collimator served to focus the analysis on the scintillators optimization. The introduction of a collimator would result in an increase of the background continuum component of the gamma radiation impinging on the CeBr_3 , mainly due to events scattered in the collimator. This applies especially for the low energy component of the spectrum. However, the contribution of the scattered component of the gamma radiation reaching the CeBr_3 can be reduced with the application of a narrow TOF window about the prompt component. The discrimination is possible due to the fact that the latter presents a well defined time structure, while the former has a broader time distribution (Lopes et al., 2012). The collimation about the metal implant provided an excellent scenario to test the detection performance of simultaneous high and low energy discrete lines.

The difference in the activation of the AC shield had to be attributed to the geometrical differences of the secondary crystals depicted in Fig. 4.9. The smaller values are related to the fact that a larger d_p decreases the probability for a scattered event to leave the primary and reach the secondary crystal.

The intense production of the ^{12}C excited state 0^+ (7.65 MeV) was not observed in previous simulation studies with proton beam (Verburg et al., 2012). It is therefore highly relevant the presence of the optimized AC shielding to detect the new discrete lines specific to ^4He beams.

When compared with the typical size of commercially available crystals ($d = 2''$ or $3''$), we may conclude that the secondary CeBr_3 crystal should be as

large as the primary one. Together with the constraints in shape presented by such crystals and low relevance of a good energy resolution on the secondary crystal, we suggest the choice of BGO as secondary crystal.

The study aimed at a quantitative assessment of the capability of the optimized system to resolve the discrete prompt gamma lines induced by ^4He beams (summarized in Table 4.4). The geometrical optimization of the system has been performed independently of the ^4He induced prompt gamma spectrum. In spite of the differences in the prompt gamma emission that have led to different specific SNR_i values, we believe that such optimized system may therefore be applied to other beam species.

Conclusions

We presented an optimized detector design with CeBr_3 crystals to be used for range verification through prompt gamma spectroscopy. The study was focused on ^4He beams with applicability also to other beam species. The introduction of a Compton shielding in anti-coincidence increased the signal-to-noise ratio for discrete gamma peaks up to a factor of 3.5. We concluded that the primary CeBr_3 crystal should have a diameter to length ratio of 0.5 and the BGO should be used as a secondary crystal. This configuration allowed for the simultaneous detection of the discrete energy lines from a water target with a thin metal insert.

Acknowledgments

Author R.D.B. is supported by the International Max Planck Research School for Quantum Dynamics in Physics, Chemistry and Biology, Heidelberg, Germany. P.M.M. is supported by a research fellowship for postdoctoral researchers from the Alexander von Humboldt Foundation, Bonn, Germany.

The authors would like to thank the research group in-vivo dosimetry for new types of radiation at OncoRay, Dresden, Germany, in particular Dr. Guntram Pausch for fruitful discussions.

4.3 Experimental verification of the spectroscopic unit performances

Title : Results from the experimental evaluation of CeBr₃ scintillators for ⁴He prompt gamma spectroscopy

Authors : Riccardo Dal Bello, Paulo Magalhaes Martins, Joao Graça, German Hermann, Thomas Kihm and Joao Seco

Status : Published

Journal : Medical Physics, 46(8), pp. 3615-3626, 2019

DOI : 10.1002/mp.13594

Copyright : © 2019 American Association of Physicists in Medicine. Reproduced with permission. Permission request number: 4667071434831. All rights reserved.

Contributions : R.D.B. designed and performed the experiments. The last author, J.S., coordinated the project and provided guidance during the experimental planning. The third to fifth authors, J.C., G.H. and T.K., provided support with the electronics used in the experimental setup. This included customized pre-amplifiers and a FADC module. R.D.B. conducted the post-processing of the experimental data and he wrote the software to perform the quantitative analysis. The second author, P.M.M., attended and provided support during the experimental campaigns and he contributed to the interpretation of the results. R.D.B. finalized the data analysis, wrote the software to export the plots included in the article and wrote the article. R.D.B. and the co-authors concluded the studying reporting quantitative parameters that demonstrate the improvement of the experimentally detected spectra obtained adopting the previously optimized detection system.

Abstract

Purpose: The presence of range uncertainties hinders the exploitation of the full potential of charged particle therapy. Several range verification techniques have been proposed to mitigate this limitation. Prompt gamma spectroscopy (PGS) is among the most promising solutions for online and in vivo range verification. In this work we present the experimental results of the detection of prompt gamma radiation, induced by ^4He beams at the Heidelberg Ion-Beam Therapy Center (HIT). The results were obtained, using a spectroscopic unit of which the design has been optimized using Monte Carlo simulations.

Methods: The spectroscopic unit is composed by a primary cerium bromide (CeBr_3) crystal surrounded by a secondary bismuth germanate (BGO) crystal for anti-coincidence detection (AC). The digitalization of the signals is performed with an advanced FADC/FPGA system. ^4He beams at clinical energies and intensities are delivered to multiple targets in the experimental cave at the HIT. We analyze the production of prompt gamma on oxygen and carbon targets, as well as high Z materials such as titanium and aluminum. The quantitative analysis includes a systematic comparison of the signal-to-noise ratio (SNR) improvement for the spectral lines when introducing the AC detection. Moreover, the SNR improvement could provide a reduction of the number of events required to draw robust conclusions. We perform a statistic analysis to determine the magnitude of such an effect.

Results: We present the energy spectra detected by the primary CeBr_3 and the secondary BGO. The combination of these two detectors leads to an average increase of the signal-to-noise ratio by a factor 2.1, which confirms the Monte Carlo predictions. The spectroscopic unit is capable of detecting efficiently the discrete gamma emission over the full energy spectrum. We identify and analyze nineteen independent spectral lines in an energy range spacing from $E_\gamma = 0.718 \text{ MeV}$ to $E_\gamma = 6.13 \text{ MeV}$. Moreover, when introducing the AC detection, the number of events required to determine robustly the intensity of the discrete lines decreases. Finally, the analysis of the low energy reaction lines determines whether a thin metal insert is introduced in the beam direction.

Conclusions: This work provides the experimental characterization of the spectroscopy unit in development for range verification through PGS at the HIT. Excellent performances have been demonstrated over the full prompt gamma energy spectrum with ^4He beams at clinical energies and intensities.

Introduction

The key feature exploited in charged particle therapy (CPT) is the finite range of swift ions in matter. Conversely to conventional radiotherapy, the ion beams deposit most of their energy at the so-called Bragg peak, i.e. at the maximum penetration depth. This potentially allows for the generation of highly conformal dose distributions, thus reducing the dose to healthy tissue (Amaldi et al., 2005). Beams of light nuclei are nowadays used in clinical

practice, such as ^1p and ^{12}C ions. However, there is a growing interest in other ions, such as ^4He and ^{16}O . The former is since long known for its dosimetric properties, while the latter benefits from the high linear energy transfer (Mein et al., 2018). The ^4He beams show distinct advantages against proton beams due to the sharper lateral and distal profile. Moreover, the rather complex biological effectiveness of ^{12}C beams could also ease the choice of clinical ^4He beams instead (Tommasino et al., 2015).

The presence of range uncertainties hinders the full advantage of CPT (Paganetti, 2012). Therefore, sub-optimal treatment angles are chosen and the physical uncertainties related to the beam interactions should be considered along with the clinical delineation uncertainties. In order to avoid these compromises, several techniques for *in-vivo* range monitoring have since long been proposed and investigated (Knopf et al., 2013).

Prompt gamma imaging (PGI) has emerged as a promising technique for *in-vivo* range monitoring and online beam tracking. This relies on the fact that the secondary radiation is promptly generated by the inelastic nuclear interactions between the beam and the human body and leaves the patient in sub-nanosecond time scales. Conversely to other techniques such as positron emission tomography (PET) and secondary charged particle trackers, PGI does not suffer from biological wash-out effects (Handrack et al., 2017) and the limitation in the spatial resolution from intrinsic multiple Coulomb scattering in the patient (Mattei et al., 2017). On the other hand, the development of PGI requires dedicated technology capable of detecting high-energetic gamma radiation at high count rates exclusively during the beam delivery. In this work, we focus primarily on the detection of such radiation at beam intensities available in a clinical synchrotron-based facility.

Numerous solutions have been proposed for PGI (Krimmer et al., 2018). Among the proposed techniques, different groups have developed systems based on multi-slits (Pinto et al., 2014), knife-edge-shaped slits (Bom et al., 2012), Compton cameras (Draeger et al., 2018), timing without collimation (Golnik et al., 2014) or integrating systems (Krimmer et al., 2017). Several successful experiments with collimated designs showed a good correlation between the proton (Min et al., 2006) and the carbon (Testa et al., 2008) ion range with the prompt gamma emission profile at 90° from the beam axis. So far, the investigation with other beam species focused only on the total cross section for the production of secondary radiation in non-collimated experiments (Mattei et al., 2017). In general, when moving from proton to helium beams there are two counterbalancing phenomena affecting the prompt gamma statistics. The number of primary particles necessary to deliver a given dose reduces (Tommasino et al., 2015) but at the same time the cross-section for production of prompt gamma radiation increases (Kozlovsky et al., 2002). Moreover, proton and helium induced prompt gamma present similar energy dependence for the cross sections. Finally, the energy thresholds for the nuclear reactions leading to prompt gamma production are found at lower values for helium projectiles. This effect could provide an additional benefit as the prompt gamma production is favoured closer to the position where the primary particles come to rest.

There are currently two PGI systems based on collimated systems that have reached the clinical prototype for proton range verification. The first application in men was the knife-edge slit camera from IBA³ (Xie et al., 2017) (Richter et al., 2016). This device retrieves the relative changes in the total prompt gamma emission profile along the Bragg peak. The second prototype is a prompt-gamma spectroscope developed at the MGH⁴, that measures the absolute deviations with respect to the plan and it is foreseen for application in a upcoming clinical study (Hueso-González et al., 2018). It exploits another fundamental property of the prompt gamma radiation, i.e. their discrete spectral energy lines associated with specific nuclear transitions. One can correlate the intensity of the several spectral lines with the absolute range provided an accurate knowledge of the energy-dependent cross-sections (Verburg et al., 2014).

The critical components of a PGS prototype are its dedicated fast detectors. They must feature high energy resolution, the capability of resolving the prompt gamma spectrum up to 10 MeV and cope with the high clinical intensities. The Cerium(III) bromide (CeBr_3) scintillating crystals have shown promising results for such application, opening to the possibility to detect also the low energy component of the prompt gamma spectrum (Magalhaes Martins et al., 2017). This could be performed especially due to the very low intrinsic activity and the excellence performances for $E_\gamma < 3$ MeV (Quarati et al., 2013). This makes them suitable for the detection of the low energy lines generated by the irradiation of high-Z materials usually included in metal implants. The spectroscopic properties of such a prototype can be further improved by surrounding the primary crystals with an anti-coincidence shield, thus suppressing the Compton scattered events and the single- and double-escape peaks (Dal Bello et al., 2018). The optimization of the detector performances is critical for PGS application in a future clinical scenario. In particular, this technique is based on the possibility to detect independent spectral lines produced by different nuclear reactions. Increasing the energy range of the detectable spectrum and improving the background subtraction aims to raise the accuracy in the prediction of the ion range. Moreover, the capability to detect the low energy component of the spectrum could be relevant for patients having the target volume close to a metallic implant, which could significantly compromise the dose distribution (Dietlicher et al., 2014). In such a scenario, analyzing the prompt gamma spectrum can provide a feedback on whether the metallic structure was or was not located along the beam path during the treatment. In this paper, we investigate a spectroscopic unit combining the CeBr_3 crystal with a secondary crystal to be used in future applications of PGS for range control in CPT.

The aim of this work is the assessment of the experimental performance of this spectroscopic unit during the ^4He irradiation of several phantoms under clinically relevant beam energies and intensities. This work follows a dedicated Monte Carlo optimization of such a spectroscopic unit (Dal Bello et al., 2018). Here, we present the performances of its primary and secondary

³Ion Beam Applications SA, Louvain-la-Neuve, Belgium

⁴Massachusetts General Hospital, Boston, U.S.A.

detectors. We also show the experimental results from the irradiation of different targets, including two thin metal inserts.

Materials and Methods

The properties of a single spectroscopy unit from the PGS system currently being developed at the German Cancer Research Center⁵ was evaluated. The details of the experimental components are presented below.

Ion beam characteristics

The experimental work was performed at the Heidelberg Ion-Beam Therapy Center (HIT), Heidelberg, Germany (Haberer et al., 2004). The ^4He beams were delivered to the experimental cave through the therapeutic beam monitoring nozzle, which was used in the active feedback mode to guarantee the beam stability. The beam was controlled using the therapy control system (TCS)⁶. The nominal parameters of the beam were: $E_0^{\text{kin}} = 149.02 \text{ MeV/u}$, $I_2 = 3 \cdot 10^7 \text{ ions} \cdot \text{s}^{-1}$, $\text{FWHM}_{x,y} = 6.7 \text{ mm}$. The beam was delivered at the isocenter, i.e. no treatment plan was considered. We delivered approximately $9 \cdot 10^9$ primary particles during 10 minutes, where the current I_2 corresponded to the one during beam-on time that was 50% of the total time. We chose this high number of primary ^4He particles in order to perform a robust statistic analysis, which will be presented in the section "Relaxation of statistics requirements".

Detectors arrangement

The measurements were performed using the following detectors:

- Primary: CeBr_3 scintillating crystal with a cylindrical shape (diameter $d = 3.81 \text{ cm}$ and length $l = 7.62 \text{ cm}$)⁷. This hygroscopic detector was coupled to a Hamamatsu photomultiplier (PMT) R9420-100 and protected by layers of Teflon and aluminum.
- Secondary: Bismuth germanium oxide (BGO) scintillating crystal with a cylindrical shape and a hollow cylinder to fit the CeBr_3 (inner diameter $d_{\text{in}} = 4.6 \text{ cm}$, thickness $t = 3 \text{ cm}$ and length $l = 11 \text{ cm}$). The crystal was sectioned in eight optically-separated and azimuthally-symmetric segments. Each section was coupled to an independent Hamamatsu PMT R1924. This crystal is used as Anti-Compton (AC) shield.
- Trigger: EJ-200 scintillating plastic with a parallelepipedic shape (volume $V = 8 \times 8 \times 0.1 \text{ cm}^3$). It was sealed with aluminum foil and black tape to make it light tight and coupled on one side with a silicone coupling component to an Hamamatsu PMT R13089.

⁵DKFZ, Heidelberg, Germany

⁶Siemens Medical Solutions, Erlangen, Germany

⁷ Scionix Holland B.V., Bunnik, The Netherlands

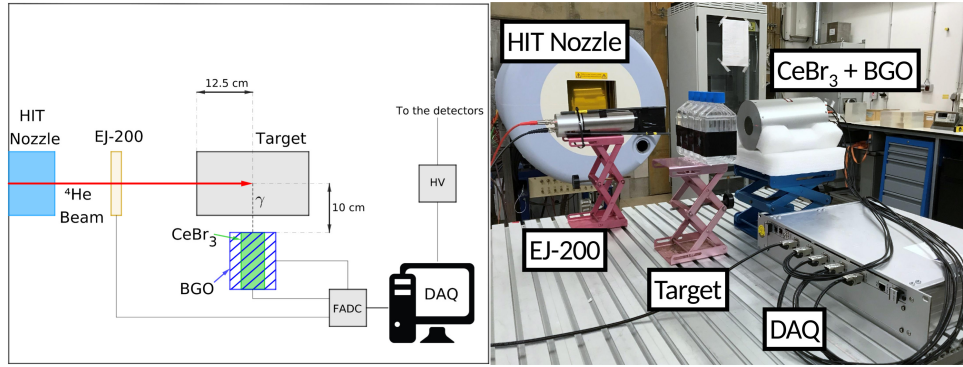


FIGURE 4.16: Detectors arrangement in a schematic representation (left) and in its realization in the experimental cave at HIT (right)

Figure 4.16 shows the prompt-gamma spectroscopy unit composed by the CeBr₃ detector inside the BGO detector with both front faces aligned. The choice of the dimension and shape of the detectors was taken based on a previous Monte Carlo study (Dal Bello et al., 2018). The EJ-200 detector was placed upstream to the target in order to provide the Time-of-Flight (ToF) information. Therefore, the EJ-200 is considered as the beam trigger. We placed the spectroscopy unit at an angle of 90° and 10 cm from the beam axis. In the longitudinal direction we placed the spectroscopic unit with the principal axis aligned to 12.5 cm downstream the front face of the targets, i.e. approximately at the center of the fourth flask for the water target and the center of the third block for the PMMA target. The experiments were performed without collimation in order to focus the data analysis on the spectroscopy unit.

Electronics setup

The data acquisition system (DAQ) was based on one FlashCam FADC module (Werner et al., 2017). The FlashCam FADC system, originally designed for the Cherenkov Telescope Array Actis et al., 2011, provides three fundamental properties for PGS: continuous high-speed digitization (12-bit, 250 MS/s FADC system) with on-board FPGA-based digital signal processing and triggering, multi-channel acquisition and flexible Ethernet-based interface (10 Gbit) with high data-rate capability for continuous data streaming.

We acquired event-by-event with single traces $\Delta t = 240$ ns and sampling intervals: $\delta t = 1$ ns for the EJ-200, $\delta t = 4$ ns for the CeBr₃ and the BGO. The slower sampling rates were chosen according to the slower response of the scintillators. In the case of the EJ-200, the $\delta t = 1$ ns is achieved, by splitting the signal on 4 FADC channels, which are operated with $\delta t = 1$ ns phase shift with respect to each other. In the case of the BGO, we summed the signals from four PMT and fed them into one FADC channel. This reduced the number of the FADC channels needed for the AC shield from eight to two, while keeping the pile-up in this detector below 1%. Moreover, the signals from each BGO PMTs were pre-amplified with independent non-inverting amplifiers in buffer mode having a load of $R = 225 \Omega$ and a first order band-pass

filter with the low cutoff frequency at $\nu_{\text{low}} = 1.5$ MHz and the high cutoff frequency at $\nu_{\text{high}} = 15$ MHz. This settings represented a tradeoff between energy and time resolution of the BGO.

The DAQ was triggered by events in the CeBr₃ with a threshold set at $E_{\gamma} = 511$ keV. We registered a maximum count rate of $5.5 \cdot 10^4$ cps and a dead time below 7%.

Data analysis

Detectors based background rejection

The off-line data analysis was performed with ROOT (Brun et al., 1997). In the post-processing we considered only the CeBr₃ events with a coinciding signal in the EJ-200 and in anti-coincidence with the BGO. The last condition did not apply when analyzing the CeBr₃ only.

The ToF distributions between the EJ-200 and the CeBr₃ slightly depended on the target. We defined σ_{target} as the standard deviation of the Gaussian component of the respective ToF distributions for each of the four targets, which always respected $\sigma_{\text{target}} < 2$ ns. The coincidence windows were set at $\pm 1.5 \cdot \sigma_{\text{target}}$. This choice was made to maximize the prompt gamma contribution in the ToF window and minimize the one of photons that have scattered or were produced by neutrons in the walls of the experimental cave. Previous studies have shown that these two components are separated by time intervals $\Delta t \geq 8$ ns (Testa et al., 2010), which is compatible with the choice of our ToF window.

The anti-coincidence window was fixed to 25 ns. This broad time interval was associated to the poorer time resolution of the BGO compared to the CeBr₃. The threshold for BGO events to trigger the AC rejection was fixed after an analysis of the noise in this secondary detector. In absence of energy deposition in the AC shield, only fluctuations of the baseline were observed. These fluctuations led to a noise peak in the energy spectrum of the BGO events located at low energies. Negative values arising from the baseline fluctuations were also included in the histograms as each event was processed integrating the ADC counts over a fixed time window and subtracting the baseline. We defined σ_{noise} and \bar{E}_{noise} as the parameters of the Gaussian function fitting the noise peak. The threshold was set above the $3 \cdot \sigma_{\text{noise}}$ of the noise distribution, namely at $E_{\text{thr.}} = \bar{E}_{\text{noise}} + 3.5 \cdot \sigma_{\text{noise}}$. After the energy calibration, we assessed that the threshold corresponded to $E_{\gamma} = 150$ keV.

Algorithmic background rejection

The signal-to-noise ratio (SNR) for each discrete peak was calculated adopting the same method used in our previous Monte Carlo study (Dal Bello et al., 2018). This included a combination of background subtraction and fit routines. First, for each spectrum, we computed the continuous background component $BG(E)$ with the dedicated ROOT function included in the TSpec-spectrum class. This was based on the Statistics-sensitive Non-linear Iterative Peak-clipping (SNIP) algorithm (Ryan et al., 1988) and its implementation for the background evaluation of complex gamma rays spectra (Morháč et

al., 1997). Then, we subtracted from the original spectrum the result of the SNIP algorithm $BG(E)$, which included both the continuous component of the prompt gamma emission and the residual Compton continuum. Finally, we fitted the background-subtracted spectrum with multiple Gaussian functions $S_i(E)$. Each Gaussian fit characterized a discrete prompt gamma peak with its energy E_i and its width σ_i . The SNR for each detected peak was then calculated with

$$\text{SNR}_i = \frac{\int_E S_i(\tilde{E})d\tilde{E}}{\int_{E_i-3\sigma_i}^{E_i+3\sigma_i} BG(\tilde{E})d\tilde{E}}. \quad (4.5)$$

The relative SNR_i values, further referred to as $\hat{\text{SNR}}_i$, were obtained dividing the result of (4.5) for the system operated in anti-coincidence by the result of (4.5) for the system with CeBr_3 only. We also compared the experimental $\hat{\text{SNR}}_i^{\text{exp}}$ with the values $\hat{\text{SNR}}_i^{\text{MC}}$ obtained in the previous Monte Carlo study (Dal Bello et al., 2018). We considered the relative deviations for each of the spectral lines $d_i = (\hat{\text{SNR}}_i^{\text{exp}} - \hat{\text{SNR}}_i^{\text{MC}}) / \hat{\text{SNR}}_i^{\text{exp}}$ and then calculated their average \bar{d} .

Background rejection efficiency

We also estimated the absolute efficiency of the AC shield for the selected energy thresholds. For the detection performed with the CeBr_3 only, the number of events was given by $N_1 = N_{\text{PG}} + N_{\text{CC}} + N_{\text{HC}}$. For the detection in anti-coincidence, the number of events was given by $N_2 = N_{\text{PG}} + (1 - f) \cdot N_{\text{CC}} + N_{\text{HC}}$. Moreover, after removing the background calculated with the SNIP algorithm, the number of events left was $N_3 = N_{\text{PG}}$. Where N_{PG} is the number of prompt gamma in the discrete lines, N_{CC} are the events with partial energy deposition in the CeBr_3 , N_{HC} is the number of events in the ^4He induced continuum and f is the fraction of the N_{CC} events removed in anti-coincidence. We approximated $N_{\text{HC}} \simeq 0.1 \cdot N_{\text{PG}}$ (Dedes et al., 2014). We estimated f according to:

$$f = \frac{N_1 - N_2}{N_1 - N_3 + N_{\text{HC}}} \simeq \frac{N_1 - N_2}{N_1 - 0.9 \cdot N_3}. \quad (4.6)$$

Energy calibration

The energy resolution of the CeBr_3 detector in combination with the DAQ system and dedicated off-line analysis, was verified, using an ^{152}Eu source. In this case, we tested the performances of the system in a setup without the beam. We analyzed the spectral line from the ^{152}Sm transition 2^- (1.53 MeV) \rightarrow 0^+ (.122 MeV) producing a $E_\gamma = 1.408$ MeV photon, which follows the electron capture decay of the ^{152}Eu . We chose to verify the energy resolution of the CeBr_3 at this specific energy since it was the most energetic monochromatic gamma emission available with calibration sources at our institute.

On the other hand, during the experimental campaign at HIT we placed a ^{137}Cs source inside the cave. In the post-processing we analyzed the events in the scintillating crystals acquired during beam-on but not in coincidence with a signal in the scintillating plastic. Among these events we selected

the spectral line $E_\gamma = 0.6617$ MeV following the ^{137}Cs decay to calibrate the energy response of the detectors during beam-on conditions. The known position of the high energy spectral lines was used to perform a further fine tuning of the calibration and correcting for the non-linearity. The contribution of such fine tuning was $< 5\%$ on the overall calibration and did not play a critical role in the identification of the spectral lines.

The energy calibration for the AC shield was performed during a dedicated run with beam-on by triggering the DAQ on signals in the BGO. We selected the events in anti-coincidence with the EJ-200 and fitted the position of the ^{137}Cs peak in the corresponding spectrum (not shown).

Targets

Four different targets were used in the experimental measurements:

1. Five flasks filled with double distilled water. The flasks had two polystyrene walls with thickness of $l_{\text{wall}} = 0.15$ cm each and an inner cavity of $l_{\text{cavity}} = 3.2$ cm. These sum up to a total thicknesses in the beam direction: $l_{\text{water}} = 16$ cm and $l_{\text{polystyrene}} = 0.9$ cm. For this target, we estimated the Bragg peak position at a depth of approximately 1.5 cm inside the fifth flask. This is further referred to as the *Water* target.
2. Four PMMA blocks with a thickness in beam direction of $l_i = 5$ cm each, summing up to a total of $l_{\text{PMMA}} = 20$ cm. For this target, we estimated the Bragg peak position at a depth of approximately 3.5 cm inside the third block. This is further referred to as the *PMMA* target.
3. One titanium slab inserted between the third and fourth flask of the water target. The titanium was $l_{\text{Ti}} = 0.6$ cm thick in the beam direction. For this target, we estimated the Bragg peak position at a depth of approximately 3.0 cm inside the fourth flask. This is further referred to as the *Water+Ti* target.
4. One aluminum slab inserted between the third and fourth flask of the water target. The aluminum was $l_{\text{Al}} = 0.25$ cm thick in the beam direction. For this target, we estimated the Bragg peak position at a depth of approximately 1.0 cm inside the fifth flask. This is further referred to as the *Water+Al* target.

The positions of the Bragg peaks for the four different targets were estimated through linear interpolation of the projected ranges tabulated in the ASTAR database ([ASTAR](#)).

Relaxation of statistics requirements

We analyzed two scenarios where statistical considerations are of interest for range control through prompt gamma spectroscopy.

First, we analyzed the stability of the fit of the intensity for the $E_\gamma = 4.4$ MeV peak in the PMMA target case. We indicate with $E_\gamma = 4.4$ MeV the spectral lines due to the two merged transitions $^{12}\text{C}_{4.43}^* \rightarrow ^{12}\text{C}_{g.s.}$ and

$^{11}\text{B}_{4.45}^* \rightarrow ^{11}\text{B}_{g.s.}$. We randomly sampled the total events to artificially reduce the number of entries in the spectrum after the ToF cuts. We then fitted the $E_\gamma = 4.4$ MeV peak and compared its intensity with respect to the spectrum having the maximum number of events, which was assumed as reference. In previous studies with proton beams it was observed that about the Bragg peak the intensity of the $E_\gamma = 4.4$ MeV peak drops from 100% to 0% in about 25 mm (Verburg et al., 2014), i.e. $\pm 4\%$ for every ∓ 1 mm in first approximation. Therefore, to estimate the Bragg peak position with a submillimetric precision one aims to detect the peak intensities with an uncertainty in the order of $\pm 2\%$. We evaluated the number of events necessary to achieve such precision for the $E_\gamma = 4.4$ MeV peak. The simultaneous analysis of independent discrete lines has the benefit to relax this constraint. Therefore, the $\pm 2\%$ could be assumed as the lower limit of the accuracy one has to aim for in order to achieve submillimetric precision.

Then, we analyzed the significance of existence of the $E_\gamma = 0.889$ MeV peak, which is unique to a titanium target. We considered the Water target and the Water+Ti target. We analyzed the spectra in the interval $0.65 \text{ MeV} \leq E_\gamma \leq 1.05 \text{ MeV}$. We performed fits with either two or three Gaussian peaks and calculated the F-statistics. This statistical test assessed the significance of existence of a third reaction channel in the selected interval, namely the $E_\gamma = 0.889$ MeV peak. Moreover, we considered the intensities of the discrete peaks for the Water target I_{Water} and we compared these to the ones obtained with the targets including a metallic insert $I_{\text{Water+Metal}}$.

Finally, we repeated the artificial down-sampling of the data with different random number generators available in ROOT (Brun et al., 1997). We used four different down-sampled data sets to assess the reproducibility of the results and the statistical uncertainty of the extracted parameters.

Results

Detectors performances

Secondary crystal: BGO

The time and energy distributions of the events in the AC shield are presented in Figure 4.17. We first applied a low-energy cut on the BGO events ($E_\gamma < 150$ keV) to select the traces without energy deposition in the AC shield.

The ToF spectrum between BGO and CeBr_3 for the PMMA target is shown in Figure 4.17 (left). It considers the events above the energy cut and presents a primary Gaussian peak with $\mu_{\text{ToF}} = (20.62 \pm 0.01)$ ns and $\sigma_{\text{ToF}} = (1.52 \pm 0.01)$ ns and a secondary peak with $\mu'_{\text{ToF}} = (7.46 \pm 0.01)$ ns and $\sigma'_{\text{ToF}} = (1.31 \pm 0.01)$ ns. The applied cuts included both peaks. In total, 27.8% of the BGO events fell inside the anti-coincidence window and above the energy threshold. Similar performances have been observed for the other targets.

We set a condition to consider the AC shield activated and therefore remove such event from the CeBr_3 spectra: at least one BGO trace should be

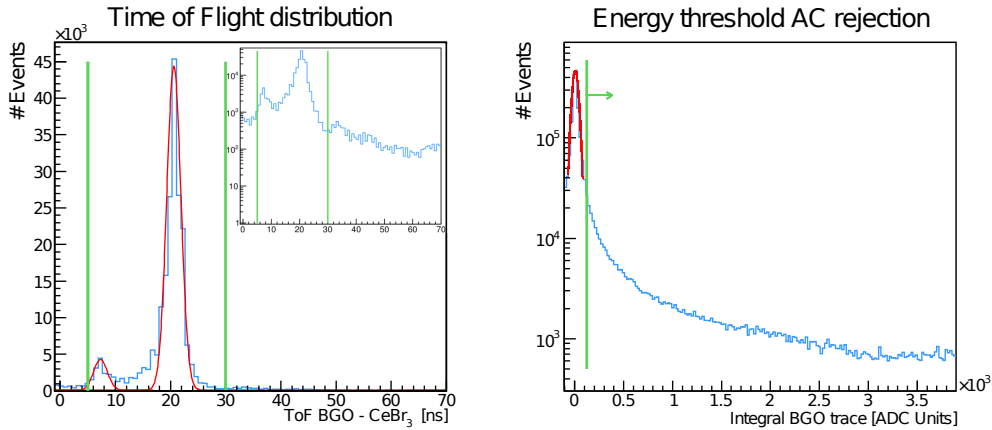


FIGURE 4.17: Energy and time spectra of the BGO events: Time of Flight with respect to the events in the CeBr_3 (left) and energy deposition recorded with the DAQ triggered by the CeBr_3 (right). The insert in the left plot shows the same data in a logarithmic scale. The histograms report the experimental data, the vertical lines indicate the cuts adopted in the off-line data analysis the solid lines represent the Gaussian fits of the regions of interest. In the right plot, the events below the cut correspond to noise fluctuations about the baseline.

above the energy threshold and within the ToF cuts. We calculated the fraction of events with partial energy deposition in the CeBr_3 that were removed by the AC shield. The average over the four different targets was $\bar{f} = 47.3\%$, where the estimation for each setup was done according to (4.6).

Primary crystal: CeBr_3

The energy spectra acquired with the optimized PGS system are presented in Figure 4.18. The use of the optimized BGO shield improves significantly the quality of the spectra by removing a fraction of the events having only a partial energy deposition in the CeBr_3 . We are able to identify more discrete reaction lines in the anti-coincidence spectra. The $E_\gamma = 3.68$ MeV peak generated by the ^{13}C transition $\frac{3}{2}^- (3.68 \text{ MeV}) \rightarrow \frac{1}{2}^- (0.0 \text{ MeV})$ is visible and would be otherwise merged with the single and double escape peaks of the $E_\gamma = 4.4$ MeV line. We also observe that the hydrogen neutron capture line at $E_\gamma = 2.22$ MeV is successfully suppressed by the coincidence between the CeBr_3 and the EJ-200. In particular, we observe the spectral line at $E_\gamma = 2.31$ MeV associated to the ^{14}N transition $0^+ (2.31 \text{ MeV}) \rightarrow 1^+ (0.0 \text{ MeV})$ while a local minimum is present in the spectrum in correspondence of $E_\gamma = 2.22$ MeV.

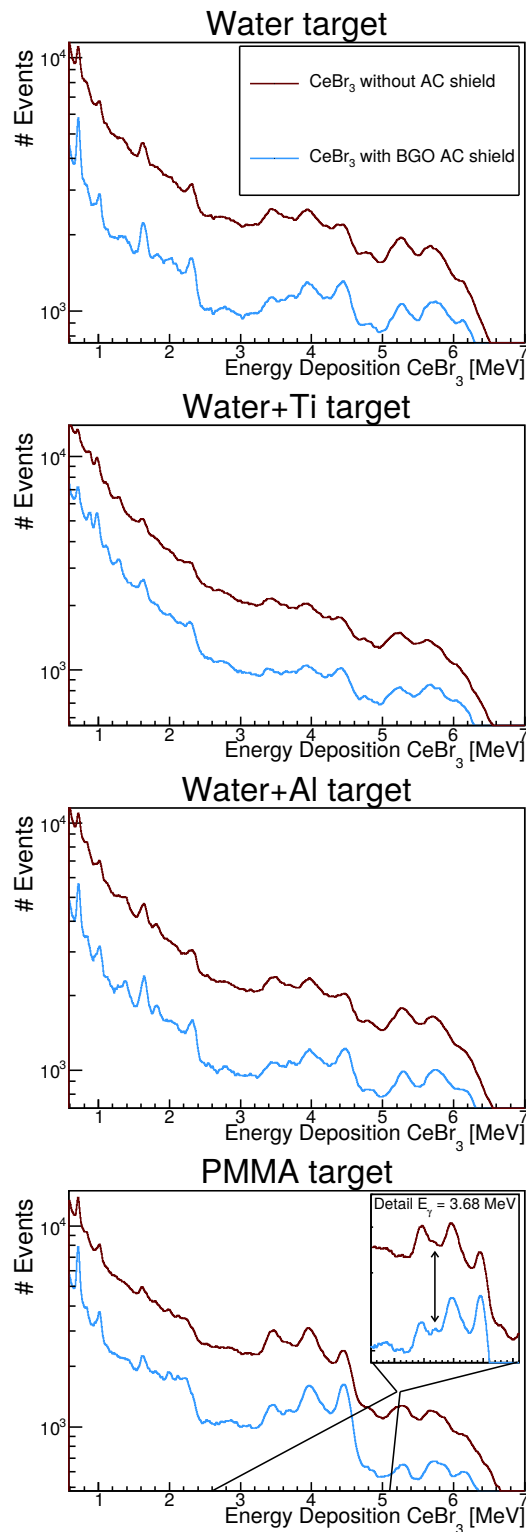


FIGURE 4.18: Energy spectra of the prompt gamma radiation detected with the CeBr_3 alone (dark solid line) or in combination with the anti-coincidence shield (light solid line). From top to bottom: Water target, Water+Ti target and Water+Al target, PMMA target. In the latter, the insert shows the detail for the $E_\gamma = 3.68$ MeV peak, detectable only in anti-coincidence.

Reactions	E_γ [MeV]	$100 \cdot (I_{\text{Water+Metal}} - I_{\text{Water}}) / I_{\text{Water}}$	
		Water+Al	Water+Ti
$^{12}\text{C}_{4.43}^* \rightarrow ^{12}\text{C}_{g.s.}$ $^{11}\text{B}_{4.45}^* \rightarrow ^{11}\text{B}_{g.s.}$	4.4	-10%	-30%
$^{14}\text{N}_{3.94}^* \rightarrow ^{14}\text{N}_{2.31}^*$	1.63	-14%	-31%
$^{15}\text{O}_{7.55}^* \rightarrow ^{15}\text{O}_{6.17}^*$ $^{26}\text{Al}_{1.76}^* \rightarrow ^{26}\text{Al}_{0.416}^*$	1.3	+27%	n.a.
$^{10}\text{B}_{1.74}^* \rightarrow ^{10}\text{B}_{0.718}^*$ $^{48}\text{Ti}_{0.983}^* \rightarrow ^{48}\text{Ti}_{g.s.}$	1.	n.a.	+95%

TABLE 4.3: Relative variations of the intensities for the most intense discrete peaks, obtained introducing a metallic insert in the water target. When multiple reactions produced two discrete peaks with $\Delta E_\gamma < 0.1$ MeV, we merged the results in the same row. The entries indicated with n.a. were irrelevant for the corresponding target and were not reported.

The energy resolution measured without beam of the CeBr₃ detector was $R_{1.408 \text{ MeV}}^{\text{Mes.}} = 3.49\%$. This was in agreement with its nominal value $R_{1.408 \text{ MeV}}^{\text{Ref.}} = 3.47\%$ that we calculated according to the fit of the resolution over a wide energy scale done in previous studies (Roemer et al., 2015).

Analysis of the discrete reaction lines

The spectra were further analyzed to quantify the benefit of the anti-coincidence detection. The SNR for each discrete peak was calculated and the results are presented in Table 4.4. In total, nineteen different discrete reaction lines were analyzed. The system with the AC shield showed an average improvement of the relative SNR by a factor 2.1 with respect to the system with a single CeBr₃ detector.

The discrete energy line at $E_\gamma = 5.2$ MeV was not analyzed, since it was merged with the double escape peak from the $E_\gamma = 6.13$ MeV. The energy line at $E_\gamma = 3.68$ MeV does not have a defined SNR value, since it was not observable at all without the anti-coincidence detection.

The comparison of the spectra obtained from the Water target with respect to the targets including the metal inserts is shown in Figure 4.19. In this case, the spectra are shown in a linear scale and the continuous background has been removed according to the procedure presented in section "Data analysis". The algorithmic background removal enhances the visualization of the discrete peaks but, oppositely to the active background rejection achieved with the secondary detectors, it does not add information to the spectra, i.e. the discrete peaks presented in Figure 4.19 are observable also in Figure 4.18. Four additional low energy peaks appear for

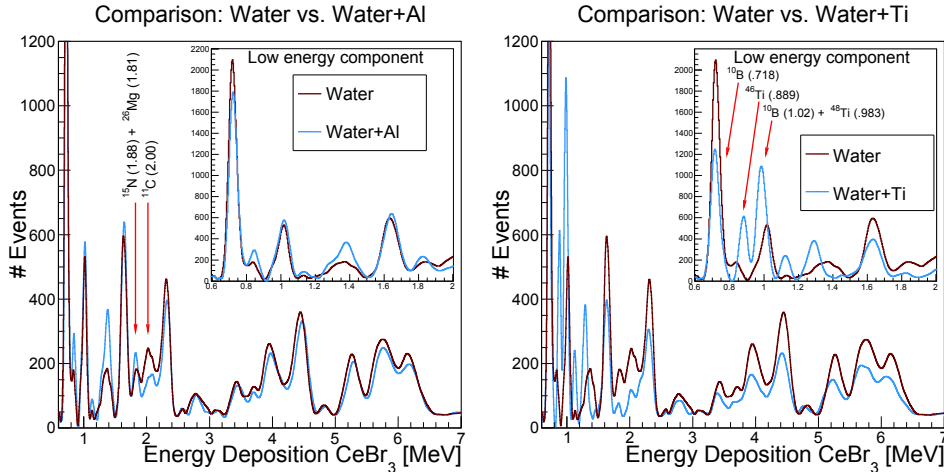


FIGURE 4.19: Energy spectra of the prompt gamma radiation detected with the CeBr_3 in combination with the anti-coincidence shield in presence of the water target (dark solid lines) and the metal slabs (light solid lines). The inserts show the detail of the low energy components of the spectra. The arrows indicate the peaks considered in the analysis to evaluate the presence or absence of the metal insert and the labels report the corresponding nuclei involved in the reactions with the energy of the emitted gamma quanta in brackets in MeV. The comparison is shown between the Water target with respect to the Water+Al target (left) and the Water+Ti target (right).

the Water+Ti target. Two spectral lines are not merged with any oxygen discrete lines, namely the $E_\gamma = 0.889$ MeV produced by the ^{46}Ti transition $2^+(0.889 \text{ MeV}) \rightarrow 0^+(0.0 \text{ MeV})$ and the $E_\gamma = 1.1$ MeV produced by the ^{46}Ti transition $4^+(2.01 \text{ MeV}) \rightarrow 2^+(0.889 \text{ MeV})$ merged with the ^{47}Ti transition $\frac{9}{2}^-(1.25 \text{ MeV}) \rightarrow \frac{7}{2}^-(0.159 \text{ MeV})$. Other two peaks appear for the Water+Al target, which are merged with oxygen discrete lines.

We observed a reduction of the intensity of the discrete lines unique to the Water target in presence of a metal insert. We analyzed few of the most intense spectral lines to quantify this effect, the results are presented in Table 4.3. The most intense effects are observable for the Water+Ti target, in agreement with the fact that the thickness of the metallic insert was the largest. In this case, an increase of the intensities up to +95% is observed for the lines including reactions on titanium and a reduction down to -31% is observed for the lines with reactions unique to the ^{16}O target nuclei.

Reaction	E_γ [MeV]	Reference	SNR for target			
			PMMA	Water	Water+Al	Water+Ti
$^{16}\text{O}_{6.13}^* \rightarrow ^{16}\text{O}_{g.s.}$	6.13	Tilley et al., 1993	2.33	2.14	2.05	2.08
$^{15}\text{O}_{5.24}^* \rightarrow ^{15}\text{O}_{g.s.}$ $^{15}\text{N}_{5.27}^* \rightarrow ^{15}\text{N}_{g.s.}$ $^{14}\text{N}_{5.11}^* \rightarrow ^{14}\text{N}_{g.s.}$	5.2	Ajzenberg-Selove, 1991 Ajzenberg-Selove, 1991 Ajzenberg-Selove, 1991	Merged with D.E. peak of $E_\gamma = 6.13$ MeV			
$^{12}\text{C}_{4.43}^* \rightarrow ^{12}\text{C}_{g.s.}$ $^{11}\text{B}_{4.45}^* \rightarrow ^{11}\text{B}_{g.s.}$	4.4	Kelley et al., 2017 Kelley et al., 2012	2.05	2.03	2.04	1.99
$^{13}\text{C}_{3.68}^* \rightarrow ^{13}\text{C}_{g.s.}$	3.68	Ajzenberg-Selove, 1991	Not observable without the BGO			
$^{12}\text{C}_{7.65}^* \rightarrow ^{12}\text{C}_{4.44}^*$	3.21	Kelley et al., 2017	1.95	-	-	-
$^{16}\text{O}_{8.87}^* \rightarrow ^{16}\text{O}_{6.13}^*$ $^{11}\text{C}_{4.80}^* \rightarrow ^{11}\text{C}_{2.00}^*$	2.8	Tilley et al., 1993 Kelley et al., 2012	1.82	1.69	2.45	1.73
$^{14}\text{N}_{2.31}^* \rightarrow ^{14}\text{N}_{g.s.}$	2.31	Ajzenberg-Selove, 1991	2.70	2.26	2.27	2.07
$^{11}\text{C}_{2.00}^* \rightarrow ^{11}\text{C}_{g.s.}$	2.00	Kelley et al., 2012	3.36	4.37	5.30	2.72
$^{15}\text{N}_{7.15}^* \rightarrow ^{15}\text{N}_{5.27}^*$	1.88	Ajzenberg-Selove, 1991	3.09	1.64	1.68 ^a	1.43
$^{26}\text{Mg}_{1.81}^* \rightarrow ^{26}\text{Mg}_{g.s.}$	1.81	Basunia et al., 2016	-	-	1.68 ^a	-
$^{14}\text{N}_{3.94}^* \rightarrow ^{14}\text{N}_{2.31}^*$	1.63	Ajzenberg-Selove, 1991	1.73	2.05	1.97	1.72
$^{15}\text{O}_{7.55}^* \rightarrow ^{15}\text{O}_{6.17}^*$	1.38	Ajzenberg-Selove, 1991	-	1.79	1.87 ^b	1.68 ^a
$^{26}\text{Al}_{1.76}^* \rightarrow ^{26}\text{Al}_{0.416}^*$	1.34	Basunia et al., 2016	-	-	1.87 ^b	-
$^{46}\text{Ti}_{3.29}^* \rightarrow ^{46}\text{Ti}_{2.01}^*$ $^{47}\text{Ti}_{1.44}^* \rightarrow ^{47}\text{Ti}_{0.159}^*$ $^{48}\text{Ti}_{2.29}^* \rightarrow ^{48}\text{Ti}_{0.983}^*$	1.3	Wu, 2000 Burrows, 2007 Burrows, 2006	-	-	-	1.68 ^a
$^{46}\text{Ti}_{2.01}^* \rightarrow ^{46}\text{Ti}_{0.889}^*$ $^{47}\text{Ti}_{1.25}^* \rightarrow ^{47}\text{Ti}_{0.159}^*$	1.1	Wu, 2000 Burrows, 2007	-	-	-	1.87
$^{10}\text{B}_{1.74}^* \rightarrow ^{10}\text{B}_{0.718}^*$	1.02	Tilley et al., 2004	2.04	2.04	1.99	2.02 ^b
$^{48}\text{Ti}_{0.983}^* \rightarrow ^{48}\text{Ti}_{g.s.}$	0.983	Burrows, 2006	-	-	-	2.02 ^b
$^{46}\text{Ti}_{0.889}^* \rightarrow ^{46}\text{Ti}_{g.s.}$	0.889	Wu, 2000	-	-	-	2.09
$^{10}\text{B}_{0.718}^* \rightarrow ^{10}\text{B}_{g.s.}$	0.718	Tilley et al., 2004	2.58	2.53	2.67	2.44
Mean relative deviation from Dal Bello et al., 2018			-	-3.6%	+2.1%	-

TABLE 4.4: Relative signal-to-noise values for the discrete peaks observed in the spectra. The SNR are given for the system CeBr₃+BGO with respect to the system CeBr₃ only. The letter superscripts indicate the aluminum and titanium lines that are merged with lines from water in the same column. The relative uncertainties of the SNR values are below 1%. The last row reports the average deviation with respect to the Monte Carlo predictions for the targets in common in the two studies.

Relaxation of statistics requirements

The adoption of the optimized anti-coincidence shield showed not only an improvement in the SNR values, but also more relaxed requirements on the number of events necessary to draw statistically significant conclusions. The results based on the random number generator TRandom3 to down-sample the data are presented in Figure 4.20. We observed that with the BGO we require in average a factor 2.4 ± 0.9 less events to converge inside the $\pm 2\%$ confidence interval for the intensity fit of the $E_\gamma = 4.4$ MeV peak in presence of the PMMA target. In the specific setup used for our experiments the convergence in anti-coincidence detection was achieved with $(1.9 \pm 0.4) \cdot 10^9$ primary ${}^4\text{He}$ ions. While the number of primary particles strongly depends on the geometrical setup of the experiment, the efficiency of the beam trigger and the number of CeBr_3 crystals adopted; the number of events in the CeBr_3 to reach convergence is a constant value for the spectroscopic unit analyzed. In Figure 4.20 (left) the convergence has been achieved with $4 \cdot 10^5$ total events in the CeBr_3 . Similar results have been observed for other down-sampled data based on different random number generators. The results also show that with the BGO we require in average a factor 4.3 ± 1.9 less events to converge below the $\alpha = 0.01$ significance level for the existence of the $E_\gamma = 0.889$ MeV peak in presence of the Water+Ti target. In the specific setup used for our experiments the convergence in anti-coincidence detection was achieved with $(2.9 \pm 0.9) \cdot 10^8$ primary ${}^4\text{He}$ ions. In Figure 4.20 (right) the convergence has been achieved with $2 \cdot 10^5$ total events in the CeBr_3 . Similar results have been observed for other down-sampled data based on different random number generators.

Discussion

The adoption of the optimized CeBr_3 crystal surrounded by the dedicated BGO anti-coincidence shield showed a significant increase in the spectroscopic performances. The experimentally evaluated signal-to-noise confirmed the Monte Carlo predictions of our previous study (Dal Bello et al., 2018), in particular we observed an overall improvement of a factor 2.1 compared to the factor 2 from the simulations and the average deviations for each target were limited to $|\bar{d}| \leq 3.6\%$. The probability of activation of the AC shield in the experiments (27.8%) was also aligned to the one obtained in the previous Monte Carlo study (26.75%). Moreover, we were able to detect some discrete reaction lines with the AC shield that would have been otherwise not observable without this secondary detector. The most significant example was clearly shown in Figure 4.18 for the PMMA target, where the ${}^{13}\text{C}$ transition $\frac{3}{2}^-$ (3.68 MeV) \rightarrow $\frac{1}{2}^-$ (0.0 MeV) emerges from the background. Without the BGO, this discrete line would be merged with the single and double escape peaks from the $E_\gamma = 4.4$ MeV line.

We verified the nominal energy resolution of the CeBr_3 with radioactive sources. We observed an additional broadening of the high-energetic spectral lines from the irradiated targets. This could be interpreted as a Doppler

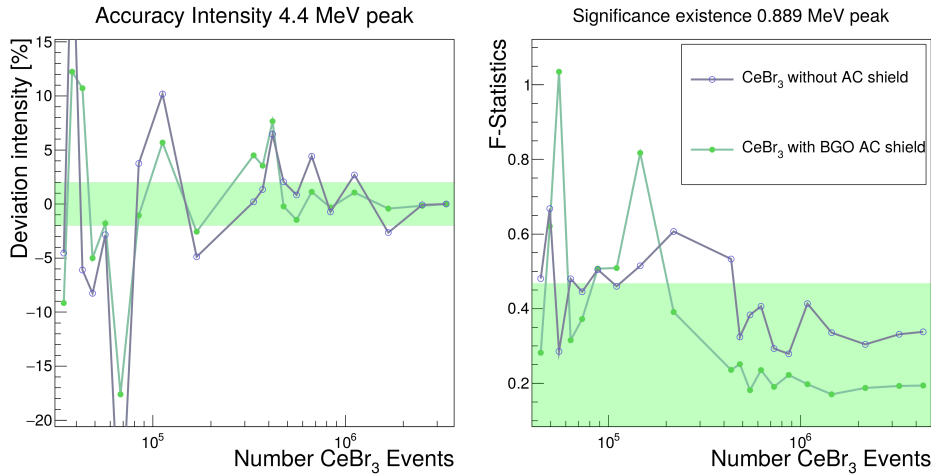
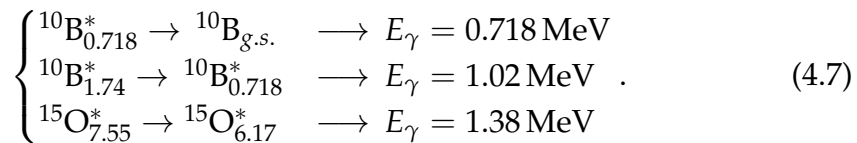


FIGURE 4.20: Evolution of the parameters extracted from the spectra with respect to the number of events analyzed. Stability of the fit of the intensity of the $E_\gamma = 4.4$ MeV peak for the PMMA target until convergence inside the $\pm 2\%$ confidence interval (left). F-statistics for the existence of the $E_\gamma = 0.889$ MeV peak in the Water+Ti target until convergence below the $\alpha = 0.01$ significance level (right). The solid circles indicate the case with BGO and the empty circles the case without. The lines are introduced to help the reader to follow the convergence until the highlighted region. The down-sampling was based on the random number generator TRandom3 in ROOT.

broadening effect which grows with the increasing mass of the projectile. Therefore, greater importance was given to the analysis of the low energy component of the discrete spectrum, which is possible due to the low intrinsic activity of the CeBr_3 crystal. Other scintillating crystals used in PGS, such as the LaBr_3 , perform better at high energies but are limited in the low-energy region to the $E_\gamma = 1.63$ MeV peak (Hueso-González et al., 2018).

The superior performances of the CeBr_3 with respect to the LaBr_3 for $E_\gamma < 3$ MeV have been proven in previous studies for general application purposes (Quarati et al., 2013). In the present study, we specifically analyzed the impact of the higher detection sensitivity for PGS applications. We demonstrated that the use of CeBr_3 opens the possibility to include in the analysis several spectral lines below the previous limit of $E_\gamma = 1.63$ MeV. We observed eight additional discrete lines below this energy, three of which were related to reactions on the ^{16}O target. In particular, the prompt gamma emission lines following reactions on ^{16}O nuclei were:



The possibility to detect the reactions in (4.7) has the benefit of increasing by three the number of prompt gamma lines to be used for PGS, additionally to

the seven in use by the MGH system (Hueso-González et al., 2018). This increases the number of independent variables by over +40% promising an improvement in the accuracy in the detection of the ion range for future clinical applications. However, the correlation of the cross-sections for the reactions in (4.7) with the residual beam energy, i.e. the Bragg peak position, has to be verified. The presence of metal inserts in the target was observable strictly in this low energy component. Therefore, the detection of the interaction between the ion beam and high-Z inserts is restricted to PGS performed with CeBr₃. This feature could be exploited for patients having the target volume close to metallic implants. In such a scenario, the analysis of the detected spectrum could assess whether the metallic structure was or was not located along the beam path during the treatment. Further clinical applicability may include patient with implanted seeds (Lim et al., 2009, Cheung et al., 2010). In general, this considerations are valid for high-Z materials that, in contrast to light nuclei, emit prompt gamma radiation mainly in the low energy component of the spectrum. Additionally, the annihilation line $E_\gamma = 0.511$ MeV could also be measured (not shown).

For what concerns the prompt gamma lines with $E_\gamma > 3$ MeV, other crystals such as the LaBr₃ are known to have a better energy resolution. Specifically, the FWHM for CeBr₃ is expected to be approximately $108/81 = +33\%$ wider compared to LaBr₃ (Quarati et al., 2013). However, this does not hinder the capability to detect the seven reaction lines from $E_\gamma = 1.63$ MeV to $E_\gamma = 6.13$ MeV. A drawback of the poorer energy resolution is the fact that the $E_\gamma = 5.2$ MeV peak is merged with the double escape peak of the $E_\gamma = 6.13$ MeV. The use of post-processing routines including a detector response model is foreseen for future applications and expected to mitigate this effect (Guttormsen et al., 1996). Moreover, the detection of the high energy spectral lines suffers not only from a lower energy resolution, but also from Doppler broadening. The magnitude of this phenomenon is maximum for a non-collimated geometry, i.e. we analyzed the worst case scenario. In our experiments we detected the prompt gamma emission induced by reactions over the full energy range of the ⁴He ions, namely from $E_0^{\text{kin}} = 149.02$ MeV/u ($\beta = 0.51$) to rest ($\beta \rightarrow 0$). Nevertheless, we demonstrated the capability of the spectroscopic unit to detect the high energy lines up to $E_\gamma = 6.13$ MeV. We gave great importance to the experimental implementation of the AC shield. By virtue of the active background rejection it is possible to compensate for the lower performances of the CeBr₃ at $E_\gamma > 3$ MeV and achieve the convergence of the analyzed parameters with a statistically significant smaller number of events.

The aluminum energy lines were merged with the oxygen lines. In particular, the transition $^{26}\text{Mg}_{1.81}^* \rightarrow ^{26}\text{Mg}_{g.s.}$ producing a $E_\gamma = 1.81$ MeV photon was merged with the transition $^{15}\text{N}_{7.15}^* \rightarrow ^{15}\text{N}_{5.27}^*$ producing a $E_\gamma = 1.88$ MeV photon. This spectral line is further referred to as $E_\gamma = 1.8$ MeV.

Nonetheless, after an accurate analysis of the spectrum, it was possible to retrieve a unique signature of the presence of this metal along the beam path. The reactions on the aluminum target increased the intensity of the $E_\gamma = 1.8$ MeV peak, while the $E_\gamma = 2.0$ MeV peak intensity decreased since

it was unique to reactions on ^{16}O nuclei. As shown in Figure 4.19, the net effect is an increased $I_{2.0\text{ MeV}}$ with respect to the $I_{1.8\text{ MeV}}$ in the absence of the metal ($I_{2.0\text{ MeV}} > I_{1.8\text{ MeV}}$) and an opposite effect for the Water+Al target ($I_{2.0\text{ MeV}} < I_{1.8\text{ MeV}}$). It is noticeable that the effect on the prompt gamma spectra was well observable even if the size of the insert was relatively small, i.e. ratio between the beam paths in aluminum and water was 1/64. Finally, two more reactions were merged in a unique spectral line. Namely the transition $^{26}\text{Al}_{1.76}^* \rightarrow ^{26}\text{Al}_{0.416}^*$ producing a $E_\gamma = 1.34\text{ MeV}$ photon and the transition $^{15}\text{O}_{7.55}^* \rightarrow ^{15}\text{O}_{6.17}^*$ producing a $E_\gamma = 1.38\text{ MeV}$ photon. This spectral line is further referred to as $E_\gamma = 1.3\text{ MeV}$. A significant increase of the intensity of the energy line at $E_\gamma = 1.3\text{ MeV}$ was also observed.

There are titanium energy lines that are unique to this metal and not observable in the water target alone. These are the $E_\gamma = 1.1\text{ MeV}$ and the $E_\gamma = 0.889\text{ MeV}$ peaks. The energy lines at $E_\gamma = 1.3\text{ MeV}$ and $E_\gamma = 0.983\text{ MeV}$ were merged with the ^{16}O lines and their intensity is therefore increased for the Water+Ti target.

In general, whenever a metal insert was added in the water target, we observed that the intensity of the oxygen lines was reduced. The quantification of this effect was reported in Table 4.3. This could be interpreted by the fact that given a fixed number of primary ^4He particles, the presence of a metal slab leads to a decrease of the number of ^4He that interact with inelastic nuclear reactions with ^{16}O and to an increase of the reactions with aluminum or titanium. The amplitude of this effect was significant and we can interpret this in the light of two geometrical properties of the experimental setup. First, the metal inserts were placed just before the Bragg peak where the total cross section for nuclear reactions is expected to have its maximum values. Second, the spectroscope was aligned to the fourth flask and the metal slabs were inserted just upstream is, therefore having a minimal metal-detector distance. Nevertheless, this could be considered representative of a possible clinical application. In presence of a patient with a metallic implant close to the target volume, one would place the spectroscope without any collimation as close as possible to the position where the metal is expected to be. In such a clinical scenario, both geometrical conditions adopted in our experiment would apply.

When adopting the AC shield not only the SNR for the detection of the discrete peaks improved, but also a relaxation of the statistical requirements to robustly extract parameters from the spectra was observed. The quantitative evaluation of these effects was performed with a series of statistic analysis.

Conclusions

We presented the first experimental results for prompt gamma spectroscopy applied to ^4He beams at clinically relevant intensities and energies. The optimized detector based on CeBr_3 surrounded by BGO has been proven to provide an excellent performance, especially for the low energy component of the prompt-gamma energy spectrum. This has the potential to increase by

over +40% the number of independent variables to be used for range verification in patients through PGS. In the low energy region, it was even possible to identify unique energy lines from metal inserts. This feature could have an applicability for patients with metallic implants close to the target volume. The presence of the BGO anti-coincidence shield also allowed for a significant relaxation of the statistical requirements.

Acknowledgments

Author R.D.B. is supported by the International Max Planck Research School for Quantum Dynamics in Physics, Chemistry and Biology, Heidelberg, Germany. P.M.M. is supported by a research fellowship for postdoctoral researchers from the Alexander von Humboldt Foundation, Bonn, Germany. The authors thank the staff of the Heidelberg Ion-Beam Therapy Center (HIT), Heidelberg, Germany, in particular Dr. Stephan Brons for the technical support. The authors thank also the radiation protection department of the DKFZ, in particular Dipl.-Ing. Mechthild Kämmer, for the support with calibration sources.

4.4 Development and characterization of the beam trigger

Title : Hadron beam time tracker for time-of-flight measurements of prompt-gamma

Authors : Paulo Magalhaes Martins, Riccardo Dal Bello, Michael Seimetz, German Hermann, Thomas Kihm and Joao Seco

Status : Under review

Journal : Nuclear Instruments and Methods in Physics Research Section A

Copyright : Ownership of the copyright not transferred to any publisher yet

Contributions : P.M.M. designed and performed the experiments. R.D.B., attended and provided support during the experimental campaigns and he contributed to the design of the experiments and interpretation of the results. The last author, J.S., coordinated the project and provided guidance during the design of the detector. The third to fifth authors, M.S., G.H. and T.K., provided support with the detector and electronics used in the experimental setup. M.S. manufactured the trigger according to the design developed together with R.D.B., P.M.M. and J.S. The first author, P.M.M., conducted the post-processing of the experimental data and he wrote the software to perform the quantitative analysis. P.M.M., R.D.B. and the co-authors concluded the studying reporting quantitative parameters that demonstrate the scintillating fiber trigger for time resolved detection of prompt gamma radiation. The detector is adopted in the final manuscript included in this thesis.

Abstract

The tracking of single particles accelerated by synchrotrons is a subject that crosses several physics fields. The high clinical intensities used in particle therapy that can exceed 10^9 p/s make this task very challenging. The tracking of the arrival time of a single particle in the ion beam is fundamental for the verification of that particle range and dose delivery to the patient. We present a prototype from scintillating fibers that was able to provide time-of-flight (TOF) information for three beam species currently accelerated at the Heidelberg Ion-Beam Therapy Center (HIT). We demonstrated a time-tracker for a prompt-gamma spectroscopy system that allows for a background TOF rejection with a time resolution of 0.8 ns FWHM.

Introduction

The correlation between the ion beam microstructure and the prompt-gamma ray production in synchrotron facilities has been investigated in the context of therapy monitoring by means of in-beam PET imaging (Parodi et al., 2005; Crespo et al., 2005). The prompt-gamma ray emissions during ion-beam therapy, at that time still considered mostly a source of background, eventually became a promising technique for range verification (Jongen et al., 2003). Several authors have meanwhile investigated the benefits of time-of-flight (TOF) measurements for background rejection in prompt gamma imaging (PGI) (Testa et al., 2008; Biegun et al., 2012; Smeets et al., 2012; Verburg et al., 2013b; Golnik et al., 2014; Cambraia Lopes et al., 2015). In cyclotron-based facilities, the use of the TOF information is rather straightforward as the arrival time of the proton bunches is highly correlated with the radio-frequency (RF) of the accelerator, being the bunch width in the order of 1–2 ns. However proton bunch drifts against the RF of the cyclotron have been observed (Petzoldt et al., 2016). In synchrotron facilities, a time-correlation of the prompt gamma radiation with the residual microstructure of the extracted beam is still observed (Parodi et al., 2008), but the minimum bunch width is in the order of 10 ns. The information obtained thereof may be sufficient to track the inter- and intra-spill time between spills and bunches, respectively, to be used for in-beam PET. However, it is not sufficient for defining a useful TOF window for PGI. Provided the distance from the prompt-gamma detector to the target, typical TOF windows are usually within 1–3 ns (Verburg et al., 2014; Hueso-González et al., 2015; Cambraia Lopes et al., 2015; Magalhaes Martins et al., 2017). Many experiments in high-energy physics have achieved sub-ns TOF resolutions. Several types of detectors have been used in those experiments, such as plastic scintillator slabs (Gil et al., 2017), resistive plate chambers (Schüttauf, 2004; Alici, 2012; Blanco et al., 2013) and strip silicon detectors (Sadrozinski et al., 2018; Cartiglia et al., 2017; Sadrozinski et al., 2016). The plastic scintillator detectors have also been widely investigated for radiation dosimetry by Beddar et al., 1992a; Beddar et al., 1992b and Beddar et al., 2016. Many facilities use plastic scintillator counters for beam

monitoring. In the therapy with ion beams, plastic detector counters are usually placed after the beam extraction. However, this solution is just available during quality assurance, since the particles hitting the detector will be scattered and will not reach the nozzle. Testa et al., 2008 have proposed the use of an external beam monitor between the nozzle and the patient to determine the time correlation between the prompt gamma detection and the transverse position of the incident ions measured by the monitor. Several solutions for spatial tracking have meanwhile been presented either based on diamond detectors (Gallin-Martel et al., 2018), or based on plastic scintillating fibers (Kirn, 2017; Leverington et al., 2018). The aforementioned strip silicon detectors have presented promising results for beam characterization and monitoring in a clinical setting (Vignati et al., 2017). Several authors claimed the need for bunch monitors to create reliable range verification procedures in the clinical routine (Petzoldt et al., 2016; Krimmer et al., 2018; Pausch et al., 2018a; Hueso-Gonzalez et al., 2019). In this work, we present a prototype of a start detector capable of providing distinct time references for single particles accelerated at the Heidelberg Ion-Beam Therapy Center - HIT (Haberer et al., 2004). The information of the arrival time of those particles is correlated with the prompt-gamma arrival time measured in the CeBr₃ detectors to assess the system time resolution. The bunch width and interval for several beam species and energies are also shown thus demonstrating the need for such an external trigger. Finally, we evaluate the energy deposition for beam diagnostic purposes and provide results on the efficiency of tracking single particles.

Requirements to the Prototype

The main requirements to our prototype are: tracking the arrival time of single particles within an ion beam provided by a synchrotron; providing a sub-ns system time resolution; being able to cope with clinical intensities; being radiation hard; interacting as few as possible with the beam.

In this work, we will focus on the first three requirements. The further requirements have been addressed elsewhere (Joram et al., 2015; Ekelhof, 2016; Leverington et al., 2018).

Materials and Methods

The HIT facility accelerates proton, helium, carbon, and oxygen ions from 48 MeV/u up to 515 MeV/u. While protons and carbon ions are routinely implemented in the clinical setting, helium ions are currently being commissioned (Tessonier et al., 2018; Mein et al., 2019), and oxygen ions still remain as a research beam species. In this work, we focus just on proton, helium and carbon ion beams.

The intensities in clinical practice range from 2×10^6 p/s for carbon ions to 2×9^{10} p/s for protons. There are however 15 intensity levels for each beam species. The intensity is controlled via an intensity feedback system

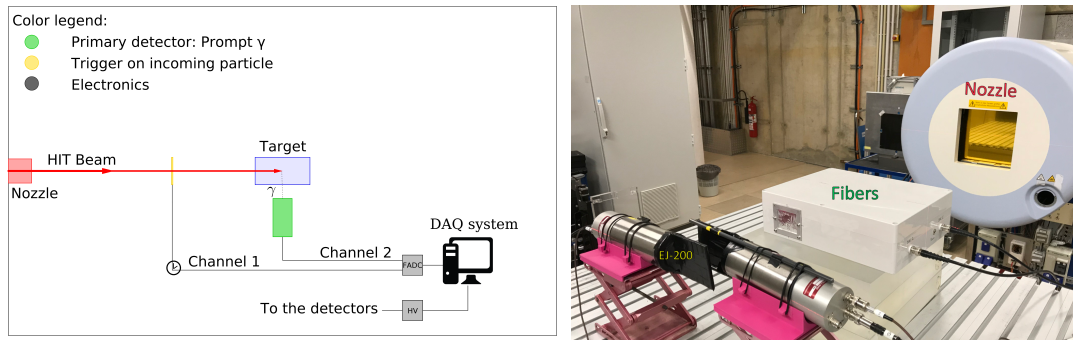


FIGURE 4.21: Left: Schematic drawing of the first experimental setup comprising the PGS system and an external trigger detector between the nozzle and the target. Right: Photo of the second experimental setup with the scintillating fibers and the EJ-200 scintillating tiles placed, in sequence, along the beam axis.

(Schoemers et al., 2015). This system can however be switched off for achieving lower intensities. In that case, the beam can be bended via magnets up to 1° and the intensity at the nozzle lowered down to approximately 30–50 particles per second. The intensity can also be artificially changed by demanding a certain charge in the ionization chambers through the intensity feedback system. The latter is suitable to deliver intensities down to three orders of magnitude of the lowest clinical intensity (8×10^4 p/s for protons and 2×10^3 p/s for carbon ions).

The HIT facility is equipped with two clinical horizontal rooms, a fully 360° gantry and an horizontal experimental room. All the experiments were performed in the experimental room, i.e. at the largest distance from the extraction point.

Experimental Setup

The prompt gamma spectroscopy (PGS) system is composed of CeBr_3 detectors ($\varnothing 1.5'' \times 3''$) coupled to Hamamatsu R13089 photomultiplier tubes (PMTs) and plugged to a voltage divider. The anode output feeds our data acquisition system (DAQ) (Werner et al., 2017). This is a module of a Flash-Cam FADC system, originally designed for the Cherenkov Telescope Array (CTA) (Actis et al., 2011).

Fig. 4.21 shows a schematic drawing of our PGS system consisting of a primary prompt-gamma detector, a trigger for the incoming particles, and the electronics. The focus of the present study is the external trigger placed between the nozzle and the target and the TOF information on the incoming particles extracted thereof. Moreover, we performed experiments also with a second setup. In this case, the target and the CeBr_3 were removed, while a EJ-200 scintillating tile was introduced. The trigger and the scintillating plastic were placed along the beam axis to detect, in sequence, the beam particles delivered by the synchrotron.

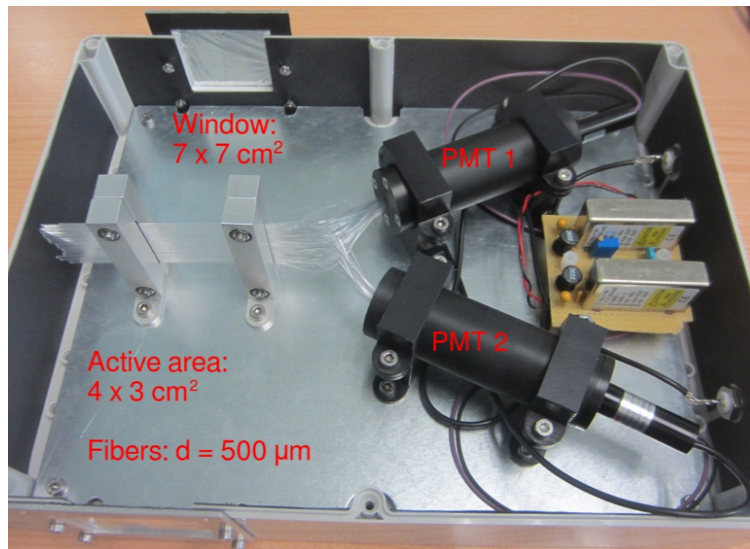


FIGURE 4.22: Photo of the prototype comprising scintillating fibers connected on one side to two independent PMTs in an alternating fashion.

Trigger

We considered several options for our trigger. In a previous study, we used plastic scintillators and showed their ability to provide TOF information (Dal Bello et al., 2019). These detectors are commonly used as start counters, but have a limited count rate of approximately 10^6 cps. We chose EJ-200 scintillating plastics with a squared area of $8 \times 8 \text{ cm}^2$ and a respective thickness of 1 and 4 mm. Each of these was sealed with aluminum foil and black tape to make it light tight and coupled on one side with a silicone coupling component to a Hamamatsu PMT R13089.

For the prototype presented in this study, we considered a set of scintillating fibers with a square cross section of $500 \mu\text{m}$. We designed dedicated supports to obtain a single layer of scintillating fibers (BCF-12, Saint Gobain Crystals). The total active area was $4 \times 3 \text{ cm}^2$. The fibers were connected on one side to two independent R647 PMT with E849-35 socket assembly (Hamamatsu) in an alternating fashion. The detector included an housing for light shielding equipped with an entrance and exit window for the beam (double aluminized mylar with a total thickness of $10 \mu\text{m}$). The PMTs are connected to two independent anode readout channels. High voltage supply modules are integrated in the prototype and powered by an external 12 V DC plug. The pulse heights of the two channels have been pre-adjusted with a Sr-90 source. Fig. 4.22 shows a photograph of the prototype without the top cover.

Data acquisition, processing and analysis

Our DAQ system has 6 sockets and 24 channels. Each socket is capable of acquiring 4 independent channels at 250 MS/s with 12-bit precision. There is the option to cluster those 4 channels and acquire at 1 GS/s by phase shifting

every channel by 1 ns. We used this clustering technique to acquire the data from the two PMTs outputs within our scintillating fiber box and the PMTs outputs from both plastic detectors. In total, to test both trigger options, we used 16 channels (4 channels for each PMT). Concerning the CeBr₃ detector, a larger sampling interval of $\delta t = 4$ ns was considered. The signals in the CeBr₃ were only compared to the ones in the fibers. The maximum throughput of the DAQ system is approximately 200 kcps.

The data was continuously streamed from the DAQ to the PC through Gigabit Ethernet and stored in listmode data files. Those files were then converted to independent binary files containing the information of each trace, the relative time assigned to the event, the deadtime, and a standalone energy calculation. All the data pulse processing and analysis were carried out offline in self-designed MATLAB routines.

In order to retrieve the arrival time and energy of the particles in every detector, we shaped the digital signal by convolving the input signal with an impulse response function. For fast evaluation and visualization purposes, we acquired traces of 16 μ s (3980 samples). This acquisition mode displays the bunch structure within 16 μ s and permits a fast visualization of pile-up events. A supplemental video shows the single carbon particles arriving within the course of a single spill. These large traces were also used to determine the bunch width and interval for several beam species with different energies.

In order to determine the system time resolution and the intrinsic resolution of the fibers, we acquired traces of 240 ns (60 samples without clustering or 240 samples after clustering). The coincidences between the events in the scintillating fibers and the events in the plastic detectors or in the CeBr₃ detector were performed offline after digital pulse processing. In order to determine the arrival time stamp, we adapted the MATLAB function *findpeaks* for better performance. A maximum of 3 peaks per trace and a minimum peak prominence on the processed data were considered. The time stamp corresponded to the half width at half height. Three gaussian functions were analytically calculated with the values of the local peaks and widths and their maximum considered for calculating the energy deposition. All data were corrected for deadtime.

Decomposition of the cross-talk between neighbouring fibers

During the manufacturing process, we deliberately avoided any cladding in order to avoid dead regions between the scintillating fibers. Therefore, we observed a cross-talk between neighboring fibers, this effect being more evident for incident carbon ions. Every time we observe a single event from a carbon ion in an odd (even) fiber we observe a cross-talk event with smaller light yield in the even (odd) fiber. The highest signal can be decomposed from the smaller one by evaluating the energy deposition in both odd and even fibers. After setting a threshold and performing simple logic operations, we can decompose the events in four components: a) the valid events that have an energy deposition in the odd or even fibers above that threshold

and which generated an event in the neighboring fiber below that threshold; b) the events with an energy deposition in the odd or even fibers below the threshold and a signal above the threshold in the neighboring fiber; c) events that generated a signal above the given threshold in both odd and even fibers; d) events that generated a signal below the given threshold in both odd and even fibers.

Spill structure

The spill macrostructure comprehends a period of approximately 5 s of irradiation followed by a pause of approximately 4 s. In order to determine the initial and final part of each spill, we use the reference clock of the FADC that runs at 250 MHz. This clock assigns a very precise relative time stamp to each event. To determine both the spill start and end, we calculated the first and second derivatives of the trigger time course (inversely proportional to the count rate) provided by the FADC clock. During the spill on, we have many events close-by in time. Conversely, during spill off, very few events are detected. In the presence of a CeBr_3 detector, we could use the time derivative of the energy deposited in the CeBr_3 or the presence of overflows generated by scattered charged particles hitting directly the CeBr_3 , as they immediately arise during spill on. During spill off, there is just the activation of the target with gamma-rays being emitted with an energy of 511 keV. Conversely, during spill on, the high energetic prompt-gammas immediately provide the information that the spill started. Finally, we used an external radioactive source to provide a continuous count rate even during spill off. This method is quite accurate within a few milliseconds. In the supplemental movie, we can clearly see the start and the end of the carbon ion spill with 16 μs traces. Fig. 4.23 shows a straightforward method for determining the spill start and end by defining a threshold on the energy deposited in the trigger detector. During spill off, there are still activation related events acquired by the CeBr_3 , but without any energy deposition in the fibers.

Single Particle Tracking

Fig. 4.24 (left) shows the time microstructure of beams of protons (bottom), helium (middle), and carbon (top). Displayed are the 16 μs traces acquired with both odd (top) and even (bottom) fibers. We observe a very regular time microstructure for the helium beams due to the very low energy. The beam travels the shortest distance from the injector to the nozzle with very few turns in the synchrotron.

Fig. 4.24 (right) shows a zoom over a smaller time period, where the single particles are clearly distinguishable. For proton beams, we can even distinguish double and higher order hits within a bunch of particles. However, some multiple hits cannot be resolved for such intensity (8×10^7 p/s). For carbon ions, the cross-talk between odd and even fibers is clearly visible. Every hit in an odd or even fiber creates a simultaneous but smaller hit in the

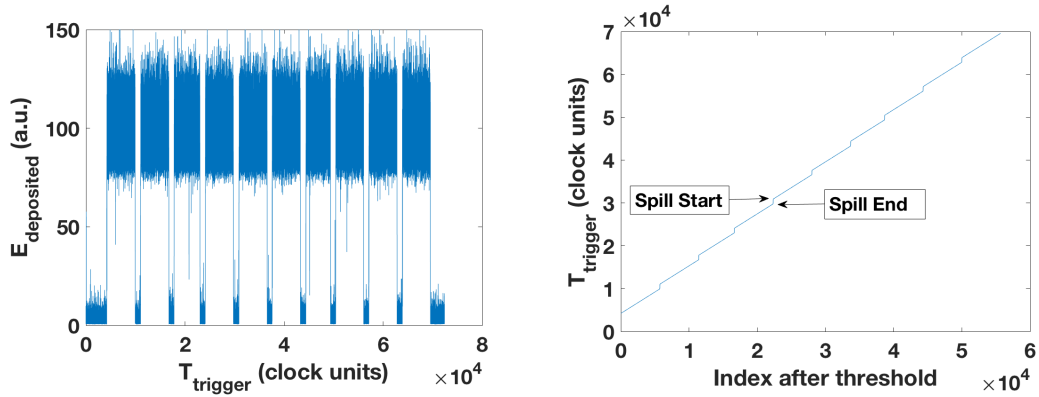


FIGURE 4.23: Left: Energy deposited in the trigger detector along the acquisition time. The relative acquisition is given by the internal clock of the FADC unit. Right: After setting a threshold at 60 (a.u.), we obtain the index of the spill start and the spill end and the corresponding trigger time given by the FADC unit. The time difference between those times gives the time between spills.

neighboring fiber. Fig. 4.25 shows an exemplary multiple hit with four events within 200 ns from a proton beam. These four events would overlap and be discarded without the clustering technique.

The movie 4.26 shows the arrival time of carbon ions within the course of a spill. The spill starts with a low particle rate within the first milliseconds and achieves the requested intensity afterwards. It eventually vanishes after approximately 4.85 s. The ramp-up time was already observed by Schoemers et al., 2015.

Bunch width and interval

Fig. 4.27 shows an histogram of the arrival time of the helium and carbon ions over 10 spills for an energy of 180 MeV/u and 276 MeV/u, respectively. For carbon ions, we observe a bunch interval of $171.1 \text{ ns} \pm 2.6 \text{ ns}$ and a minimum bunch width of $15.5 \text{ ns} \pm 1.6 \text{ ns}$. Due to the regular microstructure of the helium beams with lowest energy, we observe a very precise peak width of $33.1 \text{ ns} \pm 0.5 \text{ ns}$. As the energy of the helium ions increases, the peak width gets larger. Also three components seem to arise and become more evident for higher energies. As expected, we observe that the peak interval between bunches decreases for an increasing energy of all beam species.

Time resolution

Fig. 4.28 shows the time spectrum obtained from the time difference between the arrival of the prompt-gamma radiation generated by a thin target at the CeBr₃ detector and the carbon ions at the scintillating fibers. We clearly observe a prompt component with a superimposed gaussian function in red. A

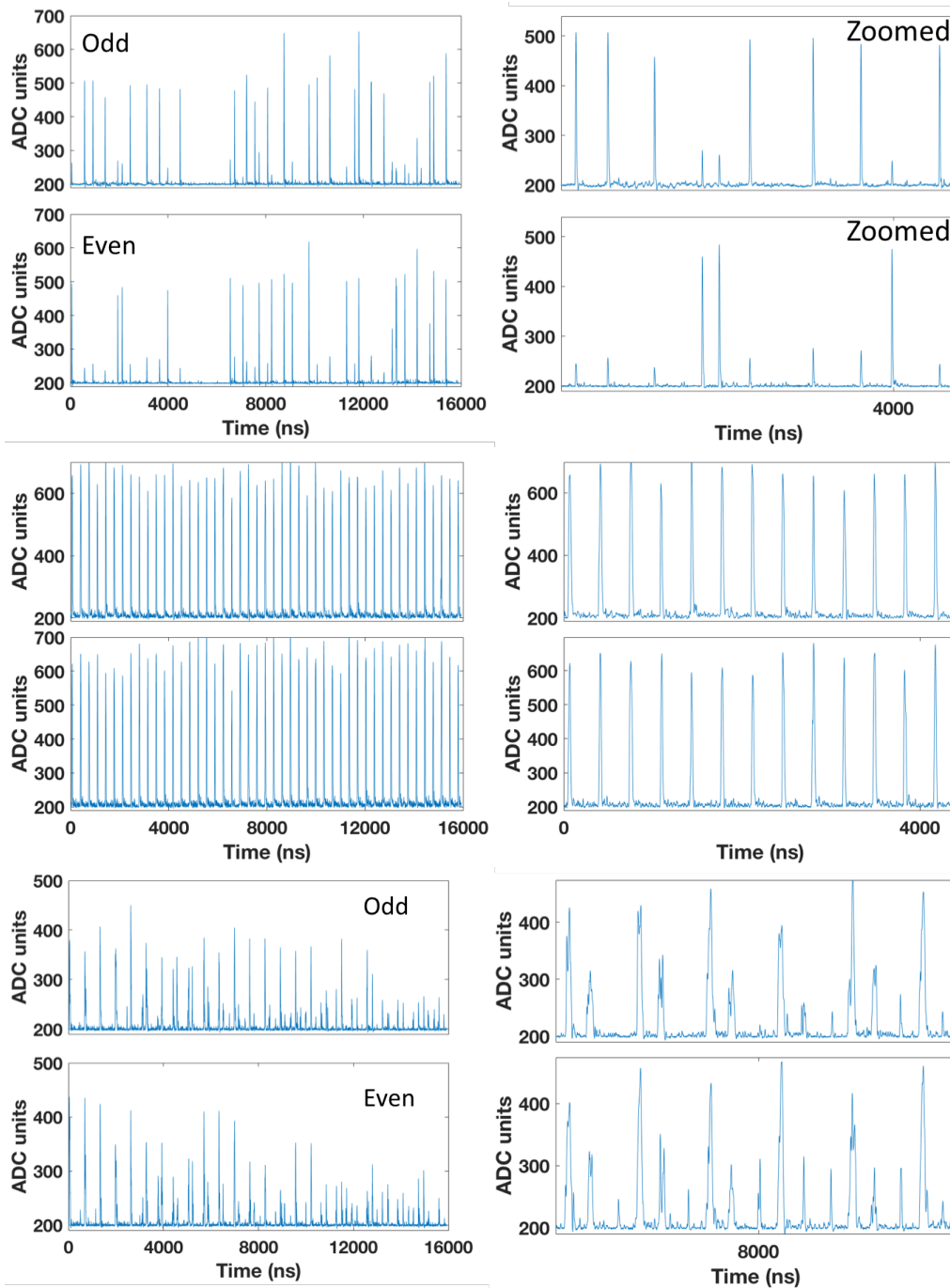


FIGURE 4.24: Time microstructure for carbon (top), helium (middle), and proton (bottom) beams. The beam energies are 276 MeV/u, 146 MeV/u, and 145 MeV/u, respectively. The intensities are 2×10^6 p/s, 2×10^7 p/s, and 8×10^7 p/s, respectively. The trace duration is $16 \mu\text{s}$ and hits in both odd and even fibers are shown. The right plots correspond to a windowed region from the left plot. Cross-talk for carbon ions and multiple hits for protons are clearly visible.

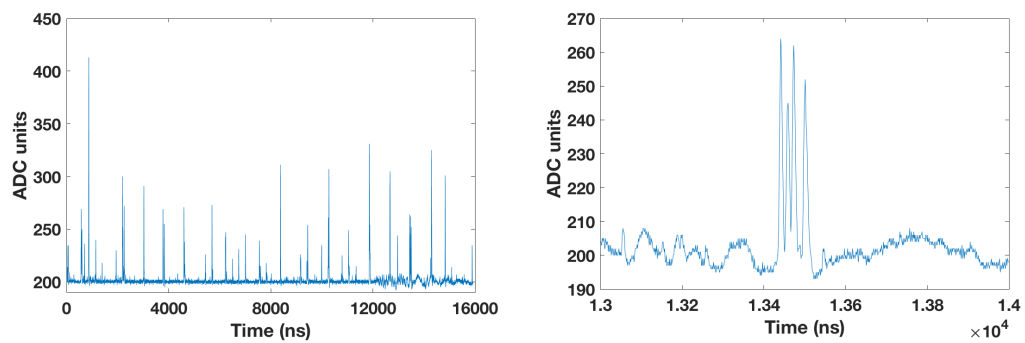


FIGURE 4.25: Left: A $16 \mu\text{s}$ trace from a proton beam with an intensity of 8×10^7 p/s. Right: A zoom over the time interval from $13 \mu\text{s}$ to $14 \mu\text{s}$ shows a multiple hit with four events within 200 ns.

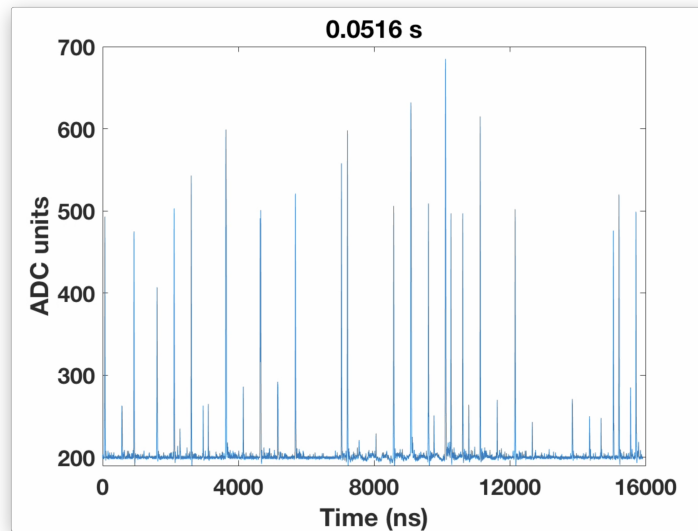


FIGURE 4.26: Animation of the carbon ion spill course. Every frame corresponds to a $16 \mu\text{s}$ trace. The spill lasts approximately 4.85 s. Only the initial and the last part of the spill are displayed. (available online)

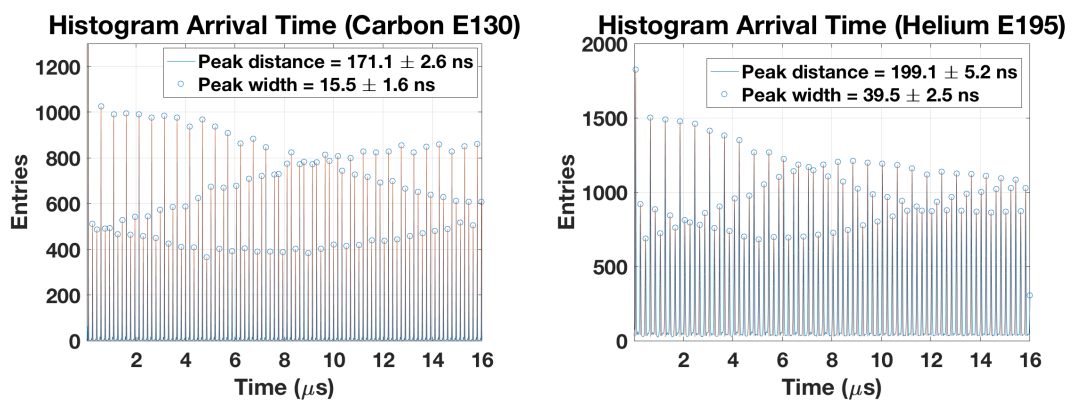


FIGURE 4.27: Bunch width and interval of a carbon beam with 276 MeV/u (left) and a helium beam with 180 MeV/u (right).

	Energy step	E1	E65	E135	E195	E255
^1H	Interval [ns]	352.2 ± 7.1	248.1 ± 4.1	217.1 ± 6.2	199.5 ± 3.6	185.0 ± 4.1
	Width [ns]	73.1 ± 10.4	48.5 ± 4.9	45.5 ± 4.2	44.2 ± 3.0	40.8 ± 3.8
^4He	Interval [ns]	347.7 ± 2.0	246.7 ± 4.0	216.4 ± 3.9	199.1 ± 5.2	185.0 ± 5.1
	Width [ns]	33.1 ± 0.5	38.5 ± 2.4	38.3 ± 2.4	39.5 ± 2.5	41.8 ± 2.5
^{12}C	Interval [ns]	–	192.7 ± 6.8	171.1 ± 2.6	159.1 ± 3.1	149.3 ± 3.5
	Width [ns]	–	26.9 ± 4.6	15.5 ± 1.6	16.8 ± 1.8	19.2 ± 2.1

TABLE 4.5: Bunch width and interval for proton, helium, and carbon beams for five energy steps ranging from 48.1 MeV/u to 221.1 MeV/u, from 50.6 MeV/u to 220.5 MeV/u, and from 88.8 MeV/u to 430.1 MeV/u, respectively.

delayed component from neutron and fragment induced prompt gamma is also observed. A faster component just before the prompt component may result from prompt-gamma induced fragments produced in the nozzle and hitting directly the CeBr_3 detectors. The prompt component demonstrates a system time resolution of approximately 0.8 ns FWHM.

Fig. 4.29 shows the time spectrum obtained from the time difference between the arrival of the carbon ions at the plastic scintillator and at the scintillating fibers. For this measurement the setup has been changed. For the previous measurements only the scintillating fibers were in the beam (in coincidence with the CeBr_3). Here the coincidences are made exclusively between the plastic scintillator and the odd scintillating fibers. The higher the energy the faster the particles and the lower the time elapsed between both detectors. A consistent intrinsic time resolution of 0.7 ns FWHM was obtained for the five energy steps.

Fig. 4.30 shows a slightly different time difference between the odd and the even scintillating fibers and the plastic detector. We observe a degradation of the time resolution for helium (1.56 ns FWHM) and proton (2.64 ns FWHM) beams attributable to an increased energy straggling (not shown).

Energy deposition

Fig. 4.31 shows four spectra of the energy deposited by carbon and helium ions in both plastic scintillators and in the odd and even fibers. The carbon ion distributions present a Gaussian shape as expected from a Vavilov distribution in the Gaussian limit (Leo, 1994). For lighter particles, the distributions resemble a Landau distribution as expected for such particles hitting

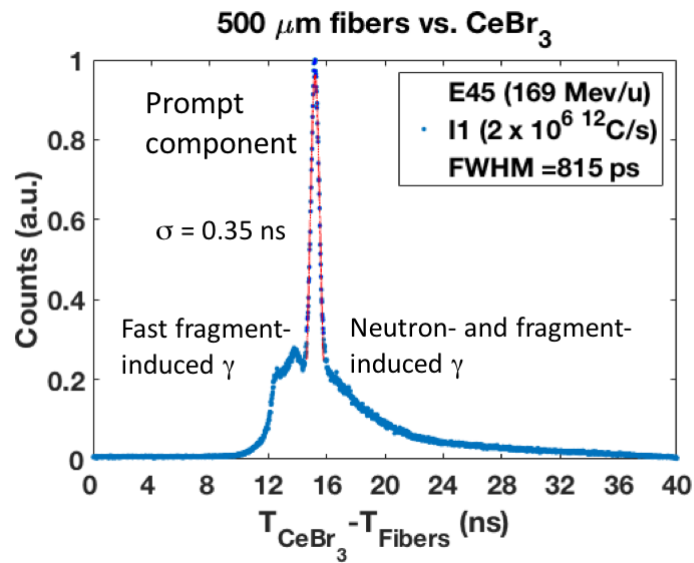


FIGURE 4.28: Time resolution of the PGS system. The time difference between the arrival from prompt-gamma to the CeBr_3 detector and the arrival from carbon ions to the scintillating fibers shows a prompt component (red) with 0.8 ns FWHM. A delayed component resulting from neutron and fragment induced γ -rays is observed and may be removed by TOF cuts. A fast component resulting from fragment induced γ -rays scattered in the nozzle is also visible.

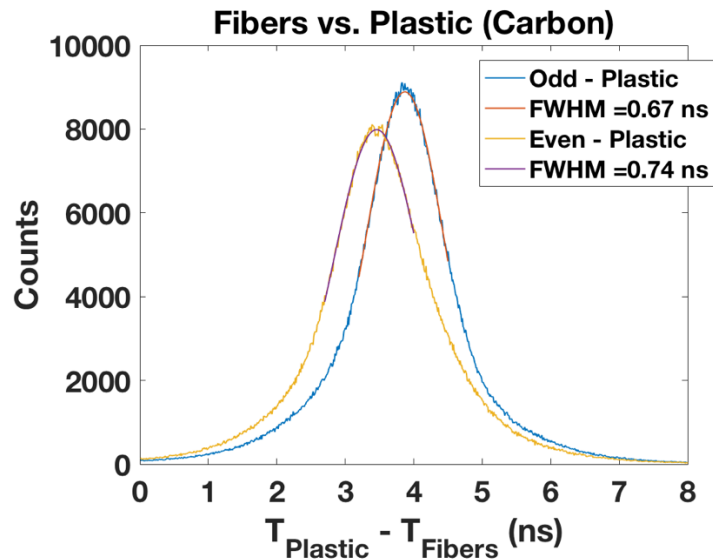


FIGURE 4.29: Intrinsic time resolution determined from the time between the arrival from carbon ions to the plastic detector and to the scintillating fibers. A consistent value of 0.7 ns is observed for five energy steps covering the full energy range. The higher the energy, the faster the particles and the smallest the time elapsed between detectors.

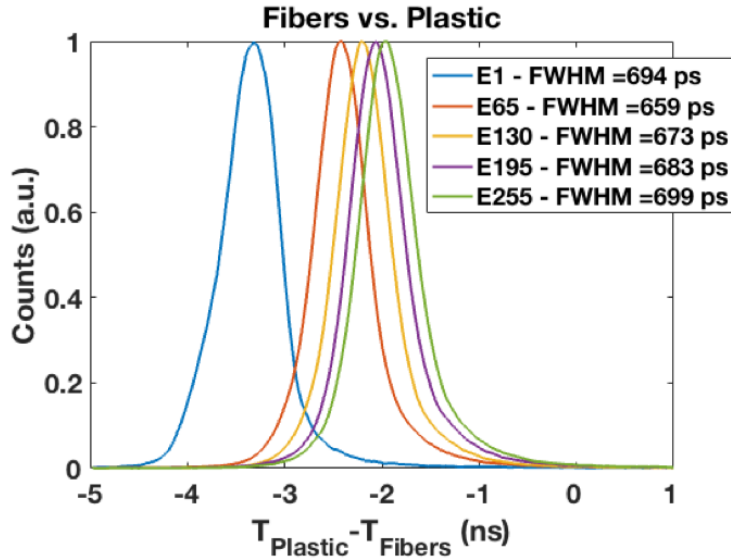


FIGURE 4.30: Intrinsic time resolution for the odd and even scintillating fibers present within the alternating fashion. A consistent value of 0.7 ns is obtained for both fiber bundles.

a thin target. The proton beam distributions resemble the helium ions distributions (not shown).

Fig. 4.32 presents the result from the decomposition of the four components associated to the interaction of the carbon ions with the odd and even fibers. As mentioned before, there is an evident cross-talk between odd and even fibers if irradiated by carbon ions. We can select from the events hitting the odd fibers, the ones that have a higher energy deposition in that fiber and a lower energy deposition in the neighboring fiber. Conversely, we can choose from the events hitting the even fibers, the ones that have a higher energy deposition in that fiber and a lower energy deposition in the neighboring fiber. We observe that 45.6% of the events deposit higher energy in the odd fibers and 46.2% in the even fibers, totaling 91.8% of the total events. In this analysis, the threshold was set at 200 (a.u.).

Efficiency

In order to evaluate the efficiency of the scintillating fibers, we lowered the beam intensity by two means: a) bending the beam up to 1° via magnets; b) collimating the beam with two PMMA blocks separated by a 1 mm spacer. For the determination of very low intensities, we bended the beam gradually and detected the scattered particles in the nozzle with the thicker plastic detector very close to the nozzle. We compared the count rate with the one obtained with the scintillating fibers. Since we clustered the channels from the fibers, the FADC throughput was limited to ≈ 28 kcps. For the first nominal intensity, we obtained a count rate in the plastic detector of ≈ 950 cps.

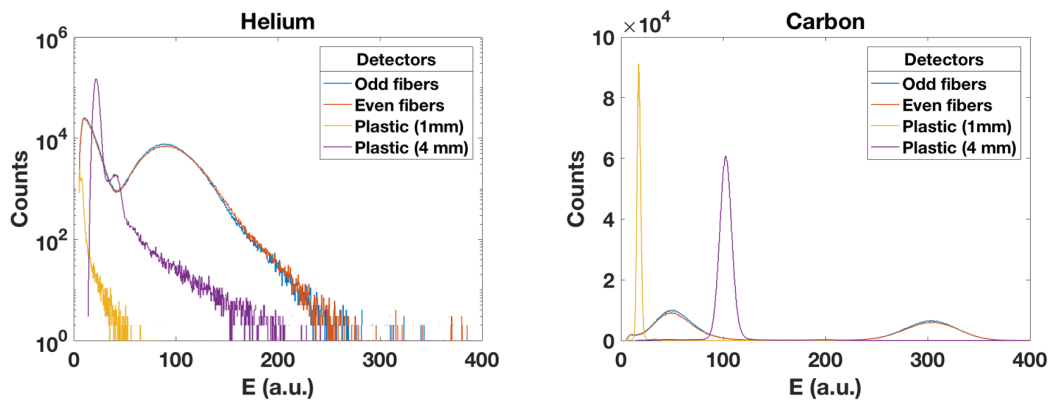


FIGURE 4.31: Right: Energy deposited by carbon (left) and helium (right) beams in the scintillating fibers and in the two plastic scintillators. An expected Gaussian shape for heavier particles is observed. The distributions from lighter particles resemble a Landau distribution as expected for a thin target.

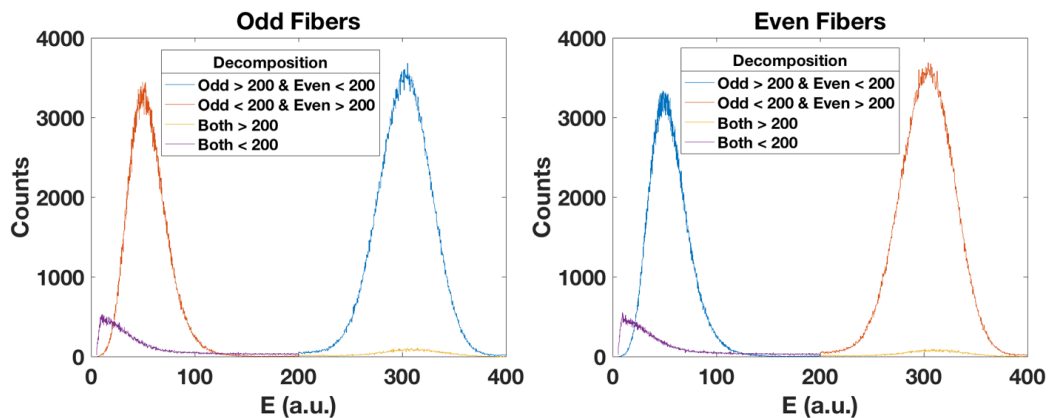


FIGURE 4.32: The energy deposited by carbon ions in the scintillating fibers produces cross-talk in the corresponding neighboring fiber. For the odd fibers (left), we can decompose the events by setting a threshold and performing logic operations. The blue curve corresponds to the valid events. Conversely, for the even fibers (right), the valid events are represented in the red curve.

Run	1	2	3	4	5	6	7	8	9	10	11
BCM [cps]	-	-	-	-	-	29	122	238	356	465	950
CR Factor	-	-	-	-	-	33.3	7.77	3.99	2.67	2.05	1
SciFi [cps]	104	471	741	2.11	11.8k	60k	174k	285k	379k	432k	495k
DT [%]	0	0	0	0	0	54	83	90	92	92	93
CCR [cps]	-	-	-	-	-	60k	257k	501k	749k	978k	2M
ECR [Mcps]	-	-	-	-	-	2.00	1.36	1.14	1.01	0.88	0.50

TABLE 4.6: Measured count rate (CR) in the plastic scintillator bunch monitor (BCM) and in the scintillating fibers (SciFi). Dead time (DT) starts increasing at a CR of 28 kcps in the SciFi. The calculated count rate (CCR) is obtained from the nominal intensity of 2×10^6 p/s divided by the CR factor from the BCM measurements. The extrapolated count rate (ECR) is obtained from the CR factor from the BCM measurements multiplied by the measured CR in the SciFi after dead time correction.

We gradually bended the beam until we had a count rate of ≈ 30 cps. We acquired alternately the events from the plastic scintillator and the scintillating fibers.

In table 4.6, we present the results from the acquisition of carbon ions with an intensity lowered from the nominal intensity $I_1=2 \times 10^6$ p/s down to 100 p/s. Both detectors match at run 6. We obtained a count rate in the scintillating fibers of ≈ 60.5 kcps, already corrected for a dead time of 53.6%, and a count rate of 29 cps in the plastic detector. We finally obtained an extrapolated count rate of 2.002×10^6 p/s which compares well with the nominal intensity of reference. Below those values (run 1–5), the plastic scintillator is not reliable, while above those values (run 7–11), the dead time starts playing an important role and the count rate in the scintillating fibers is not retrievable anymore.

We proceeded with higher intensities in order to evaluate the ability of two 0.5 mm fibers feeding alternate PMTs to cope with a collimated beam with a slit of 1 mm. We acquired traces of 16 μ s and counted the number of particles in each trace. We then increased the intensity of the beams from the intensity step 1 ($I_1=2 \times 10^6$ p/s for carbon ions and $I_1=8 \times 10^7$ p/s for protons) up to the intensity step 8 ($I_8=3 \times 10^7$ p/s for carbon ions and $I_8=1.2 \times 10^9$ p/s for protons). Fig. 4.33 shows the relative number of particles in each trace for the several intensity steps and the estimated intensity. We observe a linear behavior for carbon ions up to the intensity step 7 (2×10^7 p/s) both for odd and even fibers. For protons, there is an increasing underestimation of the true intensity as a result of the pile-up of multiple hits within bunches.

Summary and future perspectives

A small-scale prototype of a hadron beam time tracker for the measurement of the arrival time of single particles in an ion beam has been demonstrated.

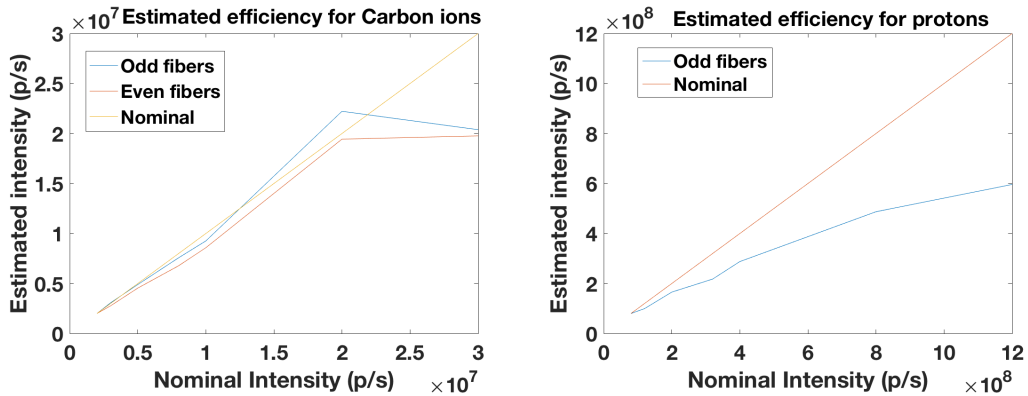


FIGURE 4.33: Estimated efficiency for the detection of carbon ions (left) and protons (right) by the scintillating fibers for an intensity range of 2×10^6 p/s – 3×10^7 p/s and 8×10^7 p/s – 1.2×10^9 p/s, respectively. Results for odd and even fibers are shown for carbon ions as well as the ideal line.

This prototype was able to track single particles within bunches of proton, helium, and carbon ions currently accelerated at the HIT facility. This is of utmost importance for PGI systems relying on the TOF information for range verification. We demonstrated a time resolution for the prompt component of 0.8 ns FWHM. This allows for an efficient rejection of neutron and fragment induced prompt-gamma background. The results from the measurement of the carbon bunch width was in good agreement with previous results (Parodi et al., 2008). However, those results are clearly insufficient if compared with the proton bunch widths in cyclotron-based facilities where the protons are much less spread over the bunch and very well correlated with the cyclotron RF. Despite the absence of fiber cladding, we were able to remove the cross-talk between fibers by evaluating the energy deposited in the alternating fibers. This evaluation may be further used in beam diagnostics, e.g. in mixed beams (Graeff et al., 2018; Mazzucconi et al., 2018), where the carbon beams are used for treatment and the helium beams are used for imaging. Such prototype may also be used for cross-section measurements of carbon ions hitting a thin target. The carbon ions and the fragment (e.g., protons) component may be separated by measuring the energy deposition.

We plan to scale our prototype and build a 20×20 cm² detector to cover the full treatment area and work under active scanning beams. For such an area, we would need 400 scintillating fibers readout by independent detector elements. In order to cope with the maximum intensities available at the HIT facility (2×10^9 p/s) and considering an average separation between bunches of approximately 150 ns, we would need to track 300 single particles per bunch. These particles may be spread over a small or a large area depending on the beam focus. If we consider a lateral spread of 3 cm (3σ), those 300 particles would be spread over 60 scintillating fibers with an average number of events per scintillating fiber and per bunch of ≈ 5 . For carbon ion beams where intensities reach 5×10^7 ions/s and the lateral spread is

smaller (≈ 1 cm), we would need 20 scintillating fibers to cope with approximately 8 particles per bunch and measure an average number of events per scintillating fiber and per bunch below 0.35.

The interference of the prototype with the beam and its radiation hardness remained out of the scope of this paper. However, we plan to measure the water equivalent path length of the crossed material and the effect on beam degradation and test the scintillating fibers against radiation damage over routine clinical workflow conditions.

Finally, a clinical prototype of such scintillating fibers will provide a fundamental input to PGI for the verification of the particle range and dose delivery to the patient.

Acknowledgements

P.M.M. is supported by a research fellowship for postdoctoral researchers from the Alexander von Humboldt Foundation, Bonn, Germany. R.D.B. is supported by the International Max Planck Research School for Quantum Dynamics in Physics, Chemistry and Biology, Heidelberg, Germany. The authors thank the staff of the Heidelberg Ion-Beam Therapy Center (HIT), Heidelberg, Germany, in particular Dr. Stephan Brons and Dipl.-Ing. (FH) Jochen Schreiner for the technical support. The authors also thank the radiation protection department of the DKFZ, in particular Dipl.-Ing. Mechthild Kaemmer, for the support with calibration sources.

4.5 Absolute range verification for ion beams

Title : Prompt Gamma Spectroscopy for absolute range verification at synchrotron based facilities: experimental results from ^1p , ^4He , ^{12}C and ^{16}O beams

Authors : Riccardo Dal Bello, Paulo Magalhaes Martins, Stephan Brons, German Hermann, Thomas Kihm, Michael Seimetz and Joao Seco

Status : Under review

Journal : Physics in Medicine and Biology

Copyright : Ownership of the copyright not transferred to any publisher yet

Contributions : R.D.B. designed and performed the experiments. The last author, J.S., coordinated the project and provided guidance in order to test the detection system in a clinical relevant scenario. The third to fifth authors, S.B., M.S., G.H. and T.K., provided support with the detectors and the electronics used in the experimental setup. This included a FADC module, a remotely controlled moving platform and the beam trigger. R.D.B. conducted the post-processing of the experimental data and he wrote the software to perform the quantitative analysis. The second author, P.M.M., attended and provided support during all the experimental campaigns and he contributed to the interpretation of the results. R.D.B. finalized the data analysis, wrote the software to export the plots included in the article and wrote the article. R.D.B. and the co-authors concluded the studying demonstrating the measurement of the absolute Bragg peak position for ion beams accelerated by a synchrotron, which was the aim of the thesis.

Abstract

The physical range uncertainty limits the exploitation of the full potential of charged particle therapy. In this work we face this issue aiming to measure the absolute Bragg peak position in the target. We investigate ^1p , ^4He , ^{12}C and ^{16}O beams accelerated at the Heidelberg Ion-Beam Therapy Center. The range of the primary particles is measured using the prompt gamma spectroscopy method, which was demonstrated for proton beams accelerated by cyclotrons and is developed here for the first time for heavier ions accelerated by a synchrotron. We develop a detector system that includes (i) a spectroscopic unit based on cerium(III) bromide and bismuth germanium oxide scintillating crystals, (ii) a beam trigger based on an array of scintillating fibers and (iii) a data acquisition system based on a FlashADC. We test the system in two different scenarios. In the first series of experiments we detect and identify $N = 19$ independent spectral lines over a wide gamma energy spectrum for different targets, including also a water target with a titanium insert. In the second series of experiments we introduce a collimator and we relate the spectral information to the range of the primary particles. We demonstrate sub-millimetric precision for the measurement of the ^{12}C Bragg peak position in the experimental setup. We develop a comprehensive statistical analysis and we conclude that range verification with a 2 mm accuracy will be achievable with lateral spot aggregation for each of the ions during a single fraction delivery of $D = 2$ Gy physical dose.

Introduction

The growing interest for charged particle therapy (CPT) is driven by the favorable depth-dose distribution of relativistic light ions in matter. Their energy deposition profile is referred to as Bragg peak and presents its maximum at the end of the range of the primary particles (Bragg et al., 1905). Such characteristic potentially allows the delivery of highly conformal radiation to the tumor while reducing the dose in the surrounding tissue (Amaldi et al., 2005). The number of patients receiving CPT is rapidly growing and it overcame the 200'000 treatments at the end of 2018 (PTCOG, 2018). This includes the clinical practice with ^1p and ^{12}C beams and a pilot project that until 1992 treated over 2'000 patients with ^4He beams at Berkeley. The latter has recently gained new interest and the introduction of therapeutic ^4He beams has been planned at the Heidelberg Ion-Beam Therapy Center (HIT) for the next year (Mein et al., 2019). Moreover, additionally to the previously mentioned ion species, beams of ^{16}O ions are available for experimentation at HIT (Haberer et al., 2004). The multiple ion species have separate rationales for their use, different biological properties, specific nuclear fragmentation processes and unique mixed fields. However, slightly relativistic ^1p , ^4He , ^{12}C and ^{16}O beams share the fact that the primary beam stops in the target and that their availability is limited to synchrotron based facilities. The former property leads to an interest in measuring the Bragg peak position while the

latter calls for the need of developing a device employable at a synchrotron based facility.

Numerous solutions have been proposed to measure the range of the primary ions in vivo. Knopf et al., 2013 reviewed all the techniques and exclusively one of these provides for all the body sites simultaneously a direct signal during CPT combined with an expected millimetric accuracy: prompt gamma imaging (PGI). This technique is based on the production of excited nuclear states through inelastic collisions of the projectiles with the target nuclei. Such states have typical mean life shorter than $\tau < 10^{-11}$ s and can de-excite with isomeric transitions emitting discrete gamma quanta with energy equal to the difference of the nuclear levels (Kozlovsky et al., 2002). The detection of this secondary radiation provides a non-invasive solution to measure the Bragg peak position without extra dose to the patient and without extending the treatment time. Therefore, several efforts have been undertaken to investigate PGI and multiple detection techniques are currently under development (Krimmer et al., 2018). Richter et al., 2016 acquired the first prompt gamma data during proton treatments with passively scattered beams and Xie et al., 2017 investigated it during patient treatments with proton pencil beam scanning. In both cases, the detection aimed at retrieving relative shifts. The recovery of the absolute Bragg peak position for proton beams accelerated by cyclotrons was demonstrated by Verburg et al., 2014. This required the employment of large crystals with spectroscopy capability to measure multiple prompt gamma lines associated with independent de-excitation channels. This technique is referred to as prompt gamma spectroscopy (PGS). Hueso-González et al., 2018 recently presented a full scale prototype dedicated to PGS for proton beams accelerated by cyclotrons. They demonstrated the measurement of absolute millimetric deviations under clinically realistic conditions. In the current work we aim to develop PGS to heavier ion beams accelerated by synchrotrons.

The core of PGS is the capability to detect discrete spectral lines. Therefore, in a previous work we optimized a spectroscopic unit based on a cerium (III) bromide (CeBr_3) scintillating crystal (Dal Bello et al., 2018). The choice of this scintillator was driven by the absence of intrinsic activity and its excellent time and energy resolution (Quarati et al., 2013). The possibility to detect the prompt gamma over its full energy spectrum down to $E_\gamma = 511$ keV is beneficial to include a multitude of independent reactions in the analysis and it was demonstrated during ^1p experiments (Magalhaes Martins et al., 2017) and ^4He irradiation (Dal Bello et al., 2019). Moreover, several new challenges are encountered moving to heavier ions (Pinto et al., 2015). Testa et al., 2010 investigated the time structure of the secondary radiation generated by ^{12}C beams. For low energy pulsed beams there is a strong correlation with the accelerator high-frequency (HF) and the background rejection techniques adopted with ^1p beams can be applied (Verburg et al., 2013b). The correlation with the HF is lost for continuous beams at the high energies required for treatments. In this case the direct detection of the arrival time of the primary ions is necessary. Therefore, we developed a beam trigger based on scintillating fibers that provides minimal interaction with the beam, single

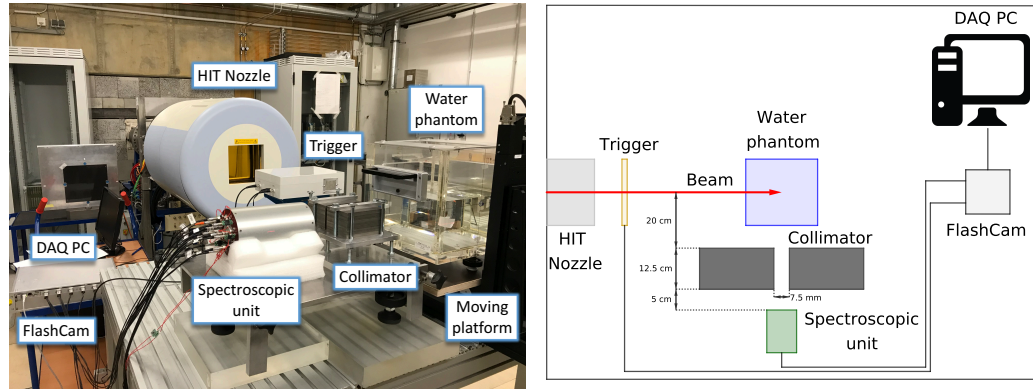


FIGURE 4.34: Experimental setup in the cave at HIT (left) and its schematic not to scale representation with labels indicating the between components (right)

particle measurement at high intensities and which is scalable to the maximum intensities used during treatments (Magalhaes Martins et al., 2019b). Finally, the use of heavier ions is also associated with the production of nuclear fragments and higher neutron yield (Aricò et al., 2019). Such processes increase the noise in the detectors used for PGI and require the development of dedicated background rejection techniques. We take into account all the previous phenomena and aim to measure the absolute Bragg peak position with a precision smaller than the current physical range uncertainties, which can reach and exceed the 10 mm (Paganetti, 2012).

In this work, we investigate for the first time PGS for absolute range verification for ^1p , ^4He , ^{12}C and ^{16}O beams. We adopted the customized spectroscopic unit and beam trigger, we developed dedicated background rejection routines and we extracted features related to the particle range. Finally, we present a method to measure the absolute range in the target and we discuss the requirements to achieve a clinically relevant range control.

Detectors and data acquisition system

We investigated experimentally the applicability of PGS for ion beam therapy in a synchrotron based facility. The current section presents the details of the experimental components.

Spectroscopic unit

The core of the experimental setup was the spectroscopic unit. The primary detector was a cerium bromide (CeBr_3) crystal with a cylindrical shape (diameter $d = 3.81$ cm and length $l = 7.62$ cm) coupled to a R9420-100 PMT (Hamamatsu). It was surrounded by a secondary bismuth germanium oxide (BGO) crystal with a cylindrical shape and a cavity to host the CeBr_3 (thickness $t = 3$ cm, length $l = 11$ cm and inner diameter $d_{\text{in}} = 4.6$ cm). The BGO was sectioned in eight azimuthally-symmetric and optically-separated

segments. Each section was coupled to an independent R1924 PMT (Hamamatsu). This crystal was used as Anti-Coincidence (AC) shield. The experimental performances of the spectroscopic unit in presence of ^4He beams accelerated at a clinical facility have been investigated in a previous dedicated study by Dal Bello et al., 2019. Figure 4.34 (left) shows the experimental setup with the spectroscopic unit at the center, behind the collimator.

Beam trigger

Two separate detectors have been used to measure the arrival time of primary particles in the experimental campaigns: the first was based on a plastic scintillator tile and the second on an array of scintillating fibers.

The plastic scintillator was 0.1 cm thick and covered a $8 \times 8 \text{ cm}^2$ area. The tile was a EJ-200 plastic scintillator. We connected it on one side to a R13089 PMT (Hamamatsu) with a silicone coupling component. The tile was sealed with an aluminum foil to enhance the internal reflection and black tape to make it light tight. The same detector has been adopted also in a previous study (Dal Bello et al., 2019). This is further referred to as the *EJ-200 detector*.

The second beam trigger was based on a set of scintillating fibers with a square cross section of side length $500 \mu\text{m}$. We designed dedicated supports to obtain a single layer of scintillating fibers (BCF-12, Saint Gobain Crystals). The total active area was $3 \times 3 \text{ cm}^2$. The fibers were connected on one side to two independent R647 PMT with E849-35 socket assembly (Hamamatsu) in an alternating fashion. The detector included an housing for light shielding equipped with an entrance and exit window for the beam (double aluminized mylar summing up to a total thickness $< 10 \mu\text{m}$). This detector was designed to be operated at higher intensities compared to the EJ-200 and its experimental performances in presence of clinical ion beams have been investigated in a previous dedicated study by Magalhaes Martins et al., 2019b. This is further referred to as the *SciFi detector*. Figure 4.34 (left) shows the SciFi detector at the front of the experimental setup, between the nozzle and the water phantom.

Electronics

We used one single FlashCam FADC module for the digitalization of the detector signals (Werner et al., 2017). Such system was originally developed for the Cerenkov Telescope Array and is highly flexible and promptly adaptable to PGS experiments. Promising results with this electronics have been obtained by Dal Bello et al., 2019. Three fundamental properties made the FlashCam modules especially suitable for the current work: the flexible Ethernet-based interface (10 Gbit) with high data-rate capability for continuous data streaming, multi-channel acquisition mode and the continuous high-speed digitization (12-bit, 250 MS/s FADC system) with on-board FPGA-based digital signal processing and triggering. Figure 4.34 (left) shows the FlashCam module at the side of the experimental setup.

The data acquisition system (DAQ) was operated with up to $N = 17$ independent channels and triggered by energy depositions in the CeBr_3 having $E \geq 500$ keV. Every channel acquired event-by-event single traces $\Delta t = 240$ ns long. We chose the sampling intervals depending on the detector properties: $\delta t = 4$ ns for the CeBr_3 and each of the eight BGO sections, $\delta t = 1$ ns for the EJ-200 and each of the two PMT in the SciFi detector. We used the DAQ to acquire either the signals from the EJ-200 or the SciFi, i.e. we did not operate the two detectors simultaneously. The resulting data stream was approximately 2 kB/event, which converts to data sets of about 2 GB for a typical run with 10^6 raw events detected by the spectroscopic unit. In the collimated experiments we observed count rates up to $2 \cdot 10^3$ cps without dead time. In the uncollimated experiments we reached up to $4 \cdot 10^4$ cps with dead time below 10%.

We pre-amplified the BGO signals as described by Dal Bello et al., 2019. The high-voltage of the PMT coupled to the CeBr_3 was tuned to cover the $0.5 \div 10$ MeV gamma spectrum within the FADC dynamic range. We also tuned the gain of the two PMT in the SciFi detector to obtain the same signal amplitude at the two channels with a ^{90}Sr source during offline calibration runs.

Data analysis and modelling

The experimental data required an extensive analysis to extract the correlation between the prompt gamma spectra and the particles range. The current section presents the offline processes adopted to suppress the background and derive spectral features.

Response function spectroscopic unit

We performed a detailed characterization of the spectroscopic unit with the aim of improving its performance during the offline data analysis. We modelled the interactions of the high energy gamma radiation in the detectors and computed the response matrix of the system. The method was based on the results presented by Guttormsen et al., 1996. We performed Monte Carlo (MC) radiation transport simulations to generate the response matrix. We used FLUKA, which is a general purpose MC software with applications in multiple fields (Ferrari et al., 2005) including medical applications (Böhlen et al., 2014). We adopted the FLUKA version 2011.2x with the default settings PRECISION.

We generated the response matrix of the system for incoming gamma with energy up to $E_\gamma = 10$ MeV. The pure energy deposition in the CeBr_3 (E_{dep}) was converted into the measured energy deposition (E_{mes}) by applying an energy spread according to the CeBr_3 resolution parameterized by Roemer et al., 2015. Then we calculated the probability $P(E_{\text{mes}}, E_0)$ that such event had been generated by an incoming gamma ray with energy E_0 . The matrix $P(E_{\text{mes}}, E_0)$ fully described the degradation of the prompt gamma

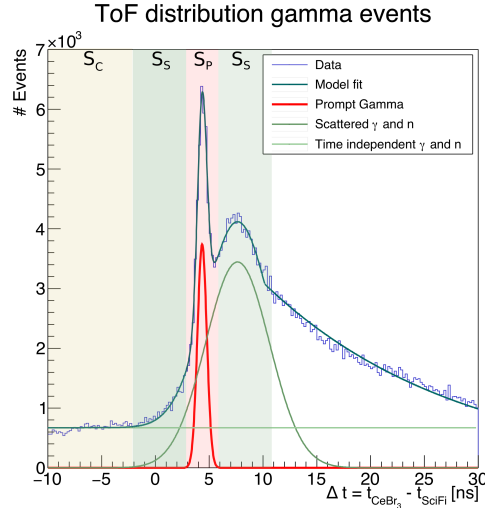


FIGURE 4.35: Time of flight spectrum between the signals in the CeBr₃ and the SciFi detector. The data was acquired in presence of the ¹²C beam during the collimated experiments. The different components are added to obtain the total model plotted in the dark green solid line, which is fitted to the data presented as histogram. The highlighted areas represent the regions where the distributions S_P , S_S and S_C were sampled.

spectrum due to the detection using the spectroscopic unit. Vertical projections of the matrix represented the response to mono-energetic radiation. Horizontal projections reported the probability distribution for the generation of a given measured energy.

Background rejection with detectors

We processed the data off-line using ROOT (Brun et al., 1997). We performed a first background rejection based on the data acquired by the primary and secondary detectors.

The spectroscopic unit was operated in anti-coincidence. We calibrated the energy deposition in the AC shield during a dedicated run with a ¹³⁷Cs source. Only in this case the DAQ was triggered by energy deposition in the BGO. We set the threshold for the anti-coincidence rejection at $E_\gamma = 50$ keV. When one of the BGO sections recorded an event above this threshold, the corresponding event in the CeBr₃ was a candidate to be discarded. The event was eventually removed if the two energy depositions happened within the anti-coincidence time window ($\Delta t = 25$ ns).

The beam trigger data was used to define a Time-of-Flight (ToF) window. We considered only the events that fell within the energy deposition cuts for the beam trigger. The cuts were defined on the base of a Gaussian fit of the energy deposition for the heavy projectiles (¹²C and ¹⁶O) and a Landau fit for the light ones (¹p and ⁴He). Simultaneous ($\Delta t < 5$ ns) hits were discarded. Then, we computed the time difference between the events in the CeBr₃ and the EJ-200 or the SciFi detector. We set a ToF window of $\Delta t_{ToF} = 3$ ns for

the experiments with the collimator and $\Delta t_{\text{ToF}} = 6$ ns for the ones without. We accepted the events in the CeBr₃ within these time windows to define the prompt gamma energy spectrum S_P . The events outside the cuts were also stored for further processing. In particular, we defined two time windows (each $\Delta t_S = 5$ ns) to sample the energy spectrum of the scattered radiation S_S before and after the prompt gamma peak. We also defined a wide time window ($\Delta t_C = 45$ ns) before the previous ToF cuts to sample the energy spectrum S_C of the time independent radiation. A graphic representation of the ToF regions where S_P , S_S and S_C were sampled is presented in Figure 4.35.

Finally, we performed a first calibration of the energy deposition in the CeBr₃ based on the ¹³⁷Cs source. We selected the events acquired during beam-on conditions, but outside the ToF cuts. We fitted the $E_\gamma = 0.662$ keV peak and performed a linear calibration of the spectrum. Non-linearity effects were not taken into account at this stage.

Background rejection with models

We further improved the background rejection with dedicated models.

First, we modelled the ToF spectra. The identification of its different components during ion irradiation was investigated by Testa et al., 2010. We based our modelling on this previous study and we defined the following ToF distributions: $f_P(t)$ as the prompt gamma events; $f_S(t)$ as the scattered gamma or the gamma produced in (n, γ) reactions; $f_A(t)$ as the events associated with activation having a characteristic decay time shorter than the time between bunches and $f_C(t)$ as the time independent component, i.e. generated by activation with decay time longer than the time between bunches. The total ToF spectrum was then parametrized by:

$$f_{\text{ToF}}(t) = f_P(t) + f_S(t) + f_A(t) + f_C(t) \quad (4.8)$$

where $f_P(t) = \mathcal{N}(\mu_P, \sigma_P)$ and $f_S(t) = \mathcal{N}(\mu_S, \sigma_S)$ were modelled by Gaussian functions, $f_A(t) = \theta(t - \mu_S - \sigma_S) \cdot e^{-\tau_A \cdot t}$ by an exponential function and $f_C(t)$ by a constant. We set the conditions: $\mu_P < \mu_S$ and $\sigma_P < \sigma_S$. In a following step, we fitted the ToF spectra with (4.8) and defined the following quantities: the correction factor for the prompt gamma ToF cut

$$k_P = \left(\int_{\mu_P - 0.5 \cdot \Delta t_{\text{ToF}}}^{\mu_P + 0.5 \cdot \Delta t_{\text{ToF}}} f_P(t) \cdot dt \right) \cdot \left(\int_{-\infty}^{+\infty} f_P(t) \cdot dt \right)^{-1} \quad (4.9)$$

and the correction factor for the scattered or (n, γ) events in the ToF cut

$$k_S = \left(\int_{\mu_P - 0.5 \cdot \Delta t_{\text{ToF}}}^{\mu_P + 0.5 \cdot \Delta t_{\text{ToF}}} f_S(t) \cdot dt \right) \cdot \left(\int_{\mu_P - 0.5 \cdot \Delta t_{\text{ToF}} - \Delta t_S}^{\mu_P - 0.5 \cdot \Delta t_{\text{ToF}}} f_S(t) \cdot dt + \int_{\mu_P + 0.5 \cdot \Delta t_{\text{ToF}}}^{\mu_P + 0.5 \cdot \Delta t_{\text{ToF}} + \Delta t_S} f_S(t) \cdot dt \right)^{-1} \quad (4.10)$$

This model and its parameters were adopted to further process the experimental data. We scaled the spectrum S_C once by the factor $2 \cdot \Delta t_S / \Delta t_C$ and once by $\Delta t_{\text{ToF}} / \Delta t_C$ to subtract it from S_S and S_P , respectively, obtaining $S_{S,\text{noC}}$ and $S_{P,\text{noC}}$. We scaled $S_{S,\text{noC}}$ by the factor k_S calculated in (4.10) and

subtracted it from $S_{P,\text{noC}}$. Finally, we scaled this result by the factor k_P calculated in (4.9). The component $f_A(t)$ was neglected as its contribution was negligible in the ToF cut for prompt gamma.

Then, we employed the response function calculated in section "Response function spectroscopic unit". We used the matrix $P(E_{\text{mes}}, E_0)$ to unfold the experimental data according to the method described by Guttormsen et al., 1996. Such method has also been successfully applied in a previous prompt gamma study by Vanstalle et al., 2017.

Finally, we smoothed the unfolded spectra with a Gaussian filter having a width proportional to the CeBr_3 resolution tabulated by Roemer et al., 2015. During this process we also corrected for non-linearity effects in the energy calibration. To do so, we used the known position of the high energy spectral line and refined the first energy calibration performed with the ^{137}Cs source. Such fine tuning contributed $< 5\%$ to the overall calibration.

Experimental campaigns

Several experimental campaigns have been performed. The experiments shared the same detectors, data acquisition system and post-processing routines. The experiment-specific features are presented in the current section.

Ion beam characteristics

The experiments were conducted at the Heidelberg Ion-Beam Therapy Center (HIT), Heidelberg, Germany (Haberer et al., 2004). We delivered ^1p , ^4He , ^{12}C and ^{16}O beams to the experimental cave. The active feedback system was activated to guarantee the stability of the parameters and we adopted beam energies and intensities available in the therapy control system (TCS)⁸. The nominal beam intensities varied from a minimum of $5 \cdot 10^6 \text{ ions} \cdot \text{s}^{-1}$ for ^{16}O beams to a maximum of $8 \cdot 10^7 \text{ ions} \cdot \text{s}^{-1}$ for ^1p beams. During all the experimental campaigns the beam was delivered at the isocenter at a fixed energy for each run. Moreover, the nominal beam intensity refers to one during beam-on condition and the ratio spill to inter-spill time was approximately 1 : 1.

Targets

We used four different targets during the experiments:

1. The *PMMA target*. It consisted of four Polymethyl-methacrylate blocks of size $25 \times 25 \times 5 \text{ cm}^3$. We aligned the blocks to obtain a thickness of $l = 20 \text{ cm}$ of PMMA in the beam direction.
2. The *Water phantom*. This target can be seen at the center of the experimental setup in Figure 4.34. The phantom was the MP3-P water tank

⁸Siemens Healthcare GmbH, Erlangen, Germany

produced by PTW⁹. We filled it with approximately $V = 15$ l of double distilled water and we oriented it with the thin ($t = 5$ mm) beam entrance window facing the nozzle. The water phantom was placed on a moving platform, which allowed movements in two directions with a step size of $\Delta l = 10$ μm .

3. The *Water target*. It consisted of five flasks filled with double distilled water and aligned to the beam direction. The total water thickness traversed by the beam was $l = 16$ cm, while the total thickness of the polystyrene flasks walls was $l = 0.9$ cm.
4. The *Water+Ti target*. This was obtained placing a titanium slab of thickness $l = 0.6$ cm between the third and the fourth flask of the water target.

The phantom (ii) had an internal rail for precise positioning of an ionization chamber support. We customized the support to hold a Gafchromic EBT3 film¹⁰, which we used to verify the range of the primary particles in the water phantom.

Uncollimated experiment: reactions identification

The first set of experiments aimed to identify the nuclear de-excitation channels observable with our system. Therefore, we did not introduce any collimator in the experimental setup and we measured the prompt gamma emission over the full target aiming to maximize the statistics. The experimental setup was analogous to the one used in Dal Bello et al., 2019. The spectroscopic unit was placed at $d = 10$ cm from the beam axis and we acquired approximately $N = 2 \cdot 10^7$ raw events in the spectroscopic unit for each run. We used the EJ-200 detector as beam trigger. The irradiated targets and the corresponding properties of the ion beams are reported in Table 4.7. We post-processed the data according to the methods presented in section "Data analysis and modelling". The final results, i.e. the background-free spectra, were used to identify the discrete prompt gamma lines generated during the irradiation. Moreover, we fitted the width of the spectral lines in the water target experiment and we quantified the relation between their FWHM and the mass of the projectile. The theoretical derivation of the functional form used in the fitting is developed in the dedicated appendix section A.

Collimated experiment: Bragg peak position

The second set of experiments aimed to correlate the intensity of the spectral lines identified in the uncollimated experiments to the position of the Bragg peak. Therefore, a tungsten slit collimator was introduced in the setup, as shown in Figure 4.34. The collimator was $t = 12.5$ cm thick, it had a vertical

⁹Physikalisch-Technische Werkstätten GmbH, Freiburg, Germany

¹⁰Ashland Inc., Ashland, U.S.

Target	Beam properties			
Water phantom (collimated experiments)	Ion	E [MeV/u]	N_0 / position	# positions
	^1p	108.88	$9.6 \cdot 10^{10}$	2
	^4He	109.97	$3 \cdot 10^{10}$	2
	^{12}C	204.27	$8 \cdot 10^9$	20
	^{16}O	241.0	$5 \cdot 10^9$	2
PMMA target (un-collimated experiments)	Ion	E [MeV/u]	N_0	
	^1p	148.21	$6 \cdot 10^{10}$	
	^4He	149.02	$1.5 \cdot 10^{10}$	
	^{12}C	281.57	$3.4 \cdot 10^9$	
	^{16}O	-	-	
Water target (un-collimated experiments)	Ion	E [MeV/u]	N_0	
	^1p	148.21	$8.6 \cdot 10^{10}$	
	^4He	149.02	$1.4 \cdot 10^{10}$	
	^{12}C	281.57	$5 \cdot 10^9$	
	^{16}O	333.91	$1.2 \cdot 10^9$	
Water+Ti target (un-collimated experiments)	Ion	E [MeV/u]	N_0	
	^1p	148.21	$7.6 \cdot 10^{10}$	
	^4He	149.02	$1.2 \cdot 10^{10}$	
	^{12}C	281.57	$1 \cdot 10^{10}$	
	^{16}O	333.91	$1.9 \cdot 10^9$	

TABLE 4.7: Breakdown of the experiments conducted at HIT. The number of ions irradiated, their type and energy associated to each experimental setup and target are reported. The blank entries correspond to experiments that were not performed.

opening of $s = 7.5$ mm and it was placed at $d = 20$ cm from the beamline. We aligned the principal axis of the spectroscopic unit with the center of the slit collimator and we positioned it with the frontal face of the CeBr₃ at $d = 40$ cm from the beamline. We used the SciFi detector as beam trigger. We selected the same energy step in the TCS for the four ions in order to generate the Bragg peak always at the same depth in the water phantom, namely at $z = 87$ mm from the beam entrance window, which we verified with the Gafchromic EBT3 films. We operated the moving platform to vary the relative longitudinal position z between the water phantom and the spectroscopic unit and therefore measure the prompt gamma radiation at different depths in the phantom. For each of the ¹p, ⁴He and ¹⁶O beams we acquired one data set before the Bragg peak ($z = 80$ mm) and one after it ($z = 105$ mm). For the ¹²C beam we acquired $N = 20$ positions along the phantom from $z = 25$ mm to $z = 120$ mm with a spacing of $\Delta z = 5$ mm. For every data set we acquired approximately $N = 10^6$ raw events in the spectroscopic unit. The summary of the beam characteristics is reported in Table 4.7. We post-processed the data according to the methods presented in section "Data analysis and modelling". A detailed data analysis was conducted for the collimated experiments.

First, we compared the ToF spectra between the CeBr₃ and the SciFi detector before ($z = 80$ mm) and after ($z = 105$ mm) the Bragg peak. For all the four ions we considered events with energy deposition in the CeBr₃ between $E_\gamma \geq 0.6$ MeV and $E_\gamma \leq 6.8$ MeV. We identified and we fitted the widths of the primary peaks in the ToF distributions for $z = 80$ mm.

Then, we compared the background-free energy spectra detected by the spectroscopic unit before ($z = 80$ mm) and after ($z = 105$ mm) the Bragg peak. We applied a smoothing proportional to the intrinsic energy resolution of the CeBr₃ (Roemer et al., 2015) to suppress the high-frequency noise. For the ¹²C or ¹⁶O beams we analyzed both the prompt gamma emission of the target and the projectile nuclei. In particular, for the ¹²C projectile we analyzed the Doppler shift of the $E_\gamma = 4.4$ MeV line and for the ¹⁶O of the $E_\gamma = 6.1$ MeV line. The theoretical derivation of the Doppler shifts at $z = 80$ mm is presented in the dedicated appendix section A.

Finally, we analyzed the evolution of the intensity of the spectral lines with respect to the Bragg peak position in presence of the ¹²C beam. At every z_i position of the water phantom, we integrated the counts of the discrete peaks over the energy interval $E_0 \pm 3 \cdot \sigma_0$. E_0 was the nominal energy of the discrete peak and σ_0 was the nominal peak width calculated from the CeBr₃ intrinsic energy resolution. We also measured the full prompt gamma emission integrated from $E_\gamma = 0.6$ MeV to $E_\gamma = 6.8$ MeV. The number of events within the integration window was used to calculate the uncertainties according to the Poisson statistics ($\sigma_I = \sqrt{N_\gamma}$). Then, we normalized the counts by the number of irradiated ¹²C ions and we applied the corresponding correction factors to take into account the cuts in the trigger and in the spectroscopic unit, obtaining $I_j(z_i)$ at every position i and for each gamma line j . To better visualize the evolution of the intensities with the position in the water phantom we superimposed the data with a smoothed curve. Such curve

was obtained with the dedicated function `SmoothLowess` in the `TGraphSmooth` class of ROOT (Brun et al., 1997). We used a smoothing factor $f = 1/5$ and we also calculated the standard deviation of the smoothed values from the data points, which we then plotted as a band about the smoothed curve. We concluded the analysis by computing the ratio of the intensities of five pairs of independent spectral lines at every z_i and propagating the statistic uncertainties. The ratios of the intensities $R_{j,k}(z_i) = I_j(z_i)/I_k(z_i)$ were parametrized with a third degree polynomial function in the neighborhood of the Bragg peak.

Results

The results of this study include the performances of the post processing routines and the extraction of spectral features, eventually correlating the prompt gamma yield to the range of the ions in the target. The current section presents the results from the experimental campaigns.

Response function spectroscopic unit

The response function of the spectroscopic unit is presented in Figure 4.36. The matrix maps the probability of obtaining a specific energy deposition in the spectroscopic unit operated in anti-coincidence given the energy of the incoming gamma radiation. The insert in Figure 4.36 shows the Monte Carlo simulated energy spectrum obtained with an incoming $E_\gamma = 6.1$ MeV gamma. It can be observed that the detection of the photo peak is promoted with respect to the background components. The ratio between the events in the photo peak and the ones in the single escape peak was 2.4, while the amplitude of the Compton continuum component was about a factor 30 smaller than the photo peak. The matrix generated with Monte Carlo and presented in Figure 4.36 was used in the following steps to improve the background rejection.

Background rejection

Time-of-Flight model

An example of a ToF spectrum and the corresponding fit of the model described by equation (4.8) is shown in Figure 4.35. The data presented was obtained in the collimated experiments in presence of ^{12}C beams. It can be seen how the $f_P(t)$ and the $f_S(t)$ components can be clearly separated with the time resolution of the system. In this specific case, the time separation was $\Delta t_{P,S} = \mu_S - \mu_P = 3.3$ ns. The separation of the primary and the scattered prompt gamma was critical to achieve a robust background rejection. In Figure 4.35 we observed a factor $\times 6.4$ more events in the $f_S(t)$ peak compared to the $f_P(t)$ peak. A significant amount of such events was present also within the ToF cuts for the primary prompt gamma. These events were subtracted according to the method presented in section "Background rejection

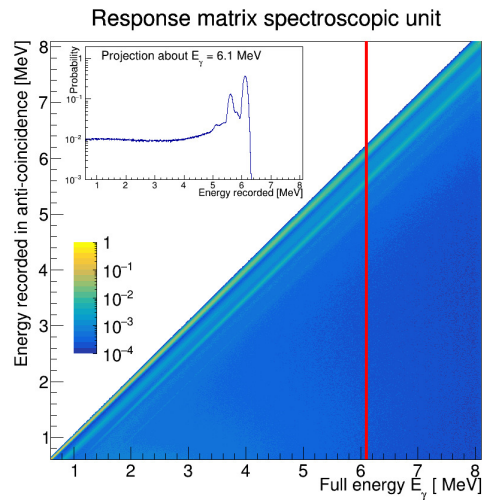


FIGURE 4.36: Response function matrix for the spectroscopic unit. The logarithmic color scale reports the probability to obtain the corresponding energy deposition. The vertical line indicates the response to a monoenergetic photon beam of $E_\gamma = 6.1$ MeV. The insert shows the simulation of its corresponding energy spectrum.

with models". The events in the time independent component $f_C(t)$ had a smaller contribution within the ToF cuts; nonetheless, we processed and subtracted them. On the other hand, the fast decaying events $f_A(t)$ had a negligible contribution to the prompt gamma peak. Therefore, we fitted their ToF distribution but we did not process such events further. A similar behaviour was observed also in the other data sets with different target and in presence of distinct ion beams. It should be noticed that in the uncollimated experiments and in presence of lighter ion beams the width of the $f_P(t)$ distribution increased. The quantitative analysis of such effect is presented in a following paragraph.

Full background rejection

An example of all the progressive steps undertaken to obtain the background-free spectra is shown in Figure 4.37. The raw data without any cut was omitted. It can be observed how the background component is progressively subtracted from the data until obtaining a spectrum mainly composed by the discrete lines. To analyze the contribution of each step, we assumed as the 100% reference the entries in the spectra after the ToF window. We observed that by applying the anti-coincidence detection with the BGO the number of events accepted decreased to 45.5%. The application of the ToF model improves the signal to noise ratio especially at the low energy component of the spectrum and it was critical to completely suppress the hydrogen neutron capture line. As a matter of fact, a local minimum was observed at $E_\gamma = 2.2$ MeV in Figure 4.37 after the ToF model. The fraction of events left after this step

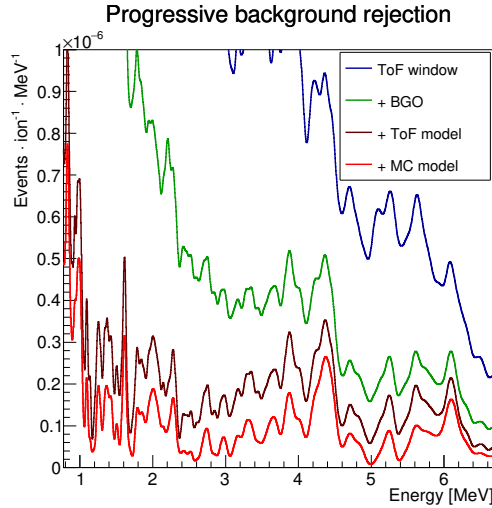


FIGURE 4.37: Progressive steps in background rejection. The solid lines show the obtained spectra after the cumulative introduction of each step in the post processing. The data was acquired in presence of the ^{12}C beam during the collimated experiments. The collimator slit was aligned to the Bragg peak location in the water phantom.

was 12.7%. Finally, the unfolding of the spectrum further removes the detector contributions such as the Compton continuum and the escape peaks. The background-free spectrum contains 8.3% of the initial events. Analogous fractions of removed events were observed for other beam species in the steps introducing the anti-coincidence detection and the unfolding of the spectrum. The number of events removed by the ToF model depended on the beam type and increased with increasing mass of the projectile.

Reactions identification

The background-free spectra acquired during the uncollimated experiments are presented in Figure 4.38. We identified $N = 19$ independent spectral lines in the three targets irradiated. The complete list of the reactions observed for every beam species are reported in Table 4.8.

The quantitative analysis of the evolution of the width of the spectral lines for the water target with increasing mass of the projectile is shown in Figure 4.39. We selected the most and the least energetic prompt gamma listed in Table 4.8. It can be observed how the model (4.20) derived in Appendix A correctly reproduces the experimental data. We observed positive deviations of the FWHM with respect to the intrinsic CeBr_3 resolution reported by Roemer et al., 2015. The minimum deviation was observed in presence of ^1p beams for the $E_\gamma = 0.718$ MeV line, namely a factor $\times 1.22$ wider. The maximum deviation was observed in presence of ^{16}O beams for the $E_\gamma = 6.1$ MeV line, namely a factor $\times 2.97$ wider. The average increase of the FWHM was $\times 1.51$ for the $E_\gamma = 0.718$ MeV line and $\times 2.55$ for the $E_\gamma = 6.1$ MeV line. It should be reminded that the FWHM values in Roemer et al., 2015 have been

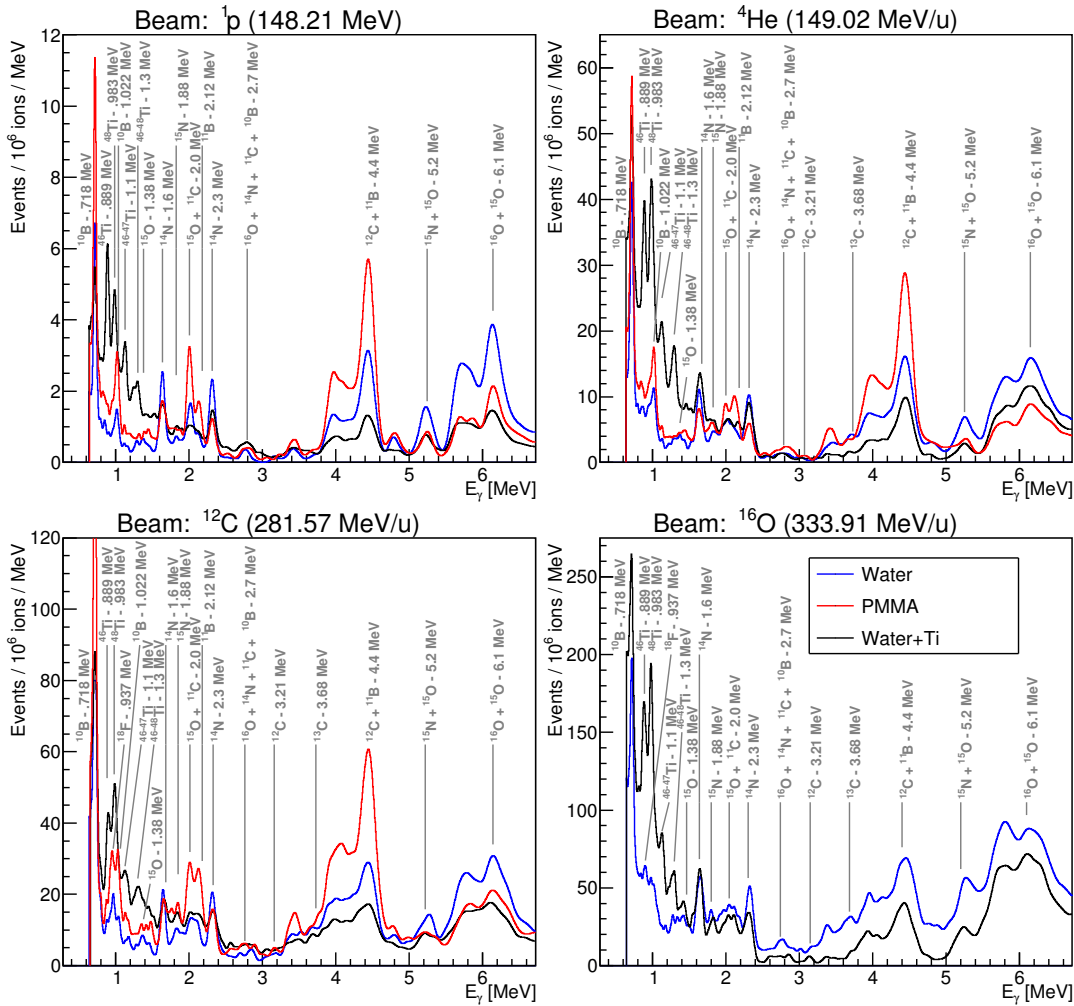


FIGURE 4.38: Background-free spectra and identification of the reaction channels for the uncollimated experiments. The vertical lines indicate the position of the identified peaks. The labels report the nominal energy of the gamma line and the nuclei undergoing the de-excitation.

calculated with negligible Doppler broadening, i.e. using sources or low energetic ^1p beams.

ToF spectra and Bragg peak position

The collimated experiments presented different features for the data sets acquired before and after the Bragg peak position. Figure 4.40 shows the ToF spectra between the CeBr₃ and the SciFi detector signals. For all the four ion beam species we observed a clear difference between $z = 80$ mm and $z = 105$ mm. In particular, for the ^1p and ^4He beams, the events in the prompt gamma peak were observable predominantly in the data acquired upstream the Bragg peak and they were comparable with the background downstream to it. On the other hand, for the ^{12}C and ^{16}O beams, such events were observable in both the positions with different intensities. In this case

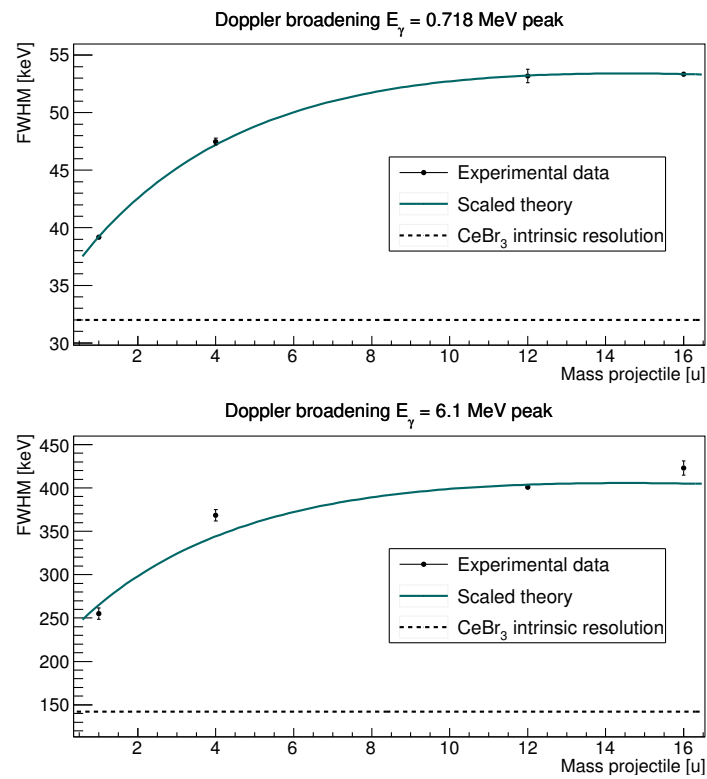


FIGURE 4.39: Evolution of the spectral lines FWHM with increasing projectile mass. The bullets report the experimental data with the water target from the uncollimated experiments. The solid line was calculated from equation (4.20) scaling κ . The dashed line is the nominal CeBr₃ resolution calculated according to Roemer et al., 2015.

E_γ [MeV]	Target nuclei	De-excitation reactions	Reactions induced by:			
			^1_0p	^4_2He	$^{12}_6\text{C}$	$^{16}_8\text{O}$
6.1	$^{16}_8\text{O}$	$^{16}_8\text{O}^*_{6.13} \rightarrow ^{16}_8\text{O}_{g.s.}$	✓	✓	✓	✓
	$^{16}_8\text{O}$	$^{15}_7\text{O}^*_{6.18} \rightarrow ^{15}_7\text{O}_{g.s.}$				
	$^{16}_8\text{O}$	$^{15}_7\text{O}^*_{5.18} \rightarrow ^{15}_7\text{O}_{g.s.}$				
5.2	$^{16}_8\text{O}$	$^{15}_7\text{O}^*_{5.24} \rightarrow ^{15}_7\text{O}_{g.s.}$	✓	✓	✓	✓
	$^{16}_8\text{O}$	$^{15}_7\text{N}^*_{5.27} \rightarrow ^{15}_7\text{N}_{g.s.}$				
	$^{16}_8\text{O}$	$^{15}_7\text{N}^*_{5.30} \rightarrow ^{15}_7\text{N}_{g.s.}$				
4.4	$^{16}_8\text{O}$	$^{12}_6\text{C}^*_{4.44} \rightarrow ^{12}_6\text{C}_{g.s.}$				
	$^{16}_8\text{O}$	$^{11}_5\text{B}^*_{4.45} \rightarrow ^{11}_5\text{B}_{g.s.}$	✓	✓	✓	✓
	$^{12}_6\text{C}$	$^{12}_6\text{C}^*_{4.44} \rightarrow ^{12}_6\text{C}_{g.s.}$				
3.68	$^{16}_8\text{O}$	$^{13}_6\text{C}^*_{3.68} \rightarrow ^{13}_6\text{C}_{g.s.}$	×	✓	✓	✓
	$^{12}_6\text{C}$	$^{13}_6\text{C}^*_{3.68} \rightarrow ^{13}_6\text{C}_{g.s.}$				
	$^{16}_8\text{O}$	$^{12}_6\text{C}^*_{7.65} \rightarrow ^{12}_6\text{C}^*_{4.44}$	×	✓	✓	✓
3.21	$^{12}_6\text{C}$	$^{12}_6\text{C}^*_{7.65} \rightarrow ^{12}_6\text{C}^*_{4.44}$				
	$^{16}_8\text{O}$	$^{16}_8\text{O}^*_{8.87} \rightarrow ^{16}_8\text{O}^*_{6.13}$				
	$^{16}_8\text{O}$	$^{14}_6\text{N}^*_{5.11} \rightarrow ^{14}_6\text{N}^*_{2.31}$				
2.7	$^{16}_8\text{O}$	$^{11}_5\text{C}^*_{4.80} \rightarrow ^{11}_5\text{C}^*_{2.00}$	✓	✓	✓	✓
	$^{16}_8\text{O}$	$^{10}_5\text{B}^*_{3.59} \rightarrow ^{11}_5\text{B}^*_{0.718}$				
	$^{12}_6\text{C}$	$^{11}_5\text{C}^*_{4.80} \rightarrow ^{11}_5\text{C}^*_{2.00}$				
2.31	$^{16}_8\text{O}$	$^{10}_5\text{B}^*_{3.59} \rightarrow ^{11}_5\text{B}^*_{0.718}$				
	$^{16}_8\text{O}$	$^{14}_6\text{N}^*_{2.31} \rightarrow ^{14}_6\text{N}_{g.s.}$	✓	✓	✓	✓
	$^{12}_6\text{C}$	$^{11}_5\text{B}^*_{2.12} \rightarrow ^{11}_5\text{B}_{g.s.}$	✓	✓	✓	n.a.
2.0	$^{16}_8\text{O}$	$^{11}_5\text{C}^*_{2.00} \rightarrow ^{11}_5\text{C}_{g.s.}$				
	$^{16}_8\text{O}$	$^{15}_7\text{O}^*_{7.28} \rightarrow ^{15}_7\text{O}^*_{5.24}$	✓	✓	✓	✓
	$^{12}_6\text{C}$	$^{11}_5\text{C}^*_{2.00} \rightarrow ^{11}_5\text{C}_{g.s.}$				
1.88	$^{16}_8\text{O}$	$^{15}_7\text{N}^*_{7.16} \rightarrow ^{15}_7\text{N}^*_{5.27}$	✓*	✓	✓	✓
	$^{12}_6\text{C}$	$^{15}_7\text{N}^*_{7.16} \rightarrow ^{15}_7\text{N}^*_{5.27}$				
	$^{16}_8\text{O}$	$^{14}_6\text{N}^*_{3.95} \rightarrow ^{14}_6\text{N}^*_{2.31}$	✓	✓	✓	✓
1.64	$^{16}_8\text{O}$	$^{14}_6\text{N}^*_{3.95} \rightarrow ^{14}_6\text{N}^*_{2.31}$				
	$^{16}_8\text{O}$	$^{15}_7\text{O}^*_{7.56} \rightarrow ^{15}_7\text{O}^*_{6.18}$	✓*	✓	✓	✓
	$^{12}_6\text{C}$	$^{15}_7\text{O}^*_{7.56} \rightarrow ^{15}_7\text{O}^*_{6.18}$				
1.3	$^{48}_{22}\text{Ti}$	$^{46}_{22}\text{Ti}^*_{3.29} \rightarrow ^{46}_{22}\text{Ti}^*_{2.01}$				
	$^{48}_{22}\text{Ti}$	$^{47}_{22}\text{Ti}^*_{1.44} \rightarrow ^{47}_{22}\text{Ti}^*_{0.159}$	✓	✓	✓	✓
	$^{48}_{22}\text{Ti}$	$^{48}_{22}\text{Ti}^*_{2.29} \rightarrow ^{48}_{22}\text{Ti}^*_{0.983}$				
1.1	$^{48}_{22}\text{Ti}$	$^{46}_{22}\text{Ti}^*_{2.01} \rightarrow ^{46}_{22}\text{Ti}^*_{0.889}$	✓	✓	✓	✓
	$^{48}_{22}\text{Ti}$	$^{47}_{22}\text{Ti}^*_{1.25} \rightarrow ^{47}_{22}\text{Ti}^*_{0.159}$				
	$^{16}_8\text{O}$	$^{10}_5\text{B}^*_{1.74} \rightarrow ^{10}_5\text{B}^*_{0.718}$	✓	✓	✓	×
1.02	$^{12}_6\text{C}$	$^{10}_5\text{B}^*_{1.74} \rightarrow ^{10}_5\text{B}^*_{0.718}$				
	$^{16}_8\text{O}$	$^{18}_8\text{F}^*_{0.937} \rightarrow ^{18}_8\text{F}_{g.s.}$	×	×	✓	✓
	$^{48}_{22}\text{Ti}$	$^{48}_{22}\text{Ti}^*_{0.938} \rightarrow ^{48}_{22}\text{Ti}_{g.s.}$	✓	✓	✓	✓
0.889	$^{48}_{22}\text{Ti}$	$^{46}_{22}\text{Ti}^*_{0.889} \rightarrow ^{46}_{22}\text{Ti}_{g.s.}$	✓	✓	✓	✓
	$^{16}_8\text{O}$	$^{10}_5\text{B}^*_{0.718} \rightarrow ^{10}_5\text{B}_{g.s.}$	✓	✓	✓	✓
	$^{12}_6\text{C}$	$^{10}_5\text{B}^*_{0.718} \rightarrow ^{10}_5\text{B}_{g.s.}$				

TABLE 4.8: List of reactions observed during the uncollimated experiments. Multiple de-excitation reactions, which were merged in the experimental data, are reported in a common row. For each projectile, we indicated with (✓) the observed spectral lines and with (×) the reactions that were not observable or that had a negligible intensity. For the ^1_0p beams, some reactions were observed only on $^{16}_8\text{O}$ target (✓*). For the $^{16}_8\text{O}$ beams, the data on $^{12}_6\text{C}$ targets is missing and one entry was not assigned (n.a.). The de-excitation reactions were retrieved from the NUDAT database (Kinsey, 1998).

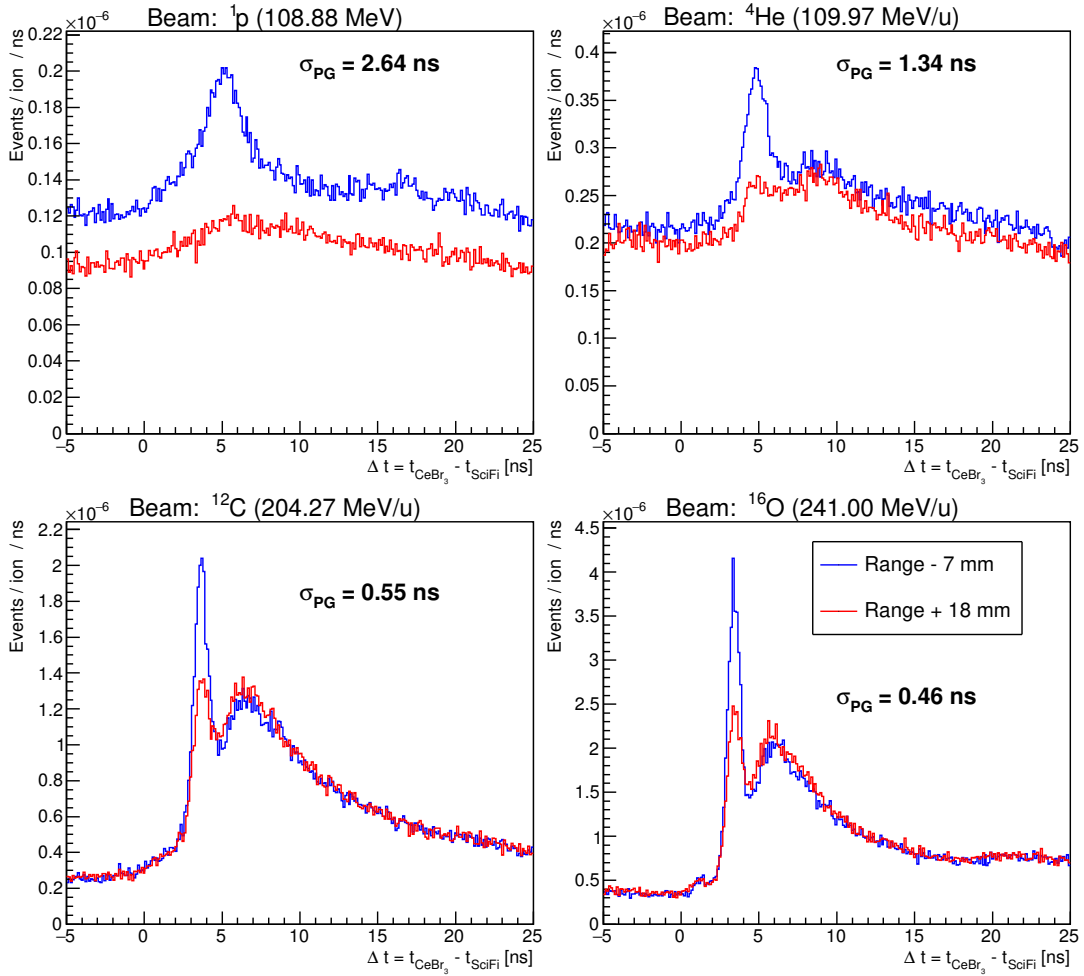


FIGURE 4.40: Time-of-Flight spectra for the prompt gamma radiation before and after the Bragg peak obtained in the collimated experiments. The comparison between the four ion species is shown. The labels in the plots report the widths of the prompt gamma peaks upstream the Bragg peak, i.e. the fit performed on the blue histogram. The counts are integrated over the $0.6 \div 6.8$ MeV energy range.

the ratio of the maximum instantaneous count rates between $z = 80$ mm and $z = 105$ mm was approximately 2 and their values downstream the Bragg peak were compatible with the ones observed for the scattered events. Moreover, we observed that the count rates at $\Delta t = 25$ ns converged to the same values for ${}^4\text{He}$, ${}^{12}\text{C}$ and ${}^{16}\text{O}$ beams, while for ${}^1\text{p}$ beams we measured an event rate + 13% higher for $z = 80$ mm compared to $z = 105$ mm. Finally, we observed a sharper ToF peak for the prompt gamma events generated by heavier projectiles, down to $\text{FWHM} = 1.08$ ns for ${}^{16}\text{O}$ beams. The values of the standard deviations of the primary prompt gamma peaks are reported in Figure 4.40. As a consequence, the ratio between the maximum and the minimum count rate strongly depended on the projectile. For ${}^1\text{p}$, ${}^4\text{He}$, ${}^{12}\text{C}$ and ${}^{16}\text{O}$ the ratios were respectively: $r = 1.8$, $r = 2.1$, $r = 8.8$ and $r = 14.2$.

Energy spectra and Bragg peak position

Binary position

The most significant differences between the data acquired upstream and downstream the Bragg peak were observable in the energy spectra reported in Figure 4.41. The efficient background suppression allowed to observe a drop of the intensities of the discrete lines when moving from $z = 80$ mm to $z = 105$ mm, both for the high and for the low energy part of the spectra. In particular, we observed that for ^1p beams the most energetic lines ($E_\gamma \geq 4.4$ MeV) were not observable at the position downstream the Bragg peak. On the other hand, for heavier projectiles the intensity of such lines were strongly reduced but the peaks in the energy spectra were still identifiable. The gamma lines at lower energy could be observed both upstream and downstream the Bragg peak with different intensities. The number of total events detected in the energy window $0.6 \div 6.8$ MeV normalized per primary ion strongly depended on the mass of the projectile. We considered the spectra acquired at $z = 80$ mm and we compared the number of events taking the ^{12}C data as the reference. For ^1p and ^4He beams we measured factors of $\Gamma_{^{12}\text{C},^1\text{p}} = 7.8$ and $\Gamma_{^{12}\text{C},^4\text{He}} = 4.8$ less events, respectively. For ^{16}O we measured a factor $1/\Gamma_{^{12}\text{C},^{16}\text{O}} = 2.1$ more events.

We observed one further effect in presence of ^{12}C and ^{16}O beams. Additionally to the discrete lines identified in Figure 4.38 we detected one more peak in each spectrum in Figure 4.41 at $z = 80$ mm. Namely, we identified a peak at $E_\gamma = 4.2$ MeV for the ^{12}C data and a peak at $E_\gamma = 5.8$ MeV for the ^{16}O data. Such lines were not observable at $z = 105$ mm. We calculated in Appendix A the Doppler shifts of the $E_\gamma = 4.4$ MeV and the $E_\gamma = 6.1$ MeV lines generated directly by ions traveling at a velocity compatible with a residual range of $r = 7$ mm. The predicted values and the measured ones were in agreement within the 1% level.

Scanning position

The evolution of the intensities of the spectral lines for the collimated experiments in presence of the ^{12}C beam is presented in Figure 4.42. We analyzed $N = 15$ reactions identified in Table 4.8 and also the integrated spectrum between $0.6 \text{ MeV} \leq E_\gamma \leq 6.8 \text{ MeV}$. A clear correlation with the Bragg peak position was observed for each of the reactions. However, the specific shape and intensity was unique to each of the gamma lines. We can observe that, in general, the high energy lines reached the maximum of the intensity just before the end of range and then they presented a sharp falloff. The behaviour at lower energies was more various and the maximum of the distribution was often reached at the Bragg peak position. A more detailed comparison between the intensities of these reactions is presented in Figure 4.43. Here, we can observe how the gamma lines at an intermediate energy present a common absolute intensity and a similar behaviour with respect to the depth in the phantom. On the other hand, radical differences were observed between

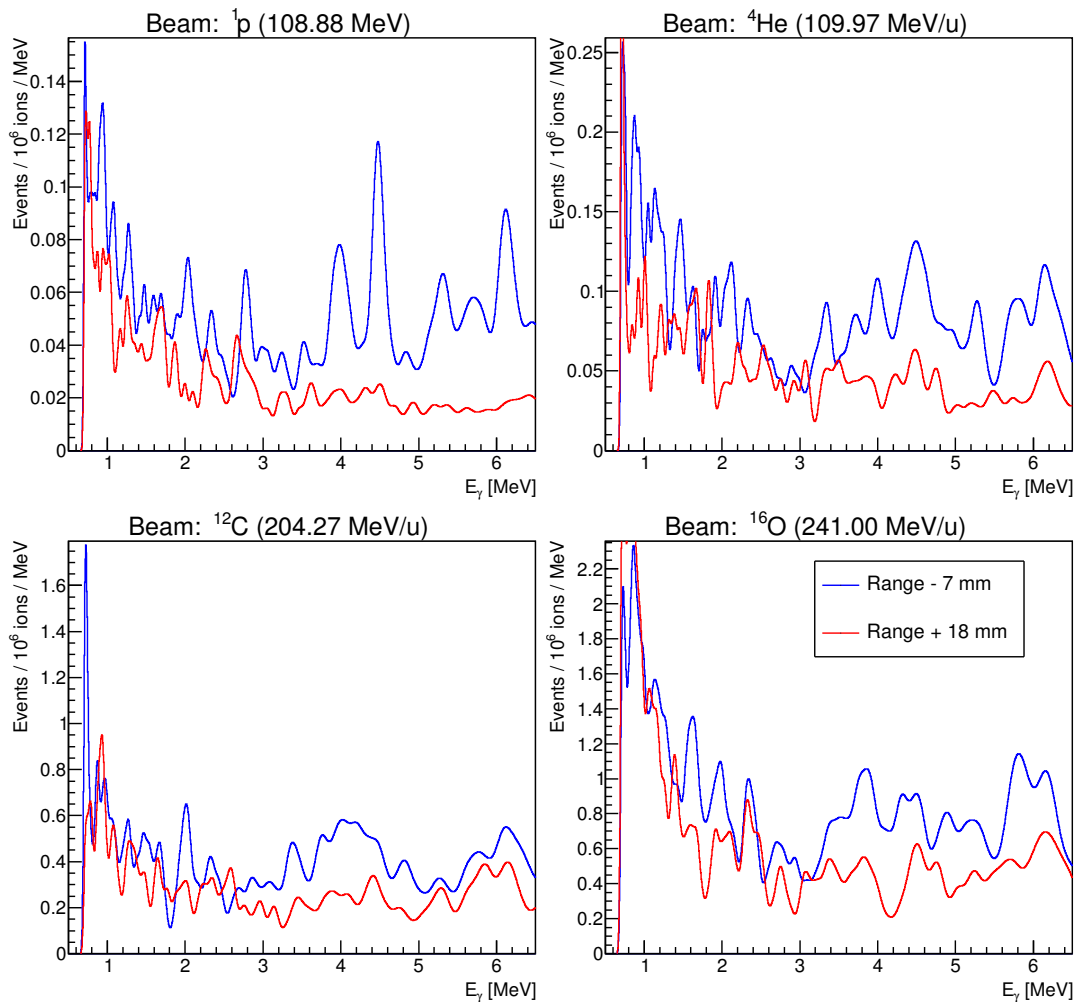


FIGURE 4.41: Energy spectra for the prompt gamma radiation before and after the Bragg peak obtained in the collimated experiments. The comparison between the four ion species is shown. The background has been suppressed after a full implementation of the background rejection techniques and the energy spectra were smoothed with a filter having a width proportional to the resolution of the CeBr_3 .

the high and the low energy prompt gamma, which could provide valuable information to retrieve the absolute Bragg peak position.

We profited from the differences observed in Figure 4.43 to extract the absolute position of the Bragg peak from the spectral information. We selected five independent pairs of prompt gamma lines from Figure 4.42 and we calculated $R_{j,k}$ at every position z_i . The results, including the propagation of the statistical errors and the parameterization of $R_{j,k}(z)$, are shown in Figure 4.44. We observed a monotonic relation between the depth in the water phantom z and the values assumed by the variables $R_{j,k}$ in a neighborhood of the Bragg peak. Therefore, the functional forms can be inverted and used to derive unequivocally the range of the primary beam. This, given the intensity of at least a pair of prompt gamma lines. We considered the ratio $R^{(1)} := I_{0.718 \text{ MeV}} / I_{4.4 \text{ MeV}}$ as an example to perform quantitative evaluations. The steepness of the curve at the Bragg peak position was $s = dR^{(1)} / dz = 0.03 \text{ mm}^{-1}$ and the average statistical error of the data points in the neighborhood of the end of the range was $\bar{\sigma}(R^{(1)}) = 0.05$. Therefore, given one single measurement, the longitudinal position of the Bragg peak z_{BP} could be recovered with a statistical uncertainty of $\sigma(z_{BP}) = \bar{\sigma}(R^{(1)}) / s = 1.67 \text{ mm}$. Similar considerations applied to the other $R_{j,k}$ and the estimation of $\sigma(z_{BP})$ ranged from a minimum of 0.96 mm to a maximum of 3.89 mm for different pairs of gamma lines.

Discussion

In this work we have presented a pre-clinical prototype for absolute range verification of ion beams at synchrotron based facilities. The study was conducted using clinically relevant beam energies and intensities. The range verification technique was based on prompt gamma spectroscopy, which has already been demonstrated for proton beams accelerated at a cyclotron based facility by Hueso-González et al., 2018. We refined the technique and we extended its applicability to heavier ions up to ^{16}O beams. This required the development of a dedicated detector system and advanced data processing routines. Using this pre-clinical prototype, we demonstrated for the first time the possibility to measure the absolute Bragg peak position for ^1p , ^4He , ^{12}C and ^{16}O beams accelerated by a synchrotron.

The development of prompt gamma spectroscopy for a synchrotron based facility and for ions heavier than protons posed several technical challenges, which we overcame. First, synchrotrons are known to have lower beam intensities compared to cyclotrons (Krimmer et al., 2018). This could facilitate the prompt gamma detection and soften the throughput requirements of the photon detector. On the other hand, the time micro-structure of the synchrotron beam is less regular and the wide time extension of the bunches does not allow to perform an efficient rejection of the neutron-induced background using only the techniques proposed by Verburg et al., 2013b; as also discussed by Krimmer et al., 2018. Therefore, we developed and implemented in the experimental setup a dedicated beam trigger. Both the EJ-200

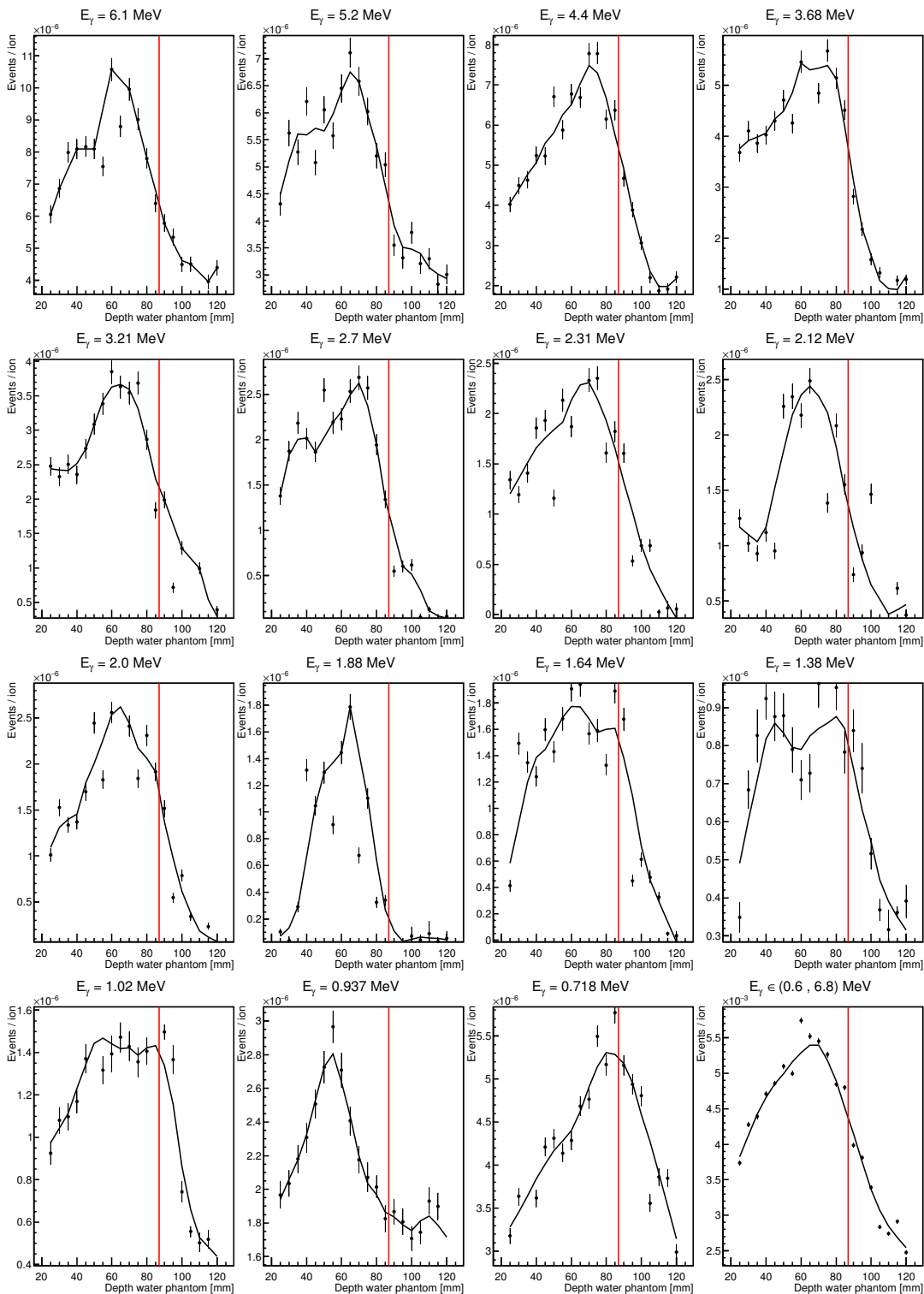


FIGURE 4.42: Evolution of the spectral lines intensities with respect to the longitudinal position of detection. The experimental data, obtained with ^{12}C beams in the collimated experiments, is shown with solid dots and its statistical uncertainty. The smoothed black lines help the reader to follow the data. The vertical red lines indicate the position of the Bragg peak.

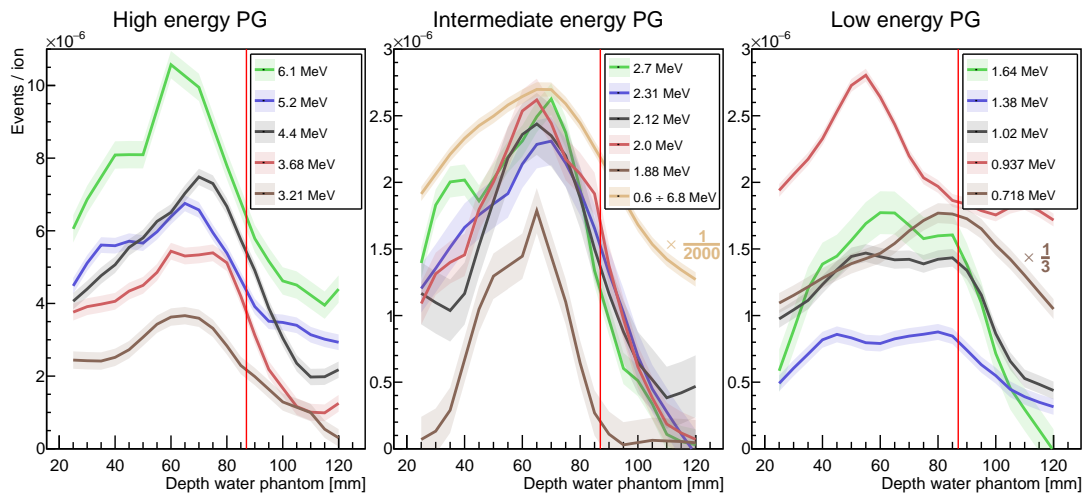


FIGURE 4.43: Comparison between multiple prompt gamma lines detected in presence of ^{12}C beams in the collimated experiments. The solid lines report the smoothed experimental data and the bands about these represent the average deviation from the original data points. Two lines were scaled to fit within the plots and their scaling factors are reported in the plot. The vertical red lines indicate the position of the Bragg peak.

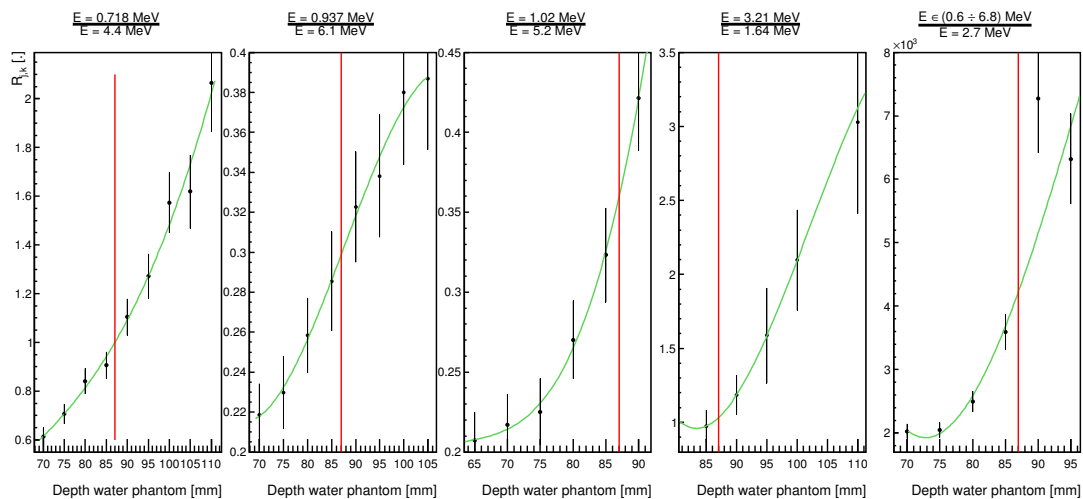


FIGURE 4.44: Ratios between the intensities of five pairs of prompt gamma lines. The experimental data is shown with solid dots and its statistical uncertainty. The green curves are the polynomial fit of the experimental data and the vertical red lines indicate the position of the Bragg peak.

detector and the SciFi detector were capable to track the arrival time of single ions. We achieved an excellent time resolution down to FWHM $\simeq 1$ ns (Figure 4.40). The SciFi detector was designed to have minimal interaction with the beam, to operate at high beam intensities and to be scalable to the highest intensities during patient treatments at HIT (Magalhaes Martins et al., 2019b). The possible implementation of scintillating fiber detectors in the nozzle for patient treatments was discussed by Leverington et al., 2018. Second, we implemented a series of robust background rejection techniques. The first steps were based on the information retrieved by the secondary detectors and were adopted also in a previous study (Dal Bello et al., 2019). We implemented also further and more advanced steps based on the detector and the ToF spectra modelling. We demonstrated in Figure 4.37 how such steps were critical to obtain a background-free spectrum at low energies. The detector effects (e.g. Compton continuum) and the neutron induced background (e.g. spectral line at $E_\gamma = 2.2$ MeV) were efficiently suppressed. The excellent time resolution achieved with the SciFi detector was critical to obtain a robust model of the ToF spectra. Moreover, we optimized the ToF model to suit the characteristics of the time spectra generated by a synchrotron beam with a minimal set of free parameters. This opened the possibility to obtain robust fits of the ToF spectra, as shown in Figure 4.35.

The efficient background rejection was fundamental to extract parameters from the time and energy spectra, which we then correlated with the range of the primary particles. We identified in total $N = 19$ independent spectral lines induced by the four beam species on the different targets. Some of the lines were unique to target nuclei found in artificial implants but not in human tissue, in this specific case the titanium. The detection of such reactions could potentially be used to identify whether the beam path crosses a metallic implant, as proposed for ^4He beams in Dal Bello et al., 2019. In the current work, we demonstrated this technique also for ^1p , ^{12}C and ^{16}O beams. Moreover, we observed that several spectral lines were generated by decays between multiple excited states without reaching directly the ground state, e.g. the chain $^{10}\text{B}_{3.59}^* \rightarrow ^{10}\text{B}_{0.718}^* \rightarrow ^{10}\text{B}_{g.s.}$ produces two gamma quanta at $E_\gamma^{(1)} = 2.7$ MeV and $E_\gamma^{(2)} = 0.718$ MeV in coincidence. The direct detection of such coincidences was not investigated in the current work. Similar prompt gamma emission chains could be identified in Table 4.8. Such reactions, in presence of multiple spectroscopic units, open the possibility to retrieve the transverse position of the prompt gamma production (Panaino et al., 2018). The $E_\gamma = 0.511$ MeV line was also detected but not analyzed. Furthermore, the background-free spectra were used to perform a quantitative analysis of the Doppler broadening. We observed that the model derived in Appendix A successfully described the experimental data. The magnitude of the effect was larger on the high energy lines compared to the low energy ones, as shown in Figure 4.39. Therefore, the capability to detect the low energy gamma lines is beneficial for a range verification system, especially in presence of ^{12}C and ^{16}O beams for which the widening of the spectral lines reached its maximum. For ^{12}C and ^{16}O beams we also observed the direct prompt gamma emission from the projectiles in Figure 4.41. The position of

the Doppler shifted peaks could potentially be used to invert the equations (4.11)-(4.16) and directly measure the residual beam energy, i.e. the residual range. However, we expect such technique not to be exploitable at the end of the range. Here, the Doppler shifts reach their minima and the peaks merge with the emission lines from the target nuclei. Nonetheless, such information could be used to obtain an independent check on whether the detection is compatible with the z ranges of Figure 4.44.

The influence of the longitudinal detection coordinate with respect to the Bragg peak position was clearly observed in the ToF spectra in Figure 4.40 and the energy spectra in Figure 4.41. We interpret the differences observed in the ToF spectra between the lightest (^1p and ^4He) and the heavier (^{12}C and ^{16}O) beams due to the fragmentation of the primary particles. For the latter, the light fragments produced before the Bragg peak travel also beyond it, exciting target nuclei and generating prompt gamma in the primary ToF peak also at $z = 105$ mm. This interpretation was supported by the spectra in Figure 4.41. Here, we observed that at $z = 105$ mm the de-excitation lines of the target nuclei are still present, while the Doppler shifted emission from the ^{12}C and ^{16}O projectiles vanished. Another significant difference in the ToF spectra was given by the number of events in the $f_S(t)$ component. This was compatible with the expected lower neutron production for ^1p and ^4He beams, which led to fewer (n, γ) reactions. The presence of a large background from (n, γ) reactions delayed by just $\Delta t \simeq 3$ ns from the prompt gamma peak requires the adoption of a dedicated beam trigger with high time resolution, especially for ^{12}C and ^{16}O beams.

The correlation of spectral parameters with the Bragg peak position was investigated in detail in presence of ^{12}C beams. We characterized the intensity of the prompt gamma lines at different depths in the phantom and presented the results in Figure 4.42 and Figure 4.43. We interpret the distinct behaviours between separate gamma lines due to the differences in the cross sections for the production of the nuclear excited states. Interestingly, the low energy gamma emissions reach their maximum intensities at the Bragg peak, i.e. where the primary ^{12}C is almost at rest. We interpret this effect assuming that the energy thresholds for such nuclear reactions are at a lower energy compared to the processes generating high energy prompt gamma. Such property could be beneficial to detect the residual range in a neighborhood of the Bragg peak. We also observed that, oppositely to the results presented by Verburg et al., 2014, the counts of the spectral lines do not drop to zero after the end of range. Again, we interpret this with the presence of nuclear fragments produced by the ^{12}C projectile, which are not created by ^1p beams. Nonetheless, it was possible to obtain a clear correlation between the spectral line intensities and the absolute Bragg peak position. We chose to calculate the ratios $R_{j,k}(z_i)$ to suppress possible systematic errors and biases introduced during the post-processing. The ten independent spectral lines used to calculate the five ratios in Figure 4.44 allowed to develop a method capable to retrieve the absolute position of the Bragg peak. The functional forms $r_{j,k}(z)$ describing the data $R_{j,k}(z_i)$ were monotonic and therefore unequivocally invertible. We propose to use such property for absolute range

verification during patient treatments. A detailed knowledge of the cross sections for the reactions listed in Table 4.8 is required. The ^{12}C and ^{16}O concentrations in the target can be derived analyzing the prompt gamma spectra (Hueso-González et al., 2018). The properties of the mixed field of ^{12}C and fragments should be calculated at every depth with Monte Carlo or analytic software, e.g. FRoG (Mein et al., 2018). Prior to the treatment, the patient specific $r_{j,k}(z)$ should be calculated along with their inverse functions $r_{j,k}^{-1}(R)$. During the treatment, the spectroscopic unit would be placed at one specific depth to measure one single $\hat{R}_{j,k} = R_{j,k}(\hat{z})$ value. The absolute Bragg peak position is then promptly estimated from the value assumed by $r_{j,k}^{-1}(\hat{R}_{j,k})$. The precision of the range estimation depends primarily on the steepness $dr_{j,k}/dz$ and the statistical uncertainty of $\hat{R}_{j,k}$. We demonstrated sub-millimetric range verification with experimental data using ^{12}C beams stopped in a water phantom. In this case, the functions $r_{j,k}(z)$ were defined empirically from the experimental data itself.

The pre-clinical prototype achieved a submillimetric statistical precision with $N_0 = 8 \cdot 10^9$ primary ^{12}C ions. Such result was obtained taking into account each $R_{j,k}$ individually. We foresee that improving detection efficiency by an order of magnitude is practicable for a full scale system, e.g. adopting multiple spectroscopic units or larger CeBr_3 crystals. The simultaneous extrapolation of the range from all the independent $R_{j,k}$ estimators or the direct comparison of the data with pre-calculated range shift scenarios is also expected to improve the efficiency approximately by a factor five. Therefore, based on the $R^{(1)}$ experimental data, we estimate that it will be possible to measure the absolute position of the Bragg peak with a statistical uncertainty of $\sigma(z_{BP}) = 2$ mm for $N_0(^{12}\text{C}) = 9 \cdot 10^7$ primary ions. Given the available experimental data, the extrapolation to the other ion species can only be preliminary. However, considering the factors $\Gamma_{12C,i}$ and scaling the statistical uncertainty to achieve $\sigma(z_{BP}) = 2$ mm, we could approximately estimate that $N_0(^1\text{p}) \simeq 7 \cdot 10^8$, $N_0(^4\text{He}) \simeq 4 \cdot 10^8$ or $N_0(^{16}\text{O}) \simeq 4 \cdot 10^7$ primary ions would be required. While we observe that the number of primary ions decreases with heavier projectiles we should remind that this is compensated by a decreasing number of particles irradiated to achieve a given dose, as presented in Appendix B. The values assumed by $N_0(^A\text{X})$ make impracticable the verification of the range on a spot-by-spot basis during a single fraction delivery of $D = 2$ Gy, for any of the ions considered. Techniques such as spot merging would be required. In this case, we sum the statistics provided by all the particles delivered within a circle on a transverse plane (x, y) of the most distal layer. The area of the spot merging is ion dependent and we calculated that, to achieve $N_0(^A\text{X})$, we require radii of $\zeta(^1\text{p}) = 8.7$ mm, $\zeta(^4\text{He}) = 12.4$ mm, $\zeta(^{12}\text{C}) = 14.1$ mm or $\zeta(^{16}\text{O}) = 11.5$ mm. We observe that, analogously to previous studies, a compromise should be taken between the fidelity interval in tracking the beam in the transverse and longitudinal direction. The precision in these two dimensions could be equalized to obtain a voxel-like grid where the Bragg peak position is tracked. The minimum radii of the single grid elements should be $\zeta = 4$ mm for ^1p beams and $\zeta = 5$ mm for all the

other beam species. Such results show once more the challenge of applying PGS to heavier ions, nonetheless they are promising and would help reducing the physical beam uncertainties currently present in clinical practice.

Conclusions

We present the results obtained with a pre-clinical prototype for absolute ion beam range verification at a synchrotron based facility. Experiments with ^1p , ^4He , ^{12}C and ^{16}O beams at clinically relevant energies and intensities were conducted. The results demonstrate for the first time absolute range monitoring by means of prompt gamma for ions heavier than protons. For the longitudinal beam tracking only, submillimetric precision was achieved with the experimental setup and we estimate that $\sigma(z_{BP}) = 2$ mm is practicable for every ion species with a full prototype during a single fraction delivery of $D = 2$ Gy. For a multi-dimensional tracking, a precision of $\xi = 4$ mm for ^1p beams and $\xi = 5$ mm for heavier ions is achievable simultaneously in the transverse and longitudinal directions. The promising results encourage future work, which will start from the cross sections measurement.

Acknowledgments

Author R.D.B. is supported by the International Max Planck Research School for Quantum Dynamics in Physics, Chemistry and Biology, Heidelberg, Germany. P.M.M. is supported by a research fellowship for postdoctoral researchers from the Alexander von Humboldt Foundation, Bonn, Germany. The authors thank the radiation protection department of the DKFZ, in particular Mechthild Kämmer, for the support with calibration sources. The authors also thank the staff of the department of medical physics in radiation oncology of the DKFZ, in particular Gernot Echner, Armin Runz and Peter Häring for the support with the experimental setup.

Appendix A

In this appendix we derive the equations that describe the influence of the Doppler effect on the detected spectra. Two separate effects are derived for the collimated and the uncollimated experiments. In the former, we derive the Doppler shift of the radiation emitted by the excited projectile at a well defined residual kinetic energy. In the latter, we approximate the Doppler broadening by averaging over multiple Doppler shifts of the radiation emitted in center of mass of the collision.

Let us first consider the collimated case, where the residual kinetic energy of the projectile is known. Moreover, we consider the emission of the prompt gamma only from the excited projectiles ^{12}C and ^{16}O and not from the target nuclei. A photon of energy E_0 emitted by an excited nucleus moving at speed β with respect to the laboratory frame is detected at an angle θ with an energy E_m given by

$$E_m = E_0 \cdot \frac{\sqrt{1 - \beta^2}}{1 - \beta \cdot \cos \theta} \quad (4.11)$$

in our experiments we have the condition $\theta = \frac{\pi}{2}$ and the equation (4.11) reduces to

$$E_m = E_0 \cdot \frac{\sqrt{1 - \beta^2}}{1 - \beta \cdot \cos \frac{\pi}{2}} = E_0 \cdot \sqrt{1 - \beta^2} = \frac{E_0}{\gamma}. \quad (4.12)$$

The data upstream the Bragg peak presented in Figure 4.41 has been measured where the residual range of the primary ions was $R_r = 7$ mm, which correspond to

$$E_{kin}(^{12}\text{C}) = 48 \text{ MeV/u} \quad \longrightarrow \quad \gamma(^{12}\text{C}) = 1.0515 \quad (4.13)$$

$$E_{kin}(^{16}\text{O}) = 56 \text{ MeV/u} \quad \longrightarrow \quad \gamma(^{16}\text{O}) = 1.0601. \quad (4.14)$$

We consider the arithmetic average of the gamma quanta emitted by the merged reactions at $E_0^{(1)} = 4.445$ MeV and $E_0^{(2)} = 6.155$ MeV, respectively by the projectiles ^{12}C and ^{16}O . These are detected in the laboratory rest frame at a lower energy according to (4.12)-(4.14), obtaining

$$E_m^{(1)} = 4.445 \text{ MeV}/1.0515 = 4.227 \text{ MeV} \quad \longrightarrow \quad \Delta E^{(1)} = 0.218 \text{ MeV} \quad (4.15)$$

$$E_m^{(2)} = 6.155 \text{ MeV}/1.0601 = 5.806 \text{ MeV} \quad \longrightarrow \quad \Delta E^{(2)} = 0.349 \text{ MeV}. \quad (4.16)$$

A different situation is present in the uncollimated experiments. Here, the kinetic energy of the projectile inducing prompt gamma production spans from the maximum beam energy to zero. We also consider the emission of the gamma quanta by the target nuclei. The net effect is the superposition of multiple Doppler shifted peaks in the spectrum and therefore wider spectral lines. Let us first calculate the center of mass energy of a collision between a generic projectile of mass $m_p = A \cdot u$ having total energy $E_A = \gamma_p \cdot A \cdot u$ with

a ^{16}O target nucleus of mass $m_t = 15.9949 \cdot u \simeq 16 \cdot u$

$$E_{CM}^2 = s^2 = \left[\begin{pmatrix} E_A \\ \vec{p}_A \end{pmatrix}^2 + \begin{pmatrix} 16 \cdot u \\ 0 \end{pmatrix}^2 \right] = (A \cdot u)^2 + (16 \cdot u)^2 + 32 \cdot \gamma_p \cdot A \cdot u^2. \quad (4.17)$$

The equation (4.17) can be used to calculate the Lorentz factor of frame moving with the center of mass

$$\gamma_{CM} = \frac{E_{CM}}{(16 + A) \cdot u} = \frac{\sqrt{A^2 + 16^2 + 32 \cdot \gamma_p \cdot A}}{16 + A}. \quad (4.18)$$

We observe that for the data presented in Figure 4.38 the projectiles have an initial energy corresponding to a maximum $\gamma_p^{max} = 1.35$ for ^{16}O and a minimum $\gamma_p^{min} = 1.15$ for ^1p . In (4.18) we approximate $\gamma_p \simeq \bar{\gamma}_p := 0.5 \cdot (\gamma_p^{max} + \gamma_p^{min}) = 1.25$. We also approximate the total widening of the spectral line having nominal energy E_0 with a linear relation to the Doppler shift, namely

$$FWHM \simeq \kappa \cdot |E_m - E_0|. \quad (4.19)$$

Plugging (4.12) and (4.18) into (4.19) we obtain

$$FWHM = \kappa \cdot E_0 \cdot \frac{\sqrt{A^2 + 16^2 + 32 \cdot \bar{\gamma}_p \cdot A} - 16 - A}{\sqrt{A^2 + 16^2 + 32 \cdot \bar{\gamma}_p \cdot A}} \quad (4.20)$$

to describe the widening of the spectral lines with increasing mass of the projectile. This effect can be seen as a direct consequence of the greater center of mass velocities for heavier projectiles.

Ion	$\sum_{IES} N_0(IES)$	$N_0(IES = 17)$	ρ [ions · mm ⁻²]	A [mm ²]	ξ [mm]
¹ p	$2.73 \cdot 10^{10}$	$7.44 \cdot 10^9$	$2.98 \cdot 10^6$	235.1	8.7
⁴ He	$7.22 \cdot 10^9$	$2.06 \cdot 10^9$	$8.25 \cdot 10^5$	484.6	12.4
¹² C	$1.34 \cdot 10^9$	$3.59 \cdot 10^8$	$1.44 \cdot 10^5$	626.4	14.1
¹⁶ O	$8.68 \cdot 10^8$	$2.42 \cdot 10^8$	$9.69 \cdot 10^4$	413.0	11.5

TABLE 4.9: Properties of the treatment plans delivering a $D = 2$ Gy dose box. The columns report in order the total number of ions irradiated, the ions in the most distal layer, the transverse ion density in the most distal layer, the area to be integrated to reach $\sigma(z_{BP}) = 2$ mm and the corresponding integration radius.

Appendix B

In this appendix we derive the relations between the dose, the number of ions irradiated and the statistical requirements for the range measurements. We used the treatment planning system syngo.via¹¹ to calculate four plans delivering uniform dose boxes to a volume $V = 50 \times 50 \times 50$ mm³ for the ions used in the current study. We chose to deliver $D = 2$ Gy physical dose in accordance to the single fraction delivery used in previous studies (Richter et al., 2016). We calculated the plans for ¹p, ⁴He, ¹²C and ¹⁶O beams with identical properties, namely: $\Delta x = \Delta y = 3$ mm transverse spacing between the single spots and $N_{IES} = 17$ iso-energy slices (IES). The deepest IES corresponded to the energy used in the collimated experiments. Each plan had a total of $N_P = 4913$ points, of which $N_P/N_{IES} = 289$ at the most distal layer. The number of particles irradiated was uniformly distributed among the pencil beam points in each IES. Further properties of the plans are summarized in Table 4.9. The most fundamental parameter for statistical considerations is the transverse ion density ρ irradiated to the most distal layer. While the number of particles per single spot depends on other parameters (e.g. Δx), the value of ρ is in first approximation constant. Assuming a uniform distribution in a small transverse neighborhood, we can calculate the area where the single spots need to be merged to achieve the minimum number of primary ions $N_0(^AX)$ required to retrieve the range with a statistical precision of $\sigma(z_{BP}) = 2$ mm. The area is given by $A = N_0(^AX)/\rho$. Finally, the integration radius is given by $\xi = \sqrt{A/\pi}$. We observe that the ξ values range approximately between $3 \cdot \Delta x$ and $5 \cdot \Delta x$ for this specific calculation. We obtained an integration radius for ¹p comparable to the one adopted by Hueso-González et al., 2018. However, it has to be reminded that in our calculation we did not merge the statistics accumulated in the longitudinal direction z , i.e. only the most distal IES was taken into account.

¹¹Siemens Healthcare GmbH, Erlangen, Germany

Chapter 5

Discussion

In this thesis a synchrotron dedicated system for absolute range monitoring was presented. The experimental setup was designed to be used with all the ion species available at the HIT facility, namely ^1p , ^4He , ^{12}C and ^{16}O beams. The correlation of the absolute Bragg peak position with the information extracted from the energy spectra was experimentally demonstrated for the first time for ^{12}C beams and further conclusions were drawn for the other ions.

In this chapter, the most important findings, achievements and limitations of the developed methodology for prompt gamma spectroscopy are discussed. Whenever possible, the results are compared to other published concepts and detection systems for prompt gamma imaging.

5.1 New findings in prompt gamma spectroscopy

The prototype presented by Hueso-González et al., 2018 was so far the only device developed to measure the Bragg peak position using the prompt gamma spectroscopy technique in clinically relevant conditions¹. This thesis presents the development of a new system based on different technology for what concerns the scintillating crystals, the electronics, the beam trigger and the data analysis. The design of a new prototype without relying on existing technology provided the challenges but also the opportunities to investigate and explore some aspects that were not considered by previous studies. The most important questions that were raised and were so far unanswered could be summarized in the following points:

1. Is it possible to efficiently suppress the background and detect the prompt gamma spectral lines over the full energy spectrum?
2. Are the low energy spectral lines directly correlated to the Bragg peak position?
3. Is it possible to detect the presence of non-tissue materials along the beam path?

¹The clinically relevant conditions should combine: (i) thick ($l \geq 5$ cm) target experiments, (ii) high intensity ($I \geq 10^6$ ions \cdot s⁻¹) ion beams and (iii) high energy primary particles with sufficient ($r \geq 5$ cm) penetration potential in water.

4. What is the amplitude of the Doppler broadening for primary ions heavier than protons and does this impede the use of prompt gamma spectroscopy?
5. What is the effect of the mixed radiation field including light fragments for primary ions heavier than protons and does this impede the use of prompt gamma spectroscopy?

The experimental results presented in the publications A.I, A.III and A.V provide the answers to all the previous questions. Each of the points had a positive outcome. Such findings were supported by quantitative analysis of the experimental data. The extensive discussion of the results is provided in the following paragraphs.

The use of a scintillating crystal that combined high energy and time resolutions with absence of intrinsic activity was proposed in the publication A.V. The detection of the prompt gamma radiation with the CeBr₃ allowed to identify multiple spectral lines over the full energy spectrum, the lowest spectral line being the one at $E_\gamma = 511$ keV induced by the β^+ decay. The previous system based on LaBr₃ scintillating crystals detects the lowest energy line at $E_\gamma = 1.63$ MeV. The spectral lines presented in Table 4.1 show how three additional reactions could be identified with the CeBr₃ detector. In this case, the background rejection was realized with the sole application of a time of flight window $\Delta t = 1$ ns wide. As a matter of fact, the high energy component of the spectrum in Figure 4.4 shows that the single and double escape peaks have intensities higher than the photopeaks. Also, the low energy component is affected by a significant Compton continuum background. Being this a possible limitation for the measurement of the peaks intensities, a dedicated active shield was optimized in the publication A.IV and later experimentally implemented in A.III. The results show an improvement in the signal to noise ratios for the high energy peaks and the detection of one additional spectral line, namely the reaction $^{15}\text{O}_{7.55}^* \rightarrow ^{15}\text{O}_{6.17}^*$ producing a photon of energy $E_\gamma = 1.38$ MeV. The results show that the use of a scintillating crystal without intrinsic activity is beneficial for prompt gamma spectroscopy but it is not sufficient to fully exploit the potential of the detection of the gamma radiation over its full energy spectrum. The use of an active shield improves significantly the spectroscopic performances. This statement is further supported by the statistical analysis presented in Figure 4.20. Therefore, the results presented in the publications A.III, A.IV and A.V provide a positive answer to the first question of the list. It is demonstrated that it is possible to efficiently suppress the background and detect the prompt gamma spectral lines over the full energy spectrum in clinically relevant situations.

The correlation of the spectral lines intensities with the Bragg peak position was then investigated in the publication A.I. The background rejection was further improved with the introduction of a time of flight model and a detector response model (Figure 4.37). One additional spectral line at $E_\gamma = 0.937$ MeV was identified, increasing to five the additional reactions

measurable with a CeBr₃ compared to a LaBr₃ crystal. This reaction was observed only in presence of ¹²C and ¹⁶O beams. The low energy spectral lines do not drop to zero-intensity downstream the Bragg peak, as the high energy ones do for ¹p beams (Figure 4.41). Therefore, it is not possible to directly draw a binary conclusion on whether the detection point is located upstream or downstream the range of the primary particles. Nevertheless, it was observed a significant intensity variation that could serve for the purpose of measuring the Bragg peak position. A deeper investigation was conducted with ¹²C beams and the right frame of Figure 4.43 demonstrates the correlation of the low energy spectral lines with the Bragg peak position. It is interesting to notice that, in general, the high and intermediate energy lines reach their maximum few millimeters before the range, while the low energy lines have their maximum at the Bragg peak location. We interpret this effect assuming that the energy thresholds for such nuclear reactions are at a lower energy compared to the processes generating higher energy prompt gamma radiation. Such property could be beneficial to detect the residual range in a neighborhood of the Bragg peak. A similar effect was observed also for the $E_\gamma = 4.4$ MeV line by Kelleter et al., 2017 in a thin target experiment. In this case, the maximum of the intensity was close to the Bragg peak position when the detector was placed at $\theta = 120^\circ$ instead of $\theta = 90^\circ$. This study did not investigate the low energy spectral lines. The results presented in the publication A.I provide a positive answer to the second question of the list. It is demonstrated that the low energy spectral lines can be used to retrieve the Bragg peak position.

Metal implants are known to severely alter the dose distribution and require dedicated techniques to ensure the correct delivery (Verburg et al., 2013a; Dietlicher et al., 2014). The different interaction properties of the beam with the metals lead on one hand to errors in the dose calculation with pencil beam algorithms but also to the opportunity to detect specific signatures of such interactions. In particular, the density of the nuclear levels in the energy domain increases with an increasing number of nucleons. An example was shown in Figure 2.3 for light nuclei. The implants found in human body are commonly made by metals with $A \geq 20$, e.g. titanium or gold. Therefore, the interaction of the beam particles with the implants is expected to produce discrete gamma lines at low energy. The detection of such reactions was proposed and experimentally verified for ¹p beams in A.V, confirmed for ⁴He beams in A.III and finally extended to all the ions in the publication A.I. The capability to detect the presence of a thin metal structure within a larger target made of lighter nuclei can be used to verify the correct relative position between the beam and a patient presenting implants. The detection of the prompt gamma emission from a purely metallic target can be achieved introducing a time of flight window for the background rejection (Figure 4.6). On the other hand, if the metal is placed within a larger phantom the active background rejection is crucial to increase the signal to noise ratio (Table 4.4). These findings confirm that it is possible to detect the presence of non-tissue materials along the beam path and open to the possibility of using such effect to verify the relative position between the beam and the patient.

The prompt gamma radiation is emitted in a system of reference that is moving with respect to the detector. An extensive description of the consequences was provided in the appendix A of the publication A.I. The greater the mass of the projectile, the wider the spectral lines. The effect was quantified and presented in Figure 4.39. It is possible to further develop the discussion taking into account the intrinsic resolution of the scintillating crystal adopted in the experiments. In particular, for the $E_\gamma = 0.718$ MeV spectral line, the intrinsic resolution of the CeBr₃ produces a peak having FWHM = 32 keV upon incoming mono-energetic radiation. The additional effect of the Doppler broadening leads, at the two extremes, to detected peaks having FWHM = 39 keV for ¹p beams and FWHM = 54 keV for ¹⁶O beams. Assuming the employment of an ideal detector with perfect energy resolution, the broadening introduced by the CeBr₃ can be quadratically subtracted. The detected peaks would be FWHM = 22 keV and FWHM = 43 keV wide, respectively for ¹p and ¹⁶O beams. We could therefore observe that the energy resolution of the CeBr₃ deteriorates the widths of the peaks by over +75% for ¹p and only by +25% for ¹⁶O, with respect to what would be achievable with a detector having an ideal energy resolution. The behaviour in presence of ¹²C beams is comparable to the one for ¹⁶O beams. The ⁴He beams present an intermediate situation between ¹p and the heavier ions. Similar considerations apply also for the other spectral lines. Nevertheless, even in presence of a significant Doppler broadening, it is possible to clearly identify 19 independent spectral lines (Table 4.8) and therefore this does not impede the use of prompt gamma spectroscopy. Also, a significant gain could be obtained for ¹p beams employing a detector with better energy resolution since the widening of the spectral lines in our experiments was dominated by the scintillating crystal. On the other hand, for ¹²C and ¹⁶O beams the widening was dominated by the Doppler broadening and the employment of a detector with better energy resolution would lead to a limited improvement in the energy spectra.

Finally, the presence of lighter charged fragments along with the primary ions produces additional prompt gamma signal. This applies especially for ¹²C and ¹⁶O beams. Such radiation is not directly correlated to the Bragg peak position since the fragments have broad energy spectra and they have a range than can be greater than the one of the beam particles. As a matter of fact, for a high energetic ¹²C beam at the Bragg peak location, the number of $Z = 1$ and $Z = 2$ fragments can be a factor, respectively, $\times 3$ and $\times 2$ more abundant than the primary ions (Figure 5.1). Despite their abundance, the fragments contribute only approximately up to 1/10 of the total dose delivered at the Bragg peak (Sihver et al., 1998). This could be interpreted due to the dependency on z^2 presented in equation 2.1. On the other hand, the most abundant fragments, i.e. protons, are known to induce intense prompt gamma radiation. Therefore, it could not be assumed a priori that the prompt gamma signal is correlated to the Bragg peak position also for ¹²C and ¹⁶O beams. This required an experimental assessment of the effect, which was analyzed in detail for ¹²C beams in water having an initial energy of $E_{\text{kin}} = 204.27$ MeV/u. Significant differences were observed in the

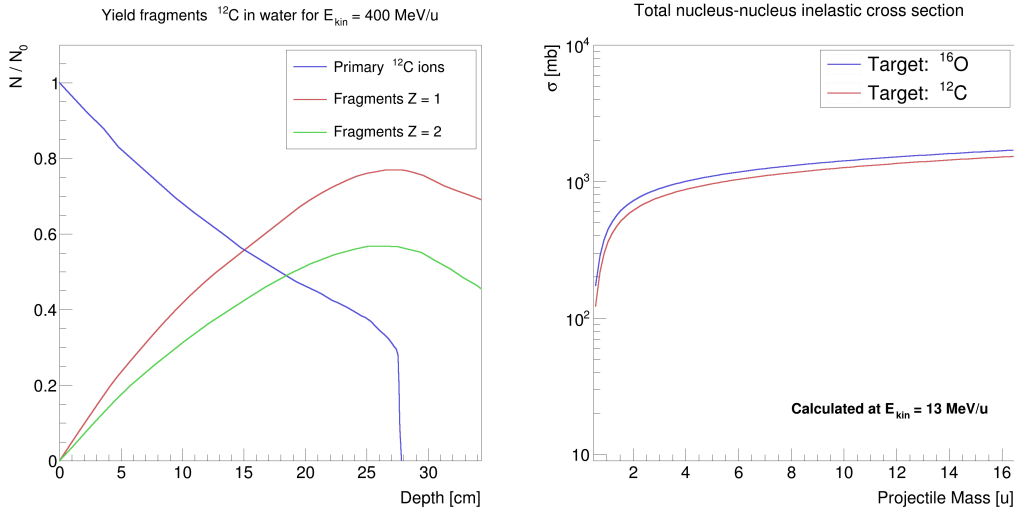


FIGURE 5.1: *Left*: Multiplicity of charged particles at different depths in water obtained with a ^{12}C beam having initial energy $E_{\text{kin}} = 400$ MeV/u. Data reproduced from Haettner et al., 2013 *Right*: Total reaction cross section for nucleus-nucleus interaction. The evolution of the cross section is shown against the mass of the projectile both for a ^{12}C and ^{16}O target. The value of the cross section was calculated for an energy of the projectile of $E_{\text{kin}} = 13$ MeV/u according to the model proposed by Townsend et al., 1986.

time of flight (Figure 4.40) and energy (Figure 4.41) spectra before and after the Bragg peak between ^1p and ^{12}C beams. The presence of an intense peak in the former and of high energy spectral lines in the latter even downstream the primary particles range should be attributed to the light fragments. Nevertheless, an in-deep analysis of the evolution of the intensities for the individual spectral lines showed a strong correlation with the Bragg peak position (Figure 4.42). We could interpret this taking into account the total cross section for inelastic nucleus-nucleus reactions. Townsend et al., 1986 proposed an energy dependent extension of the Bradt-Peter parameterization:

$$\sigma_{\text{tot}} = \pi r_0^2 \frac{1}{5 \cdot E} \cdot \left[a^{1/3} + A^{1/3} - 0.2 + \frac{1}{a} + \frac{1}{A} - c_1 \cdot e^{-E/c_2} \cdot \cos(c_3 \cdot E^{c_4}) \right] \quad (5.1)$$

where A is the nuclear mass of the target, a the nuclear mass of the projectile, E the kinetic energy of the projectile in MeV/n, $r_0 = 1.26$ fm and the c_i are a set of constants². The values of the cross sections calculated according to equation 5.1 for ^{16}O and ^{12}C targets as a function of the projectile mass are shown in Figure 5.1. The value assumed by σ for ^{12}C projectiles is almost an order of magnitude larger compared to the one for ^1p projectiles. Therefore, despite the greater number of $Z = 1$ and $Z = 2$ fragments at the Bragg peak, the most intense source of prompt gamma radiation are the primary ^{12}C ions. Such interpretation, supported by the experimental data presented

²Values of the constants: $c_1 = 0.292$, $c_2 = 792$, $c_3 = 0.229$, $c_4 = 0.453$

in the publication A.I, provides an answer to the last question of the list. We can conclude that the mixed radiation field produces additional secondary radiation not correlated with the Bragg peak position but the use of prompt gamma spectroscopy to retrieve the primary particles range is not compromised.

5.2 Features specific to synchrotrons and ion beams

The extension of prompt gamma to synchrotrons and ions heavier than protons required the introduction of an additional detector between the beam nozzle and the target. During the experiments we also detected some effects not observed for protons and unique to heavier ions.

The demand of a beam trigger is strictly related to the time structure of the accelerator and the time of flight spectra of the prompt gamma. The properties of different accelerators were presented in Table 2.1. The time separation between prompt gamma and background was first analyzed by Testa et al., 2010 and then further investigated for all the ion beams in Figure 4.40. We observed that the relevant prompt gamma peak is separated from the background by approximately $\Delta t = 3$ ns and it contains a larger number of events. Therefore, the time of flight windows to be applied during PGI should be $\Delta t < 3$ ns wide in order to exclude the radiation not correlated to the Bragg peak position. This could be achieved for cyclotrons by using the accelerator radio-frequency as reference. The arrival time of the proton bunches is correlated to such signal and the time spread is less than $T_{bw} < 2$ ns. Accepting the gamma signals from the time t_1 corresponding to a given phase of accelerator radio-frequency to the time $t_2 = t_1 + 2$ ns, one can detect all the relevant prompt gamma and reject the background. Such approach is not applicable to synchrotrons since the bunch width can be as wide as $T_{bw} = 75$ ns. The application of the previous technique would favour the detection of the background instead of the prompt gamma. The direct detection of the arrival time of single particles delivered by the accelerator is necessary. Since such detector would be placed between the beam nozzle and the patient, several strict requirements were set before its development. The requirements are: tracking the arrival time of single particles within ion bunches, provide a time resolution better than $\sigma(t) = 1$ ns, being able to cope with the clinical intensities, being radiation hard and have an as limited as possible interaction with the beam. A detector based on scintillating fibers was the best choice to satisfy the list of requirements. The radiation hardness and the beam perturbation induced by scintillating fibers was investigated by Leverington et al., 2018. The other requirements were investigated and demonstrated with a small scale prototype in the publication A.II. In particular, the design presenting independent readout of neighbouring fibers can be scaled to cope with the highest clinical intensities. To achieve this, it is exploited the fact that beam has a finite transverse dimension and different particles cross the trigger at separate vertical positions. Only a limited number ($n < 10$) of single events can be separated in each fiber. However, their small diameter allows to fit multiple independent readout channels within

the beam spot size and it is possible to track up to $n = 300$ single particles per bunch. This makes possible to track single particles at the highest clinical intensities. Finally, the analysis of the energy deposition in such detector allows to distinguish the ion type. This property could be used during the commissioning phase of a facility to determine the amount of contamination of ion beams with lighter ions or to apply techniques such as the monitoring of treatments with mixed beams (Graeff et al., 2018).

Few new phenomena were observed for ^{12}C and ^{16}O beams only. The increased Doppler broadening and the prompt gamma signal from the light fragments was discussed in the previous subsection. Along with these effects, we observed also the Doppler shifted prompt gamma emission from the projectiles and a greater importance of the low energy spectral lines to achieve range monitoring. In the first case, we observed in the experimental data that for positions upstream the Bragg peak there is one additional peak connected to the $^{16}\text{O}_{6.13}^* \rightarrow ^{16}\text{O}_{g.s.}$ transition in presence of ^{16}O beams and one connected to the $^{12}\text{C}_{4.44}^* \rightarrow ^{12}\text{C}_{g.s.}$ transition in presence of ^{12}C beams. Such transitions involve directly the de-excitation of the projectile, they happen on a frame of reference that is moving at a relativistic speed with respect to the laboratory frame and therefore undergo a Doppler shift according to the description presented in the Appendix A of the publication A.I. We observed a good agreement between the theoretical prediction and the experimental data presented in Figure 4.41. The relative position between the Doppler shifted peaks connected to the de-excitation of the projectiles and the non-shifted peaks connected to the de-excitation of the target nuclei provides a direct measurement of the residual kinetic energy of the projectile, i.e. the residual range at the detection point. However, we expect such approach not to be exploitable at the end of the range. Here, the Doppler shifts reach their minima and the peaks merge with the emission lines from the target nuclei. Nonetheless, such information could be used to obtain an independent check on whether the detection is compatible with the z ranges of Figure 4.44. Finally, the detection of the low energy spectral lines is expected to be of greater importance when measuring the absolute range of ^{12}C and ^{16}O beams. This is supported by two observations. First, one additional spectral line at $E_\gamma = 0.937$ MeV from the reaction $^{18}\text{F}_{0.937}^* \rightarrow ^{18}\text{F}_{g.s.}$ was observed only for such heavier projectiles. Second, the Doppler broadening quantified in Figure 4.39 is more pronounced for the high energy lines. As a matter of fact, the average increase of the FWHM was $\times 1.51$ for the $E_\gamma = 0.718$ MeV line and $\times 2.55$ for the $E_\gamma = 6.1$ MeV line. This, together with the increased broadening with heavier projectiles, leads to the fact that the high energy lines are often merged while the low energy ones can be still clearly separated (Figure 4.38). Therefore, we can conclude that the choice of a detector without intrinsic activity and the adoption of dedicated background rejection procedures to measure the low energy spectral lines is especially beneficial in presence of ^{12}C and ^{16}O beams.

5.3 Towards clinical applicability

Some of the prompt gamma prototypes presented in Table 2.2 reached the patient testing phase. The knife-edge slit camera was proposed in 2012 (Smeets et al., 2012) and tested during active scanning treatments in 2017 (Xie et al., 2017). Prompt gamma spectroscopy for proton beams was proposed in 2012 (Verburg et al., 2012) and the patient testing is planned during 2019 (Hueso-González et al., 2018). The INSIDE project, which aims to measure the range with the complementary signals from β^+ isotopes and secondary charged particles, was proposed in 2014, later published in the conference proceedings (Marafini et al., 2015) and the patient testing with both the PET heads and the particle tracker is planned during 2019 (Fiorina et al., 2019). All the previously listed prototypes are so-far employed during patient treatments with a passive approach, i.e. monitoring the dose delivery without interacting with the patient and without actively modifying the treatment in presence of deviations. We observe that approximately 6 year are in general required between the proposal of a novel monitoring technique until its first passive application during patient treatments. An active application would require further certification of the medical product and quality assurance tests. Given that the use of CeBr₃ for prompt gamma spectroscopy was proposed in 2017 in the publication A.V, the clinical application of the developed system remains outside the scope of the current thesis. Nevertheless, it is possible to develop a discussion towards its future clinical applicability.

This thesis developed a pre-clinical prototype that demonstrated absolute range control for ions accelerated by synchrotrons. The following full-scale prototype should be based on the findings presented here. Three main requirements will need to be satisfied: (i) the beam trigger should cover a transverse area of approximately $A = 25 \times 25 \text{ cm}^2$ to include all the scanning field; (ii) the sensitivity of the spectroscopic unit should be increased by one order of magnitude to provide millimetric range control during a single fraction; (iii) the data acquisition system should be extended to acquire signal from a more complex set of detectors. Such conditions could be realized by: (i) increasing the length and the number of fibers used in the beam trigger; (ii) adopting multiple and larger CeBr₃ crystals to build up to 10 spectroscopic units to be operated in parallel; (iii) exploiting the fully parallelizable architecture of the FlashCam. Such upgrades would provide a prototype capable of measuring the absolute position of the Bragg peak with a resolution of $\sigma(z) = 2 \text{ mm}$ during the delivery of a single fraction of $D = 2 \text{ Gy}$, as calculated in the publication A.I.

Similarly to the previous systems, the first application of the full-scale prototype would be the passive monitoring of the treatments. Additionally to the other solutions, it would also be possible to monitor patients presenting metal implants or metallic markers. The possibility to measure the absolute Bragg peak position instead of the relative deviation with respect to the first fraction would lead to avoid possible systematic errors induced by range shifts not detected in the first fraction. Moreover, such system would be the first prompt gamma device to be applied during ¹²C treatments and

a passive and retrospective study would provide a significant feedback on the robustness of the different margin concepts currently in use and previously presented in Figure 1.1. Finally, the design of the prompt gamma spectroscopy system does not conflict with the simultaneous detection of secondary charged particles and the presence of two PET heads. Therefore, a possible integration of independent detector systems based on different secondary nuclear products could be practicable.

5.4 Limitations and conceivable solutions

The limitations of the presented system can be divided in two categories. The first set is related to the detector technology and the second to the geometrical setup and the implementation during the clinical workflow.

The introduction of additional material between the beam nozzle and the patient should be avoided. However, the beam trigger is a strict requirement for prompt gamma imaging. Its presence reduces the energy of the primary ions before reaching the patient and increases the lateral scattering. The amplitude of such effects is minimized by the limited thickness of the scintillating fibers, nonetheless these should be taken into account. The implementation in the base data of the treatment planning system of the beam properties downstream the beam trigger would ensure the correct modelling of the treatment delivery. Also, the cross talk between the single fibers can be rejected in the post-processing in presence of two photomultipliers. For a full scale beam trigger with more than 60 independent photomultipliers, the cross talk may compromise the data quality. Commercial solutions are available to overcome this problem. Additionally to the optical cladding, an extra mural absorber coating could be added. Such white or black coatings may be applied to the outer fiber surface to eliminate cross talk among closely packed fibers. The coatings are typically $10 \div 15 \mu\text{m}$ thick. Additional limitations may be related to the readout electronics. At the highest clinical intensities, the detectors count rate can be up to two orders of magnitude larger than what observed in the collimated experiments presented in the publication A.I. The performances at one order of magnitude higher throughput were tested during the uncollimated experiments observing a limited dead time. One further order of magnitude could be gained exploiting the parallelizable architecture of the FlashCam modules, which were here adopted with a solution consisting of one single FADC. The FlashCam has been designed to handle order of thousand channels and demonstrated for data rates above $3 \text{ GByte} \cdot \text{s}^{-1}$. Under such conditions, countermeasures should be taken to avoid limitations in data storage. Possible solutions are the online data reduction and the analogical rejection of the coincidence events in the spectroscopic units and the overflows in the CeBr_3 generated by charged particles. Finally, the development of a full scale prototype made of multiple spectroscopic units operated in parallel should aim to reach the sensitivity required to measure the Bragg peak position with millimetric precision during a single fraction dose delivery.

The measurement of the absolute Bragg peak position during a patient treatment with the method developed in the publication A.I requires the prior knowledge of the tissue composition at the location of the measurement. Such information would be used to generate the patient specific model analogous to the one presented in Figure 4.44 for double distilled water. Several independent approaches could be selected to achieve this. In the first case, one could use the information from the planning CT and combine it with a prior probability distribution to obtain an estimate of the tissue composition at the location of the measurement. Such approach could benefit from the use of dual energy CT data. At the moment of the treatment, the range of the primary particles would be the only free variable. A second option could be the simultaneous estimation of the tissue composition and the Bragg peak position during the delivery of the treatment dose. Such approach could be based on a set of previously calculated range shift scenarios combined with different tissue compositions and the beam particle range would then be estimated by comparing the experimental data to the previously generated data sets. A third and more robust approach would be the direct measurement of the tissue composition with prompt gamma spectroscopy before the treatment. For example, such measurement could be performed in a passive way during a pre-treatment ion-CT or a in-room ion-radiography. This however would rely on the application in the clinical routine of ion-CT and ion-radiography, which are still in the pre-clinical development phase. Finally, one should consider the geometrical constraints in implementing the prompt gamma spectroscopy system inside a treatment room. The ideal solution would allow an implementation also in a gantry room. In such case, the range control system should simultaneously not overlap with the volumes reserved for the movement of the patient table and the gantry itself. Also, it should not cross the volumes used by the in-room position systems such as cone-beam CT, X-ray flat panels and optical tracking devices. The space left to locate the prompt gamma system is therefore limited. The patent application P.II proposed a solution where the detectors are positioned on a frame directly connected the gantry structure, which is retractable during patient positioning and that shares the rotation axis with the beam and the in-room position systems. This would allow to have the prompt gamma spectroscopy system always perpendicular to the beam direction and at a very well defined position with respect to the other components in the room, facilitating also the procedures of quality assurance and long term stability.

Chapter 6

Summary

This thesis presented the development of a pre-clinical prototype capable to measure the absolute Bragg peak position of protons and heavier ions at a synchrotron based facility. The range measurement was based on the prompt gamma spectroscopy technique, which was previously demonstrated for protons accelerated by cyclotrons and it was investigated here for the first time for heavier ions.

The work presented in this thesis could be summarized in three sub-categories with slightly different aims that build up to achieve the final result. In the first part, a novel technique to perform prompt gamma spectroscopy measurement was proposed and investigated at a cyclotron based facility. In the central part, such technique was refined through the optimization and characterization of the detectors. In the final part, the technique was successfully applied at a synchrotron facility.

The publication A.V proposed the use of CeBr_3 scintillating crystals for prompt gamma spectroscopy. Such crystals combine high energy and time resolution while not presenting intrinsic activity. In this first study, it was demonstrated the possibility to detect the prompt gamma energy spectrum induced by ^1p beams accelerated by a cyclotron from the highest energy peaks down to the $E_\gamma = 511$ keV line. These promising results encouraged the adoption of the CeBr_3 scintillating crystals for the development of the synchrotron dedicated prompt gamma spectroscopy system.

The publications A.II – A.IV optimized and characterized the individual detectors to be used in the pre-clinical prototype. The first part of the system to be optimized was the spectroscopic unit. With dedicated Monte Carlo simulations, the size and geometry of the primary CeBr_3 scintillating crystals were tuned to increase the signal to noise ratio in the detection of high energy gamma radiation. A set of secondary scintillating crystals to be operated in anti-coincidence was also optimized. Such optimized spectroscopic unit was then implemented in the experimental setup and tested in presence of ^4He beams. The experimental results confirmed the improvement of the signal to noise ratio predicted by the Monte Carlo simulations and demonstrated the possibility to detect additional prompt gamma lines not observed during the previous experiments with ^1p beams. Moreover, a beam trigger based on scintillating fibers was designed and implemented in the setup. The experimental tests with clinical ion beams demonstrated the requirements for such detector that were set before designing it. Among others, the requirements included the tracking of the arrival time of single particles within the

bunches, a sub-nanosecond time resolution and the capability to cope with clinical intensities.

The manuscript A.I presents the simultaneous implementation of all the techniques developed in the previous publications. This full setup was used to investigate under clinically relevant conditions the features of the prompt gamma radiation generated by proton at heavier ions at a synchrotron based facility. The distribution of the arrival time of the secondary radiation confirmed that the use of a beam trigger capable of single particle measurement is a strict requirement to efficiently apply background rejection techniques based on time of flight models. The spectroscopic unit confirmed its excellent performances both during collimated and uncollimated experiments detecting $N = 20$ independent spectral lines from $E_\gamma = 511$ keV to $E_\gamma = 6.1$ MeV. The evolution of the intensity of such lines was investigated accurately for high energy ^{12}C beams stopped in water. The experimental results demonstrated for the first time the correlation between the Bragg peak position and the intensities of such spectral lines for ions heavier than protons. The ratios between the position-dependent intensities were used to develop a model correlating the absolute Bragg peak position to the spectral information. Such model was used to determine the precision of the range measurement. It was demonstrated that by increasing the sensibility of the system it will be possible to measure the absolute Bragg peak position with a statistical uncertainty of $\sigma(z) = 2$ mm during the delivery of a single fraction having a plateau dose of $D = 2$ Gy for all the ion beams available at the Heidelberg Ion-Beam Therapy Center.

In conclusion, a method to retrieve the absolute Bragg peak position during ion beam treatments at synchrotron based facilities was proposed, optimized and experimentally demonstrated with a pre-clinical prototype. The clinical application remained outside the scope of the current work. To proceed towards such application, the future work will include the direct measurement of the energy dependent cross sections for prompt gamma production, their integration in the treatment planning software and the development and integration in a treatment room of a full-scale prototype.

List of publications

Peer-reviewed journal articles

- A.I **Dal Bello, R.** , Magalhaes Martins, P. , Brons, S. et al. (2019) Prompt Gamma Spectroscopy for absolute range verification at synchrotron based facilities: experimental results from ^1p , ^4He , ^{12}C and ^{16}O beams, under review in the journal *Physics in Medicine and Biology*
- A.II Magalhaes Martins, P., **Dal Bello, R.**, Seimetz, M. et al. (2019) Hadron beam time tracker for time-of-flight measurements of prompt-gamma, under review in the journal *Nuclear Instruments and Methods in Physics Research Section A*
- A.III **Dal Bello, R.** , Magalhaes Martins, P. , Graça, J. et al. (2019) Results from the experimental evaluation of CeBr_3 scintillators for ^4He prompt gamma spectroscopy, *Medical Physics*, 46(8), pp. 3615-3626. doi: 10.1002/mp.13594
- A.IV **Dal Bello, R.**, Magalhaes Martins, P. and Seco, J. (2018), CeBr_3 scintillators for ^4He prompt gamma spectroscopy: Results from a Monte Carlo optimization study, *Medical Physics*, 45(4), pp. 1622-1630. doi: 10.1002/mp.12795
- A.V Magalhaes Martins, P., **Dal Bello, R.** , Rinscheid, A. et al. (2017) Prompt gamma spectroscopy for range control with CeBr_3 , *Current Directions in Biomedical Engineering*, 3(2), pp. 113-117. doi: 10.1515/cdbme-2017-0023

Book chapters

- B.I Magalhaes Martins, P., **Dal Bello, R.** and Seco, J. (2019) Chapter 21: Prompt gamma detection for proton range verification; in Darafsheh, A. (2019) *Radiation Therapy Dosimetry: A Practical Handbook*, CRC Press, ISBN: 9781138543973

Patent applications

- P.I Seco, J., Magalhaes Martins, P., **Dal Bello, R.** and Seimetz, M., (2019) Method and Apparatus for Hadron Beam Time-Tracking for Radiotherapy by means of Synchrotron Accelerated Particles, *U.S. Patent Application*, Nr. 16/375,322
- P.II Seco, J., Magalhaes Martins, P. and **Dal Bello, R.** (2019) A device and a method for monitoring a treatment of a body part of a patient with particles, *European Patent Application*, Nr. 19 186 728.2

Contributions at conferences

- C.I **Dal Bello, R.**, Magalhaes Martins, P., Hermann, G., Kihm, T., Seimetz, M., Brons, S. and Seco, J. **Poster:** Investigation of Prompt Gamma Spectroscopy for range control in synchrotron based facilities: preliminary results from ^1p , ^4He , ^{12}C and ^{16}O beams, *50. Jahrestagung der Deutschen Gesellschaft für Medizinische Physik*, Stuttgart, Germany, September 19th, 2019
- C.II Huang, L., **Dal Bello, R.**, Magalhaes Martins, P. and Seco, J. **Poster:** Monte Carlo characterization of prompt gamma detection with HPGe, *50. Jahrestagung der Deutschen Gesellschaft für Medizinische Physik*, Stuttgart, Germany, September 19th, 2019
- C.III Magalhaes Martins, P., **Dal Bello, R.**, Hermann, G., Kihm, T. and Seco, J. **Talk:** Elemental composition from prompt gamma spectroscopy of irradiated samples with ion beams, *50. Jahrestagung der Deutschen Gesellschaft für Medizinische Physik*, Stuttgart, Germany, September 18th, 2019
- C.IV **Dal Bello, R.**, Magalhaes Martins, P. and Seco, J. **Poster:** Prompt Gamma Spectroscopy for Range Control in Ion Beam Therapy, *Ciência 2019 - Encontro com a Ciência e Tecnologia em Portugal*, Lisbon, Portugal, July 8th, 2019
- C.V **Dal Bello, R.**, Magalhaes Martins, P., Graça, J., Hermann, G., Kihm, T. and Seco, J. **Poster:** Range control through Prompt Gamma Spectroscopy with CeBr₃ scintillators: Experimental evaluation of the spectroscopic unit in presence of ^4He beams, *58th Annual Conference of the Particle Therapy Co-Operative Group*, Manchester, United Kingdom, June 10th, 2019
- C.VI **Dal Bello, R.**, Magalhaes Martins, P., Hermann, G., Kihm, T., Seimetz, M., Brons, S. and Seco, J. **Poster:** Towards a synchrotron dedicated system for range control through Prompt Gamma Spectroscopy: experimental results from ^1p , ^4He , ^{12}C , ^{16}O beams, *58th Annual Conference of the Particle Therapy Co-Operative Group*, Manchester, United Kingdom, June 10th, 2019
- C.VII Magalhaes Martins, P., **Dal Bello, R.**, Hermann, G., Kihm, T. and Seco, J. **Talk:** Prompt gamma spectroscopy for the determination of density and elemental compositions of samples irradiated by ion-beams, *58th Annual Conference of the Particle Therapy Co-Operative Group*, Manchester, United Kingdom, June 10th, 2019
- C.VIII Magalhaes Martins, P., **Dal Bello, R.**, Hermann, G., Kihm, T., Seimetz, M. and Seco, J. **Poster:** Hadron beam time tracker for time-of-flight measurements of prompt-gamma, *58th Annual Conference of the Particle Therapy Co-Operative Group*, Manchester, United Kingdom, June 10th, 2019

- C.IX **Dal Bello, R.**, Magalhaes Martins, P., Brons, S., Hermann, G., Kihm, T., Seimetz, M., and Seco, J. **Talk:** Preliminary results from a synchrotron dedicated Prompt Gamma Spectroscopy system: experiments with ^1p , ^4He , ^{12}C and ^{16}O beams, *1st International Biophysics Collaboration Meeting*, Darmstadt, Germany, May 20th, 2019
- C.X Magalhaes Martins, P., **Dal Bello, R.**, Hermann, G., Kihm, T., Seimetz, M., and Seco, J. **Talk:** Hadron beam time tracker for time-of-flight measurements of prompt gamma, *1st International Biophysics Collaboration Meeting*, Darmstadt, Germany, May 20th, 2019
- C.XI **Dal Bello, R.**, Magalhaes Martins, P., Graça, J., Hermann, G., Kihm, T., Seimetz, M. and Seco, J. **Poster:** Development of Prompt Gamma Spectroscopy for Range Control in Ion Beam Therapy, *3rd Heidelberg Symposium on Novel Techniques in Ion Beam Radiotherapy*, Heidelberg, Germany, October 15th, 2018
- C.XII Zieger, V., **Dal Bello, R.**, Bangert, M. and Seco, J. **Poster:** Auswirkung der Tumorrandgröße auf Risikoorgane für die Ionenstrahltherapie, 49. *Jahrestagung der Deutschen Gesellschaft für Medizinische Physik*, Nürnberg, Germany, September 19th, 2018
- C.XIII **Dal Bello, R.**, Magalhaes Martins, P., Hermann, G., Kihm, T., Seimetz, M. and Seco, J. **Talk:** Prompt Gamma Spectroscopy for range control with CeBr₃: enhanced spectra detection for ^1H and ^{12}C beams, *57th Annual Conference of the Particle Therapy Co-Operative Group*, Cincinnati, United States of America, May 26th, 2018
- C.XIV Magalhaes Martins, P., **Dal Bello, R.**, Hermann, G., Kihm, T., Laorden, M., Seimetz, M. and Seco, J. **Talk:** Towards prompt gamma spectroscopy for ^{12}C range control: development of a synchrotron-dedicated system, *57th Annual Conference of the Particle Therapy Co-Operative Group*, Cincinnati, United States of America, May 26th, 2018
- C.XV **Dal Bello, R.**, Magalhaes Martins, P. and Seco, J. **Poster:** Towards a PGS prototype for ion range verification at synchrotron-based facilities, *4th Scientific Meeting National Center for Radiation Oncology*, Dresden, Germany, March 15th, 2018
- C.XVI **Dal Bello, R.**, Magalhaes Martins, P. and Seco, J. **Talk:** Comparison of prompt gamma emission for ^4He and ^1H beams: a Monte Carlo study, 48. *Jahrestagung der Deutschen Gesellschaft für Medizinische Physik*, Dresden, Germany, September 10th, 2017
- C.XVII Magalhaes Martins, P., **Dal Bello, R.**, Rinscheid, A., Roemer, K., Werner, T., Enghardt, W., Pauch, G. and Seco, J. **Talk:** Prompt gamma spectroscopy for range control with CeBr₃, 48. *Jahrestagung der Deutschen Gesellschaft für Medizinische Physik*, Dresden, Germany, September 10th, 2017

- C.XVIII **Dal Bello, R.** and **Seco, J.** **Poster:** Comparison of Prompt Gamma Emission for Helium and Proton beams: A Monte Carlo study, *3th Scientific Meeting National Center for Radiation Oncology, Heidelberg, Germany, April 6th, 2017*

Acknowledgements

I would like to start with a great thank to Prof. Dr. Joao Seco. From the first moment I discussed with him the idea of extending prompt gamma spectroscopy to ion beams, I got fascinated by this project. I thank him not only for being my direct supervisor, member of the thesis advisory committee and referee of the thesis; but also for the enthusiasm he constantly had in coordinating the project. I think this was one of the key aspects for the successful development and completion of my doctoral studies.

Another key aspect was the excellent team work. For this, I would like to sincerely thank Dr. Paulo Magalhaes Martins. During the last three years we shared many sleepless nights to perform the experiments followed by deep discussions to interpret the data. This is a good example of how a well tuned small team can be successful.

I would also like to thank Prof. Dr. Oliver Jäkel for being the second referee of the thesis and my mentor in the clinical training as a medical physicist, which I pursued as a complementary activity. The latter gained greater importance through my doctoral studies since I consider fundamental to translate to the clinics the basic research in order to eventually improve the patient treatments.

Many thanks also to the collaborators that were involved at different stages in the project: Dr. German Hermann and Dr. Thomas Khim for the excellent support with the data acquisition system, Dr. Michael Seimetz for the development the beam trigger, the HIT staff and in particular Dr. Stephan Brons for the exceptional technical support during the experiments and also Joao Graça, Gernot Echner, Armin Runz, Mechthild Kämmer, Wibke Johnen.

The development of this doctoral project would not have been possible without the founding provided by the International Max Planck Research School for Quantum Dynamics in Physics, Chemistry and Biology. I am grateful to Prof. Dr. Peter Bachert for introducing me to this excellent school and also to the coordinator Prof. Dr. Jörg Evers who has always been keen in being updated on the status of my project.

I had the fortune to perform my doctoral studies in a dynamic, international and full of enthusiasm environment. For this, I have to thank my colleagues in the division Biomedical Physics in Radiation Oncology at the German Cancer Research Center. Many thanks also to the colleagues from the other divisions and also other institutes, who never missed a chance for a scientific discussion and kept high my scientific curiosity.

Finally, a huge thank to my family and my friends. They were always present through the oscillations between positive and negative moments and made sure that the frequency was not too high. Special thanks to my family that is now scattered through Europe and, despite this, it feels like we are always together.

Bibliography

- Actis, M. et al. (2011). "Design concepts for the Cherenkov Telescope Array CTA: an advanced facility for ground-based high-energy gamma-ray astronomy". In: *Experimental Astronomy* 32.3, pp. 193–316. ISSN: 0922-6435. DOI: 10.1007/s10686-011-9247-0. URL: <http://link.springer.com/10.1007/s10686-011-9247-0>.
- Agostinelli, S. et al. (2003). "Geant4—a simulation toolkit". In: *Nuclear Instruments and Methods in Physics Research Section A: Accelerators, Spectrometers, Detectors and Associated Equipment* 506.3, pp. 250–303. ISSN: 0168-9002. DOI: 10.1016/S0168-9002(03)01368-8. URL: <https://www.sciencedirect.com/science/article/pii/S0168900203013688?via%3Dihub>.
- Ajzenberg-Selove, F. (1991). "Energy levels of light nuclei A = 13–15". In: *Nuclear Physics A* 523.1, pp. 1–196. ISSN: 0375-9474. DOI: 10.1016/0375-9474(91)90446-D. URL: <https://www.sciencedirect.com/science/article/pii/037594749190446D?via%3Dihub>.
- Aldawood, S. et al. (2017). "Development of a Compton camera for prompt-gamma medical imaging". In: *Radiation Physics and Chemistry* 140, pp. 190–197. ISSN: 0969-806X. DOI: 10.1016/J.RADPHYSICHEM.2017.01.024. URL: <https://www.sciencedirect.com/science/article/abs/pii/S0969806X17300981>.
- Alexandrov, Andrey et al. (2019). "The FOOT FragmentatiON Of Target Experiment". In: *CERN Proc.* 1, pp. 305–312. URL: <http://inspirehep.net/record/1726663/>.
- Alici, A. (2012). "Status and performance of the ALICE MRPC-based Time-Of-Flight detector". In: *Journal of Instrumentation* 7.10. ISSN: 17480221. DOI: 10.1088/1748-0221/7/10/P10024.
- Allison, J. et al. (2016). "Recent developments in GEANT4". In: *Nuclear Instruments and Methods in Physics Research, Section A: Accelerators, Spectrometers, Detectors and Associated Equipment* 835, pp. 186–225. ISSN: 01689002. DOI: 10.1016/j.nima.2016.06.125.
- Amaldi, Ugo et al. (2005). "Radiotherapy with beams of carbon ions". In: *Reports on Progress in Physics* 68.8, pp. 1861–1882. ISSN: 0034-4885. DOI: 10.1088/0034-4885/68/8/R04. URL: <http://stacks.iop.org/0034-4885/68/i=8/a=R04?key=crossref.9a0f1e1c20da5f308fd7ce9a8adad161>.
- Aricò, G et al. (2019). "Investigation of single carbon ion fragmentation in water and PMMA for hadron therapy". In: *Physics in Medicine & Biology* 64.5, p. 055018. ISSN: 1361-6560. DOI: 10.1088/1361-6560/aafa46. URL: <http://stacks.iop.org/0031-9155/64/i=5/a=055018?key=crossref.3ff6790bd1475297d1a043666ced7ce9>.
- ASTAR. URL: <https://physics.nist.gov/PhysRefData/Star/Text/ASTAR.html>.

- Basunia, M.S. et al. (2016). "Nuclear Data Sheets for $A = 26$ ". In: *Nuclear Data Sheets* 134, pp. 1–148. ISSN: 0090-3752. DOI: 10.1016/J.NDS.2016.04.001. URL: <https://www.sciencedirect.com/science/article/abs/pii/S0090375216300011>.
- Battistoni, Giuseppe et al. (2015). "Overview of the FLUKA code". In: *Annals of Nuclear Energy* 82, pp. 10–18. ISSN: 0306-4549. DOI: 10.1016/J.ANUCENE.2014.11.007. URL: <https://www.sciencedirect.com/science/article/pii/S0306454914005878?via%3Dihub>.
- Beddar, A. S. et al. (1992a). "Water-equivalent plastic scintillation detectors for high-energy beam dosimetry: I. Physical characteristics and theoretical considerations". In: *Physics in Medicine and Biology* 37.10, pp. 1883–1900. ISSN: 00319155. DOI: 10.1088/0031-9155/37/10/006.
- (1992b). "Water-equivalent plastic scintillation detectors for high-energy beam dosimetry: II. Properties and measurements". In: *Physics in Medicine and Biology* 37.10, pp. 1901–1913. ISSN: 00319155. DOI: 10.1088/0031-9155/37/10/007.
- Beddar, Sam et al. (2016). *Scintillation Dosimetry*. Vol. Taylor & Francis Group, p. 43. ISBN: 9781482208993.
- Bethe, H. (1930). "Zur Theorie des Durchgangs schneller Korpuskularstrahlen durch Materie". In: *Annalen der Physik* 397.3, pp. 325–400. ISSN: 00033804. DOI: 10.1002/andp.19303970303. URL: <http://doi.wiley.com/10.1002/andp.19303970303>.
- Biegun, Aleksandra K. et al. (2012). "Time-of-flight neutron rejection to improve prompt gamma imaging for proton range verification: A simulation study". In: *Physics in Medicine and Biology* 57.20, pp. 6429–6444. ISSN: 00319155. DOI: 10.1088/0031-9155/57/20/6429.
- Bisogni, Maria Giuseppina et al. (2017). "INSIDE in-beam positron emission tomography system for particle range monitoring in hadrontherapy." In: *Journal of medical imaging (Bellingham, Wash.)* 4.1, p. 011005. ISSN: 2329-4302. DOI: 10.1117/1.JMI.4.1.011005. URL: <http://www.ncbi.nlm.nih.gov/pubmed/27981069><http://www.pubmedcentral.nih.gov/articlerender.fcgi?artid=PMC5133454>.
- Blanco, A. et al. (2013). "Performance of the HADES-TOF RPC wall in a Au + Au beam at 1.25 AGeV". In: *Journal of Instrumentation* 8.1. ISSN: 17480221. DOI: 10.1088/1748-0221/8/01/P01004.
- Bloch, F. (1933). "Zur Bremsung rasch bewegter Teilchen beim Durchgang durch Materie". In: *Annalen der Physik* 408.3, pp. 285–320. ISSN: 00033804. DOI: 10.1002/andp.19334080303. URL: <http://doi.wiley.com/10.1002/andp.19334080303>.
- Böhlen, T.T. et al. (2014). "The FLUKA Code: Developments and Challenges for High Energy and Medical Applications". In: *Nuclear Data Sheets* 120, pp. 211–214. ISSN: 00903752. DOI: 10.1016/j.nds.2014.07.049. URL: <https://linkinghub.elsevier.com/retrieve/pii/S0090375214005018>.
- Bom, Victor et al. (2012). "Real-time prompt gamma monitoring in spot-scanning proton therapy using imaging through a knife-edge-shaped slit". In: *Physics in Medicine and Biology* 57.2, pp. 297–308. ISSN: 0031-9155. DOI: 10.1088/

- 0031-9155/57/2/297. URL: <http://stacks.iop.org/0031-9155/57/i=2/a=297?key=crossref.2523573b42ccfc95280b551032a2188c>.
- Bortfeld, Thomas (1997). "An analytical approximation of the Bragg curve for therapeutic proton beams". In: *Medical Physics* 24.12, pp. 2024–2033. ISSN: 00942405. DOI: 10.1118/1.598116. URL: <http://doi.wiley.com/10.1118/1.598116>.
- Bragg, W. H. et al. (1905). "On the alpha particles of radium, and their loss of range in passing through various atoms and molecules". In: *The London, Edinburgh, and Dublin Philosophical Magazine and Journal of Science* 10.57, pp. 318–340. DOI: 10.1080/14786440509463378. URL: <https://www.tandfonline.com/doi/full/10.1080/14786440509463378>.
- Brun, Rene et al. (1997). "ROOT — An object oriented data analysis framework". In: *Nuclear Instruments and Methods in Physics Research Section A: Accelerators, Spectrometers, Detectors and Associated Equipment* 389.1-2, pp. 81–86. ISSN: 0168-9002. DOI: 10.1016/S0168-9002(97)00048-X. URL: <https://www.sciencedirect.com/science/article/pii/S016890029700048X?via%3Dihub>.
- Buitenhuis, H J T et al. (2017). "Beam-on imaging of short-lived positron emitters during proton therapy". In: *Physics in Medicine and Biology* 62.12, pp. 4654–4672. ISSN: 0031-9155. DOI: 10.1088/1361-6560/aa6b8c. URL: <http://stacks.iop.org/0031-9155/62/i=12/a=4654?key=crossref.9d1061e240d30bc8fbc2ff2e7d256777>.
- Burrows, T.W. (2006). "Nuclear Data Sheets for A = 48". In: *Nuclear Data Sheets* 107.7, pp. 1747–1922. ISSN: 0090-3752. DOI: 10.1016/J.NDS.2006.05.005. URL: <https://www.sciencedirect.com/science/article/abs/pii/S0090375206000482?via%3Dihub>.
- (2007). "Nuclear Data Sheets for A = 47". In: *Nuclear Data Sheets* 108.5, pp. 923–1056. ISSN: 0090-3752. DOI: 10.1016/J.NDS.2007.04.002. URL: <https://www.sciencedirect.com/science/article/abs/pii/S0090375207000403?via%3Dihub>.
- Cambraia Lopes, Patricia et al. (2015). "Time-resolved imaging of prompt-gamma rays for proton range verification using a knife-edge slit camera based on digital photon counters". In: *Physics in Medicine and Biology* 60.15, pp. 6063–6085. ISSN: 13616560. DOI: 10.1088/0031-9155/60/15/6063.
- Cartiglia, N. et al. (2017). "Beam test results of a 16 ps timing system based on ultra-fast silicon detectors". In: *Nuclear Instruments and Methods in Physics Research, Section A: Accelerators, Spectrometers, Detectors and Associated Equipment* 850, pp. 83–88. ISSN: 01689002. DOI: 10.1016/j.nima.2017.01.021.
- Cheung, Joey et al. (2010). "Dose perturbations and image artifacts caused by carbon-coated ceramic and stainless steel fiducials used in proton therapy for prostate cancer". In: *Physics in Medicine and Biology* 55.23, pp. 7135–7147. ISSN: 0031-9155. DOI: 10.1088/0031-9155/55/23/S13. URL: <http://stacks.iop.org/0031-9155/55/i=23/a=S13?key=crossref.7fb7a371ec8b5cec3c5554e1e60cf8be>.

- Cho, Jongmin et al. (2013). "Feasibility of proton-activated implantable markers for proton range verification using PET." In: *Physics in medicine and biology* 58.21, pp. 7497–512. ISSN: 1361-6560. DOI: 10.1088/0031-9155/58/21/7497. URL: <http://www.ncbi.nlm.nih.gov/pubmed/24099853><http://www.pubmedcentral.nih.gov/articlerender.fcgi?artid=PMC3998106>.
- Crespo, Paulo et al. (2005). "Suppression of random coincidences during in-beam PET measurements at ion beam radiotherapy facilities". In: *IEEE Transactions on Nuclear Science* 52.4, pp. 980–987. ISSN: 00189499. DOI: 10.1109/TNS.2005.852637.
- Dal Bello, R (2016). *Degradation of proton and carbon Bragg peaks due to density inhomogeneities - Master Thesis Heidelberg University*.
- Dal Bello, Riccardo et al. (2018). "CeBr₃ scintillators for 4He prompt gamma spectroscopy: Results from a Monte Carlo optimization study". In: *Medical Physics* 45.4, pp. 1622–1630. ISSN: 00942405. DOI: 10.1002/mp.12795.
- Dal Bello, Riccardo et al. (2019). "Results from the experimental evaluation of CeBr₃ scintillators for 4He prompt gamma spectroscopy". In: *Medical Physics* 46.8, pp. 3615–3626. DOI: 10.1002/mp.13594. URL: <https://onlinelibrary.wiley.com/doi/abs/10.1002/mp.13594>.
- Dedes, G et al. (2014). "Assessment and improvements of Geant4 hadronic models in the context of prompt-gamma hadrontherapy monitoring". In: *Physics in Medicine and Biology* 59.7, pp. 1747–1772. ISSN: 0031-9155. DOI: 10.1088/0031-9155/59/7/1747. URL: <http://stacks.iop.org/0031-9155/59/i=7/a=1747?key=crossref.3f45e687a475152e4b240b70c7507a83>.
- Dietlicher, Isabelle et al. (2014). "The effect of surgical titanium rods on proton therapy delivered for cervical bone tumors: experimental validation using an anthropomorphic phantom". In: *Physics in Medicine & Biology* 59.23, p. 7181. ISSN: 0031-9155. DOI: 10.1088/0031-9155/59/23/7181. URL: <https://iopscience.iop.org/article/10.1088/0031-9155/59/23/7181>.
- Draeger, E. et al. (2018). "3D prompt gamma imaging for proton beam range verification". In: *Physics in Medicine and Biology* 63.3. ISSN: 13616560. DOI: 10.1088/1361-6560/aaa203.
- Ekelhof, Robert Jan (2016). "Studies for the LHCb SciFi Tracker - Development of Modules from Scintillating Fibres and Tests of their Radiation Hardness". In: DOI: 10.17877/DE290R-17235.
- Enghardt, W et al. (2004). "Charged hadron tumour therapy monitoring by means of PET". In: *Nuclear Instruments and Methods in Physics Research Section A: Accelerators, Spectrometers, Detectors and Associated Equipment* 525.1-2, pp. 284–288. ISSN: 0168-9002. DOI: 10.1016/J.NIMA.2004.03.128. URL: <https://www.sciencedirect.com/science/article/pii/S0168900204004218?via%3Dihub>.
- Fano, U (1963). "Penetration of Protons, Alpha Particles, and Mesons". In: *Annual Review of Nuclear Science* 13.1, pp. 1–66. ISSN: 0066-4243. DOI: 10.1146/annurev.ns.13.120163.000245. URL: <http://www.annualreviews.org/doi/10.1146/annurev.ns.13.120163.000245>.

- Félix-Bautista, Renato et al. (2019). "Experimental verification of a non-invasive method to monitor the lateral pencil beam position in an anthropomorphic phantom for carbon-ion radiotherapy". In: *Physics in Medicine and Biology*. ISSN: 0031-9155. DOI: 10.1088/1361-6560/ab2ca3. URL: <http://iopscience.iop.org/article/10.1088/1361-6560/ab2ca3>.
- Ferrari, Alfredo et al. (2005). *FLUKA: A multi-particle transport code (Program version 2005)*. URL: <http://inspirehep.net/record/701721?ln=it>.
- Ferrero, Veronica et al. (2018). "Online proton therapy monitoring: clinical test of a Silicon-photodetector-based in-beam PET". In: *Scientific Reports* 8.1, p. 4100. ISSN: 2045-2322. DOI: 10.1038/s41598-018-22325-6. URL: <http://www.nature.com/articles/s41598-018-22325-6>.
- Fiorina, E et al. (2019). "Preliminary results of the longitudinal clinical trial for in-vivo treatment verification in particle therapy with the INSIDE bi-modal system". In: *PTCOG58*. DOI: <https://doi.org/10.26226/morressier.5cb72191ae0a09001583099b>.
- Foley, K.J. et al. (1962). "Gamma-radiation from the medium energy proton bombardment of sodium, magnesium, aluminium, silicon phosphorus and sulphur". In: *Nuclear Physics* 37, pp. 23–44. ISSN: 0029-5582. DOI: 10.1016/0029-5582(62)90243-2. URL: <https://www.sciencedirect.com/science/article/pii/0029558262902432?via%3Dihub>.
- Gallin-Martel, M. L. et al. (2018). "A large area diamond-based beam tagging hodoscope for ion therapy monitoring". In: *EPJ Web of Conferences*. Vol. 170. EDP Sciences. DOI: 10.1051/epjconf/201817009005.
- Gensheimer, Michael F. et al. (2010). "In vivo proton beam range verification using spine MRI changes". In: *International Journal of Radiation Oncology Biology Physics* 78.1, pp. 268–275. ISSN: 03603016. DOI: 10.1016/j.ijrobp.2009.11.060.
- Gil, E. Cortina et al. (2017). "The beam and Detector of the NA62 experiment at CERN". In: *Journal of Instrumentation* 12.5. ISSN: 17480221. DOI: 10.1088/1748-0221/12/05/P05025.
- Golnik, Christian et al. (2014). "Range assessment in particle therapy based on prompt gamma-ray timing measurements". In: *Physics in Medicine and Biology* 59.18, pp. 5399–5422. DOI: 10.1088/0031-9155/59/18/5399. URL: <http://stacks.iop.org/0031-9155/59/i=18/a=5399?key=crossref.5437fcd3059992135ec2113679c7dad6>.
- Golnik, Christian et al. (2016). "Compton Camera and Prompt Gamma Ray Timing: Two Methods for In Vivo Range Assessment in Proton Therapy". In: *Frontiers in Oncology* 6. DOI: 10.3389/fonc.2016.00080.
- Graeff, Christian et al. (2018). "[OA027] Helium as a range probe in carbon ion therapy". In: *Physica Medica* 52, p. 11. ISSN: 1120-1797. DOI: 10.1016/J.EJMP.2018.06.099. URL: <https://www.sciencedirect.com/science/article/abs/pii/S1120179718305817>.
- Greilich, S. (2017). *Tools to Measure and Improve the Microscopic Energy Deposition in Ion Beam Therapy - Habilitation Thesis Heidelberg University*.
- Guttormsen, M et al. (1996). *The unfolding of continuum γ -ray spectra*. Tech. rep., pp. 371–376.

- Haberer, Th. et al. (2004). "The heidelberg ion therapy center". In: *Radiotherapy and Oncology* 73, S186–S190. ISSN: 0167-8140. DOI: 10.1016/S0167-8140(04)80046-X. URL: <https://www.sciencedirect.com/science/article/pii/S016781400480046X?via%3Dihub>.
- Haettner, E. et al. (2013). "Experimental study of nuclear fragmentation of 200 and 400 MeV/u 12C ions in water for applications in particle therapy". In: *Physics in Medicine and Biology* 58.23, pp. 8265–8279. ISSN: 00319155. DOI: 10.1088/0031-9155/58/23/8265.
- Handrack, Josefine et al. (2017). "Sensitivity of post treatment positron emission tomography/computed tomography to detect inter-fractional range variations in scanned ion beam therapy". In: *Acta Oncologica* 56.11, pp. 1451–1458. ISSN: 0284-186X. DOI: 10.1080/0284186x.2017.1348628.
- Hoesl, M et al. (2016). "Clinical commissioning of an *in vivo* range verification system for prostate cancer treatment with anterior and anterior oblique proton beams". In: *Physics in Medicine and Biology* 61.8, pp. 3049–3062. ISSN: 0031-9155. DOI: 10.1088/0031-9155/61/8/3049. URL: <http://stacks.iop.org/0031-9155/61/i=8/a=3049?key=crossref.a63bb17824ee1c859184315d00734266>.
- Horst, Felix et al. (2019). "Measurement of He 4 charge- and mass-changing cross sections on H, C, O, and Si targets in the energy range 70–220 MeV/u for radiation transport calculations in ion-beam therapy". In: *Physical Review C* 99.1, p. 014603. ISSN: 2469-9985. DOI: 10.1103/PhysRevC.99.014603. URL: <https://link.aps.org/doi/10.1103/PhysRevC.99.014603>.
- Hueso-Gonzalez, F. et al. (2019). "Compact Method for Proton Range Verification Based on Coaxial Prompt Gamma-Ray Monitoring: a Theoretical Study". In: *IEEE Transactions on Radiation and Plasma Medical Sciences*, pp. 1–1. ISSN: 2469-7311. DOI: 10.1109/trpms.2019.2930362.
- Hueso-González, Fernando et al. (2015). "First test of the prompt gamma ray timing method with heterogeneous targets at a clinical proton therapy facility". In: *Physics in Medicine and Biology* 60.16, pp. 6247–6272. DOI: 10.1088/0031-9155/60/16/6247.
- Hueso-González, Fernando et al. (2018). "A full-scale clinical prototype for proton range verification using prompt gamma-ray spectroscopy". In: *Physics in Medicine and Biology* 63.18. ISSN: 13616560. DOI: 10.1088/1361-6560/aad513.
- Janssen, FMFC et al. (2014). "Factors influencing the accuracy of beam range estimation in proton therapy using prompt gamma emission". In: *Physics in Medicine and Biology* 59.15, pp. 4427–4441. ISSN: 0031-9155. DOI: 10.1088/0031-9155/59/15/4427. URL: <http://stacks.iop.org/0031-9155/59/i=15/a=4427?key=crossref.43b84093e36d45a0f60f2e260ad44f8f>.
- Jongen, Y et al. (2003). "Verification of the proton beam position in the patient by the detection of prompt gamma-rays emission". In: *PTCOG* 39.
- Joram, C. et al. (2015). "Scintillating Fibre Tracking at High Luminosity Colliders". In: *Journal of Instrumentation* 10.8. ISSN: 17480221. DOI: 10.1088/1748-0221/10/08/C08005.

- Kelleter, Laurent et al. (2017). "Spectroscopic study of prompt-gamma emission for range verification in proton therapy". In: *Physica Medica* 34, pp. 7–17. ISSN: 1724191X. DOI: 10.1016/j.ejmp.2017.01.003.
- Kelley, J.H. et al. (2012). "Energy levels of light nuclei A=11". In: *Nuclear Physics A* 880, pp. 88–195. ISSN: 0375-9474. DOI: 10.1016/J.NUCLPHYSA.2012.01.010. URL: <https://www.sciencedirect.com/science/article/abs/pii/S0375947412000413>.
- Kelley, J.H. et al. (2017). "Energy levels of light nuclei A = 12". In: *Nuclear Physics A* 968, pp. 71–253. ISSN: 0375-9474. DOI: 10.1016/J.NUCLPHYSA.2017.07.015. URL: <https://www.sciencedirect.com/science/article/abs/pii/S0375947417303330?via%3Dihub>.
- Kellnberger, Stephan et al. (2016). "Ionoacoustic tomography of the proton Bragg peak in combination with ultrasound and optoacoustic imaging". In: *Scientific Reports* 6.1, p. 29305. ISSN: 2045-2322. DOI: 10.1038/srep29305. URL: <http://www.nature.com/articles/srep29305>.
- Kinsey, R R (1998). "The NUDAT/PCNUDAT Program for Nuclear Data". In: *IAEA-NDS-162* 27.1. URL: <http://www-nds.iaea.or.at>.
- Kirn, Thomas (2017). "SciFi – A large scintillating fibre tracker for LHCb". In: *Nuclear Instruments and Methods in Physics Research, Section A: Accelerators, Spectrometers, Detectors and Associated Equipment* 845, pp. 481–485. ISSN: 01689002. DOI: 10.1016/j.nima.2016.06.057.
- Knopf, Antje Christin et al. (2013). *In vivo proton range verification: A review*. DOI: 10.1088/0031-9155/58/15/R131.
- Koehler, A M (1968). "Proton radiography." In: *Science (New York, N.Y.)* 160.3825, pp. 303–4. ISSN: 0036-8075. DOI: 10.1126/science.160.3825.303. URL: <http://www.ncbi.nlm.nih.gov/pubmed/17788234>.
- Kozlovsky, Benzion et al. (2002). "Nuclear Deexcitation Gamma-Ray Lines from Accelerated Particle Interactions". In: *The Astrophysical Journal Supplement Series* 141.2, pp. 523–541. ISSN: 0067-0049. DOI: 10.1086/340545.
- Kraan, Aafke Christine (2015). "Range Verification Methods in Particle Therapy: Underlying Physics and Monte Carlo Modeling". In: *Frontiers in Oncology* 5. ISSN: 2234-943X. DOI: 10.3389/fonc.2015.00150.
- Krimmer, J et al. (2017). "A cost-effective monitoring technique in particle therapy via uncollimated prompt gamma peak integration To cite this version : HAL Id : hal-01508408". In:
- Krimmer, J. et al. (2018). *Prompt-gamma monitoring in hadrontherapy: A review*. DOI: 10.1016/j.nima.2017.07.063.
- Leo, William R. (1994). "Passage of Radiation Through Matter". In: *Techniques for Nuclear and Particle Physics Experiments*. Berlin, Heidelberg: Springer Berlin Heidelberg, pp. 17–68. DOI: 10.1007/978-3-642-57920-2_{_}2. URL: http://link.springer.com/10.1007/978-3-642-57920-2_2.
- Leverington, B.D. et al. (2018). "A prototype scintillating fibre beam profile monitor for Ion Therapy beams". In: *Journal of Instrumentation* 13.05, P05030–P05030. ISSN: 1748-0221. DOI: 10.1088/1748-0221/13/05/P05030. URL: <http://stacks.iop.org/1748-0221/13/i=05/a=P05030?key=crossref.f525aab76f0a1bad8ce7b3b9c7fa997a>.

- Lim, Young Kyung et al. (2009). "Microscopic Gold Particle-Based Fiducial Markers for Proton Therapy of Prostate Cancer". In: *International Journal of Radiation Oncology*Biophysics* 74.5, pp. 1609–1616. ISSN: 0360-3016. DOI: 10.1016/J.IJROBP.2009.02.076. URL: <https://www.sciencedirect.com/science/article/pii/S0360301609005847?via%3Dihub>.
- Lopes, P Cambraia et al. (2012). "Optimization of Collimator Designs for Real-Time Proton Range Verification by Measuring Prompt Gamma Rays Lz". In: pp. 3864–3870.
- Lu, Hsiao-Ming et al. (2010). "Investigation of an implantable dosimeter for single-point water equivalent path length verification in proton therapy." In: *Medical physics* 37.11, pp. 5858–66. ISSN: 0094-2405. DOI: 10.1118/1.3504609. URL: <http://www.ncbi.nlm.nih.gov/pubmed/21158298><http://www.pubmedcentral.nih.gov/articlerender.fcgi?artid=PMC2980544>.
- Magalhaes Martins, P et al. (2019a). "Prompt gamma detection for proton range verification". In: *Radiation Therapy Dosimetry: A Practical Handbook*. Ed. by A Darafsheh. 1st ed. CRC Press. Chap. 21. ISBN: 9781138543973.
- Magalhaes Martins, Paulo et al. (2017). "Prompt gamma spectroscopy for range control with CeBr3". In: *Current Directions in Biomedical Engineering* 3.2, pp. 113–117. DOI: 10.1515/cdbme-2017-0023. URL: <http://www.degruyter.com/view/j/cdbme.2017.3.issue-2/cdbme-2017-0023/cdbme-2017-0023.xml>.
- Magalhaes Martins, Paulo et al. (2019b). *Hadron beam time tracker for time-of-flight measurements of prompt-gamma*. Tech. rep. GSI-2019-00596. DOI: 10.15120/GSI-2019-00596. URL: https://www.gsi.de/fileadmin/Biophysik/Bilder/Bilder_Gallery/Biophysics_Collaboration/Final_Version_web_version.pdf.
- Marafini, M. et al. (2015). "The INSIDE project: Innovative solutions for in-beam dosimetry in hadrontherapy". In: *Acta Physica Polonica A*. Vol. 127. 5. Polish Academy of Sciences, pp. 1465–1467. DOI: 10.12693/APhysPolA.127.1465.
- Martišiková, M et al. (2018). "Helium ion beam imaging for image guided ion radiotherapy." In: *Radiation oncology (London, England)* 13.1, p. 109. ISSN: 1748-717X. DOI: 10.1186/s13014-018-1046-6. URL: <http://www.ncbi.nlm.nih.gov/pubmed/29898746><http://www.pubmedcentral.nih.gov/articlerender.fcgi?artid=PMC6000951>.
- Mattei, I et al. (2017). "Secondary radiation measurements for particle therapy applications: prompt photons produced by He-4, C-12 and O-16 ion beams in a PMMA target". In: *Physics in Medicine and Biology* 62.4, pp. 1438–1455. DOI: 10.1088/1361-6560/62/4/1438. URL: <http://stacks.iop.org/0031-9155/62/i=4/a=1438?key=crossref.00d5a6c5030dd8128b1df21977daef60>.
- Mazzucconi, Davide et al. (2018). "Mixed particle beam for simultaneous treatment and online range verification in carbon ion therapy: Proof-of-concept study". In: *Medical Physics* 45.11, pp. 5234–5243. ISSN: 00942405. DOI: 10.1002/mp.13219.

- Mein, Stewart et al. (2018). "Fast robust dose calculation on GPU O ion therapy : the FROG platform". In: pp. 1–12. DOI: 10.1038/s41598-018-33194-4.
- Mein, Stewart et al. (2019). "Biophysical modeling and experimental validation of relative biological effectiveness (RBE) for 4He ion beam therapy". In: *Radiation Oncology* 14.1, p. 123. ISSN: 1748-717X. DOI: 10.1186/s13014-019-1295-z. URL: <https://ro-journal.biomedcentral.com/articles/10.1186/s13014-019-1295-z>.
- Min, C.H. et al. (2007). "Determination of distal dose edge location by measuring right-angled prompt-gamma rays from a 38 MeV proton beam". In: *Nuclear Instruments and Methods in Physics Research Section A: Accelerators, Spectrometers, Detectors and Associated Equipment* 580.1, pp. 562–565. ISSN: 0168-9002. DOI: 10.1016/J.NIMA.2007.05.235. URL: <https://www.sciencedirect.com/science/article/pii/S0168900207011230?via%3Dihub>.
- Min, Chul Hee et al. (2006). "Prompt gamma measurements for locating the dose falloff region in the proton therapy". In: *Applied Physics Letters* 89.18. ISSN: 00036951. DOI: 10.1063/1.2378561.
- Min, Chul Hee et al. (2012). "Development of array-type prompt gamma measurement system for in vivo range verification in proton therapy". In: *Medical Physics* 39.4, pp. 2100–2107. ISSN: 00942405. DOI: 10.1118/1.3694098.
- Morháč, Miroslav et al. (1997). "Background elimination methods for multidimensional coincidence gamma-ray spectra". In: *Nuclear Instruments and Methods in Physics Research Section A: Accelerators, Spectrometers, Detectors and Associated Equipment* 401.1, pp. 113–132. DOI: 10.1016/S0168-9002(97)01023-1. URL: <https://www.sciencedirect.com/science/article/pii/S0168900297010231>.
- (2000). "Identification of peaks in multidimensional coincidence gamma-ray spectra". In: *Nuclear Instruments and Methods in Physics Research Section A: Accelerators, Spectrometers, Detectors and Associated Equipment* 443.1, pp. 108–125. DOI: 10.1016/S0168-9002(99)01005-0. URL: <https://www.sciencedirect.com/science/article/pii/S0168900299010050?via%3Dihub>.
- Moteabbed, M. et al. (2011). "Monte Carlo patient study on the comparison of prompt gamma and PET imaging for range verification in proton therapy". In: *Physics in Medicine and Biology* 56.4, pp. 1063–1082. ISSN: 00319155. DOI: 10.1088/0031-9155/56/4/012.
- Owen, Hywel et al. (2016). "Current and future accelerator technologies for charged particle therapy". In: *Nuclear Instruments and Methods in Physics Research Section A: Accelerators, Spectrometers, Detectors and Associated Equipment* 809, pp. 96–104. ISSN: 0168-9002. DOI: 10.1016/J.NIMA.2015.08.038. URL: <https://www.sciencedirect.com/science/article/pii/S0168900215009729?via%3Dihub>.
- Paganetti, Harald (2012). *Range uncertainties in proton therapy and the role of Monte Carlo simulations*. DOI: 10.1088/0031-9155/57/11/R99.

- Panaino, C. et al. (2018). "Abstract ID: 171 A Monte Carlo study to reduce range uncertainty in proton beam therapy via prompt gamma-ray detection". In: *Physica Medica* 45, S2. ISSN: 1120-1797. DOI: 10.1016/J.EJMP.2017.11.027. URL: <https://www.sciencedirect.com/science/article/abs/pii/S1120179717306221?via%3Dihub>.
- Parodi, K. et al. (2005). "Random coincidences during in-beam PET measurements at microbunched therapeutic ion beams". In: *Nuclear Instruments and Methods in Physics Research, Section A: Accelerators, Spectrometers, Detectors and Associated Equipment* 545.1-2, pp. 446–458. ISSN: 01689002. DOI: 10.1016/j.nima.2005.02.002.
- Parodi, K et al. (2008). *Measurement of the carbon ion microstructure after KO extraction*. Tech. rep. EXTERNAL-HIT-08, p. 381.
- Pausch, G. et al. (2016). "Scintillator-Based High-Throughput Fast Timing Spectroscopy for Real-Time Range Verification in Particle Therapy". In: *IEEE Transactions on Nuclear Science* 63.2, pp. 664–672. ISSN: 0018-9499. DOI: 10.1109/TNS.2016.2527822. URL: <http://ieeexplore.ieee.org/document/7454861/>.
- Pausch, Guntram et al. (2018a). *Detection systems for range monitoring in proton therapy: Needs and challenges*. DOI: 10.1016/j.nima.2018.09.062.
- Pausch, Guntram et al. (2018b). "Nuclear Inst. and Methods in Physics Research, A Detection systems for range monitoring in proton therapy: Needs and challenges". In: *Nuclear Inst. and Methods in Physics Research, A* July. ISSN: 0168-9002. DOI: 10.1016/j.nima.2018.09.062. URL: <https://doi.org/10.1016/j.nima.2018.09.062>.
- Pemler, P. et al. (1999). "A detector system for proton radiography on the gantry of the Paul-Scherrer-Institute". In: *Nuclear Instruments and Methods in Physics Research Section A: Accelerators, Spectrometers, Detectors and Associated Equipment* 432.2-3, pp. 483–495. ISSN: 0168-9002. DOI: 10.1016/S0168-9002(99)00284-3. URL: <https://www.sciencedirect.com/science/article/pii/S0168900299002843?via%3Dihub>.
- Petzoldt, J. et al. (2016). "Characterization of the microbunch time structure of proton pencil beams at a clinical treatment facility". In: *Physics in Medicine and Biology* 61.6, pp. 2432–2456. ISSN: 13616560. DOI: 10.1088/0031-9155/61/6/2432.
- Piersimoni, Pierluigi et al. (2018). "Helium CT : Monte Carlo simulation results for an ideal source and detector with comparison to proton CT". In: *Medical Physics* 45.7, pp. 3264–3274. ISSN: 0094-2405. DOI: 10.1002/mp.12942. URL: <https://onlinelibrary.wiley.com/doi/abs/10.1002/mp.12942>.
- Pinto, M et al. (2014). "Design optimisation of a TOF-based collimated camera prototype for online hadrontherapy monitoring". In: *Physics in Medicine and Biology* 59.24, pp. 7653–7674. ISSN: 0031-9155. DOI: 10.1088/0031-9155/59/24/7653. URL: <http://stacks.iop.org/0031-9155/59/i=24/a=7653?key=crossref.6459a07fee7232565c291a3caffa90ff>.
- Pinto, M et al. (2015). "Absolute prompt-gamma yield measurements for ion beam therapy monitoring". In: *Physics in Medicine and Biology* 60.2, pp. 565–594. ISSN: 0031-9155. DOI: 10.1088/0031-9155/60/2/565. URL:

- <http://stacks.iop.org/0031-9155/60/i=2/a=565?key=crossref.c4760640602341dfb0ce09b91884d4e4>.
- Pinto, Marco et al. (2016). "Assessment of Geant4 Prompt-Gamma Emission Yields in the Context of Proton Therapy Monitoring." In: *Frontiers in oncology* 6, p. 10. ISSN: 2234-943X. DOI: 10.3389/fonc.2016.00010. URL: <http://www.ncbi.nlm.nih.gov/pubmed/26858937><http://www.pubmedcentral.nih.gov/articlerender.fcgi?artid=PMC4729887>.
- Polf, J. C. et al. (2009). "Measurement and calculation of characteristic prompt gamma ray spectra emitted during proton irradiation". In: *Physics in Medicine and Biology* 54.22. ISSN: 00319155. DOI: 10.1088/0031-9155/54/22/N02.
- Povh, B et al. (2008). *Particles and Nuclei*. Ed. by B Povh. 6th ed. Heidelberg: Springer-Verlag Berlin Heidelberg, p. 246. ISBN: 978-3-540-79368-7. DOI: 10.1007/978-3-540-79368-7.
- PTCOG. URL: <https://www.ptcog.ch/>.
- PTCOG (2018). *Particle Therapy Patient Statistics (per end of 2018)*. URL: <https://www.ptcog.ch/images/patientstatistics/Patientstatistics-updateDec2018.pdf>.
- Quarati, F G A et al. (2013). "Scintillation and detection characteristics of high-sensitivity CeBr3 gamma-ray spectrometers". In: *Nuclear Instruments and Methods in Physics Research Section A: Accelerators, Spectrometers, Detectors and Associated Equipment* 729, pp. 596–604. DOI: 10.1016/J.NIMA.2013.08.005. URL: <https://www.sciencedirect.com/science/article/pii/S0168900213011297?via%3Dihub>.
- Richter, Christian et al. (2016). "First clinical application of a prompt gamma based in vivo proton range verification system." In: *Radiotherapy and oncology : journal of the European Society for Therapeutic Radiology and Oncology* 118.2, pp. 232–7. ISSN: 1879-0887. DOI: 10.1016/j.radonc.2016.01.004. URL: <http://www.ncbi.nlm.nih.gov/pubmed/26774764>.
- Roemer, K. et al. (2015). "Characterization of scintillator crystals for usage as prompt gamma monitors in particle therapy". In: *Journal of Instrumentation* 10.10, P10033–P10033. ISSN: 1748-0221. DOI: 10.1088/1748-0221/10/10/P10033. URL: <http://stacks.iop.org/1748-0221/10/i=10/a=P10033?key=crossref.97faf45643409837756a2a2493868c0e>.
- Ryan, C.G. et al. (1988). "SNIP, a statistics-sensitive background treatment for the quantitative analysis of PIXE spectra in geoscience applications". In: *Nuclear Instruments and Methods in Physics Research Section B: Beam Interactions with Materials and Atoms* 34.3, pp. 396–402. ISSN: 0168-583X. DOI: 10.1016/0168-583X(88)90063-8. URL: <https://www.sciencedirect.com/science/article/pii/0168583X88900638>.
- Sadrozinski, H. F.W. et al. (2016). "Ultra-fast silicon detectors (UFSD)". In: *Nuclear Instruments and Methods in Physics Research, Section A: Accelerators, Spectrometers, Detectors and Associated Equipment* 831, pp. 18–23. ISSN: 01689002. DOI: 10.1016/j.nima.2016.03.093.
- Sadrozinski, Hartmut F.W. et al. (2018). *4D tracking with ultra-fast silicon detectors*. DOI: 10.1088/1361-6633/aa94d3.
- Schoemers, Christian et al. (2015). "The intensity feedback system at Heidelberg Ion-Beam Therapy Centre". In: *Nuclear Instruments and Methods in*

- Physics Research, Section A: Accelerators, Spectrometers, Detectors and Associated Equipment* 795, pp. 92–99. ISSN: 01689002. DOI: 10.1016/j.nima.2015.05.054.
- Schuemann, J et al. (2014). “Site-specific range uncertainties caused by dose calculation algorithms for proton therapy.” In: *Physics in medicine and biology* 59.15, pp. 4007–31. ISSN: 1361-6560. DOI: 10.1088/0031-9155/59/15/4007. URL: <http://www.ncbi.nlm.nih.gov/pubmed/24990623><http://www.pubmedcentral.nih.gov/articlerender.fcgi?artid=PMC4136435>.
- Schulte, R. et al. (2004). “Conceptual design of a proton computed tomography system for applications in proton radiation therapy”. In: *IEEE Transactions on Nuclear Science* 51.3, pp. 866–872. ISSN: 0018-9499. DOI: 10.1109/TNS.2004.829392. URL: <http://ieeexplore.ieee.org/document/1311983/>.
- Schüttauf, A. (2004). “Timing RPCs in FOPI”. In: *Nuclear Instruments and Methods in Physics Research, Section A: Accelerators, Spectrometers, Detectors and Associated Equipment*. Vol. 533. 1-2, pp. 65–68. DOI: 10.1016/j.nima.2004.07.002.
- Sihver, Lembit et al. (1998). “Depth-Dose Distributions of High-Energy Carbon, Oxygen and Neon Beams in Water”. In: *Japanese Journal of Medical Physics* 18.1, pp. 1–21. ISSN: 0918-8010. DOI: 10.11323/jjmp1992.18.1{_}1. URL: https://www.jstage.jst.go.jp/article/jjmp1992/18/1/18_1/_article/-char/ja.
- Smeets, J et al. (2012). “Prompt gamma imaging with a slit camera for real-time range control in proton therapy”. In: *Physics in Medicine and Biology* 57.11, pp. 3371–3405. ISSN: 0031-9155. DOI: 10.1088/0031-9155/57/11/3371. URL: <http://stacks.iop.org/0031-9155/57/i=11/a=3371?key=crossref.cbb392ae153f40350872c31cf8c5ed3f>.
- Target Systemelektronik*. URL: <http://target-sg.com/>.
- Tessonier, Thomas et al. (2018). “Proton and Helium Ion Radiotherapy for Meningioma Tumors: A Monte Carlo-based Treatment Planning Comparison”. In: *Radiation Oncology* 13.1. ISSN: 1748717X. DOI: 10.1186/s13014-017-0944-3.
- Testa, E. et al. (2008). “Monitoring the Bragg peak location of 73MeVu carbon ions by means of prompt γ -ray measurements”. In: *Applied Physics Letters* 93.9, p. 093506. ISSN: 0003-6951. DOI: 10.1063/1.2975841. URL: <http://aip.scitation.org/doi/10.1063/1.2975841>.
- Testa, E. et al. (2009). “Dose profile monitoring with carbon ions by means of prompt-gamma measurements”. In: *Nuclear Instruments and Methods in Physics Research Section B: Beam Interactions with Materials and Atoms* 267.6, pp. 993–996. ISSN: 0168-583X. DOI: 10.1016/J.NIMB.2009.02.031. URL: <https://www.sciencedirect.com/science/article/pii/S0168583X09002468>.
- Testa, M. et al. (2010). “Real-time monitoring of the Bragg-peak position in ion therapy by means of single photon detection”. In: *Radiation and Environmental Biophysics* 49.3, pp. 337–343. ISSN: 0301634X. DOI: 10.1007/s00411-010-0276-2.

- Thompson, Ian J. et al. (2009). *Nuclear Reactions for Astrophysics*. Cambridge: Cambridge University Press. ISBN: 9781139152150. DOI: 10.1017/CB09781139152150. URL: <http://ebooks.cambridge.org/ref/id/CB09781139152150>.
- Tilley, D.R. et al. (1992). "Energy levels of light nuclei $A = 4$ ". In: *Nuclear Physics A* 541.1, pp. 1–104. ISSN: 0375-9474. DOI: 10.1016/0375-9474(92)90635-W. URL: <https://www.sciencedirect.com/science/article/pii/037594749290635W?via%3Dihub>.
- Tilley, D.R. et al. (1993). "Energy levels of light nuclei $A = 16-17$ ". In: *Nuclear Physics A* 564.1, pp. 1–183. ISSN: 0375-9474. DOI: 10.1016/0375-9474(93)90073-7. URL: <https://www.sciencedirect.com/science/article/pii/0375947493900737?via%3Dihub>.
- Tilley, D.R. et al. (2004). "Energy levels of light nuclei $A=8,9,10$ ". In: *Nuclear Physics A* 745.3-4, pp. 155–362. ISSN: 0375-9474. DOI: 10.1016/J.NUCLPHYSA.2004.09.059. URL: <https://www.sciencedirect.com/science/article/abs/pii/S0375947404010267?via%3Dihub>.
- Tommasino, Francesco et al. (2015). "New Ions for Therapy". In: *International Journal of Particle Therapy* 2.3, pp. 428–438. ISSN: 2331-5180. DOI: 10.14338/ijpt-15-00027.1.
- Townsend, L. W. et al. (1986). "Energy-Dependent Parameterization of Heavy-Ion Absorption Cross Sections". In: *Radiation Research* 106.3, p. 283. ISSN: 00337587. DOI: 10.2307/3576735. URL: <https://www.jstor.org/stable/3576735?origin=crossref>.
- Vanstalle, Marie et al. (2017). "Benchmarking Geant4 hadronic models for prompt γ monitoring in carbon ion therapy". In: *Medical Physics* 44.8, pp. 4276–4286. DOI: 10.1002/mp.12348. URL: <https://onlinelibrary.wiley.com/doi/abs/10.1002/mp.12348>.
- Verburg, Joost M. et al. (2012). "Simulation of prompt gamma-ray emission during proton radiotherapy". In: *Physics in Medicine and Biology* 57.17, pp. 5459–5472. ISSN: 00319155. DOI: 10.1088/0031-9155/57/17/5459.
- Verburg, Joost M. et al. (2013a). "Dosimetric accuracy of proton therapy for chordoma patients with titanium implants". In: *Medical Physics* 40.7, p. 071727. ISSN: 00942405. DOI: 10.1118/1.4810942. URL: <http://doi.wiley.com/10.1118/1.4810942>.
- Verburg, Joost M. et al. (2013b). "Energy- and time-resolved detection of prompt gamma-rays for proton range verification". In: *Physics in Medicine and Biology* 58.20. ISSN: 00319155. DOI: 10.1088/0031-9155/58/20/L37.
- Verburg, Joost M. et al. (2014). "Proton range verification through prompt gamma-ray spectroscopy". In: *Physics in Medicine and Biology* 59.23, pp. 7089–7106. ISSN: 13616560. DOI: 10.1088/0031-9155/59/23/7089.
- Vidal-Quadras, A. et al. (1979). "Production of fragments of mass number 6A11 in 12C, 14N and 16O spallation by alpha-particles at energies near threshold". In: *Il Nuovo Cimento A* 49.2, pp. 235–246. ISSN: 0369-3546. DOI: 10.1007/BF02896725. URL: <http://link.springer.com/10.1007/BF02896725>.
- Vignati, A. et al. (2017). "Innovative thin silicon detectors for monitoring of therapeutic proton beams: preliminary beam tests". In: *Journal of Instrumentation* 12.12, pp. C12056–C12056. ISSN: 1748-0221. DOI: 10.1088/1748-

- 0221/12/12/C12056. URL: <http://stacks.iop.org/1748-0221/12/i=12/a=C12056?key=crossref.ee7eeb02680f19ce03500a8b575e3fa0>.
- Wambersie, A. et al. (2004). "Light" or Heavy" ions : a debate of terminology?" In: *Radiotherapy and Oncology* 73, p. iii. ISSN: 0167-8140. DOI: 10.1016/S0167-8140(04)80003-3. URL: <https://www.sciencedirect.com/science/article/pii/S0167814004800033>.
- Werner, F. et al. (2017). "Performance verification of the FlashCam prototype camera for the Cherenkov Telescope Array". In: *Nuclear Instruments and Methods in Physics Research Section A: Accelerators, Spectrometers, Detectors and Associated Equipment* 876, pp. 31–34. ISSN: 0168-9002. DOI: 10.1016/J.NIMA.2016.12.056. URL: <https://www.sciencedirect.com/science/article/pii/S0168900216313225?via%3Dihub>.
- Wohlfahrt, Patrick et al. (2017). "Clinical Implementation of Dual-energy CT for Proton Treatment Planning on Pseudo-monoenergetic CT scans". In: *International Journal of Radiation Oncology*Biophysics* 97.2, pp. 427–434. ISSN: 0360-3016. DOI: 10.1016/J.IJROBP.2016.10.022. URL: <https://www.sciencedirect.com/science/article/pii/S0360301616333429>.
- Wu, S.-C. (2000). "Nuclear Data Sheets for A = 46". In: *Nuclear Data Sheets* 91.1, pp. 1–116. ISSN: 0090-3752. DOI: 10.1006/NDSH.2000.0014. URL: <https://www.sciencedirect.com/science/article/pii/S0090375200900140>.
- Xie, Yunhe et al. (2017). "Prompt Gamma Imaging for In Vivo Range Verification of Pencil Beam Scanning Proton Therapy". In: 99.1, pp. 210–218. DOI: 10.1016/j.ijrobp.2017.04.027.
- Ytre-Hauge, Kristian Smeland et al. (2019). "A Monte Carlo feasibility study for neutron based real-time range verification in proton therapy". In: *Scientific Reports* 9.1, p. 2011. ISSN: 2045-2322. DOI: 10.1038/s41598-019-38611-w. URL: <http://www.nature.com/articles/s41598-019-38611-w>.
- Yuan, Yading et al. (2013). "Feasibility study of in vivo MRI based dosimetric verification of proton end-of-range for liver cancer patients". In: *Radiotherapy and Oncology* 106.3, pp. 378–382. ISSN: 0167-8140. DOI: 10.1016/J.RADONC.2013.01.016. URL: <https://www.sciencedirect.com/science/article/pii/S0167814013000455?via%3Dihub>.